Study of the decay $\tau \to 3\pi(n\gamma)\nu_\tau$
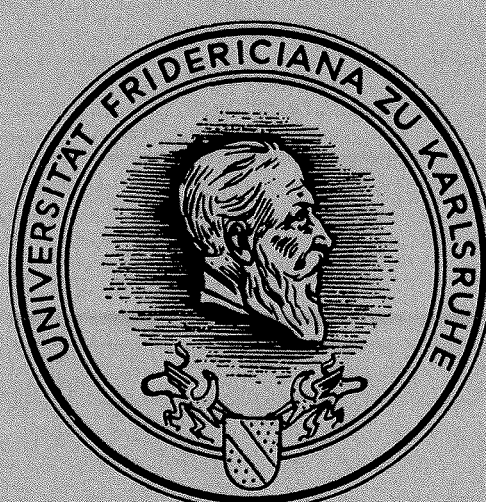
with the DELPHI Detector at LEP

Paolo Privitera

INSTITUT FÜR EXPERIMENTELLE KERNPHYSIK

UNIVERSITÄT KARLSRUHE

Study of the decay $\tau \to 3\pi(n\gamma)\nu_\tau$

with the DELPHI Detector at LEP

Paolo Privitera

Zur Erlangung des akademischen Grades eines

DOKTORS DER NATURWISSENSCHAFTEN

von der Fakultät für Physik der Universität (TH)

genehmigte

DISSERTATION

von

Paolo Privitera
aus Catania

Zusammenfassung

In dieser Arbeit werden experimentelle Studien zum Zerfall des τ –Leptons vorgestellt. Die Daten, die bei dieser Analyse benutzt wurden, stammen vom DELPHI-Detektor, einer der vier großen ($\approx 10 \times 10 \times 10$ m^3) Detektoren, der sich an einem der 8 Wechselwirkungspunkte des LEP[1]-Ringes am CERN befindet. Die Planung und der Betrieb dieses Experiments ist das Ergebnis einer gemeinsamen Anstrengung von vielen Hunderten von Physikern, Ingenieuren und Technikern. Elektronen und Positronen werden im LEP–Ring beschleunigt und bei einer Schwerpunktsenergie von ca. 91 GeV zur Kollision gebracht. Bislang wurden bei diesen Zusammenstössen mehrere Millionen Z^0–Teilchen produziert.

Die Z^0– und $W^\pm$–Bosonen wurden 1984 am CERN in Proton–Antiproton–Kollisionen entdeckt. Ihre Masse liegt genau in dem Bereich, der durch die Theorie der Vereinheitlichung der elektromagnetischen mit der schwachen Wechselwirkung vorhergesagt wird.

Die hohe Statistik der LEP–Daten erlaubt eine präzise Bestimmung der physikalischen Eigenschaften des Z^0–Bosons. Seine Masse konnte bei LEP sehr genau bestimmt werden, wobei der relative Fehler bei 10^{-4} liegt. Alle Messungen, die am LEP durchgeführt wurden, bestätigen das sogenannte Standardmodell der elektroschwachen Wechselwirkung mit einer hohen Genauigkeit. Bislang gibt es keinen Hinweis auf neue Physik außerhalb des Standardmodells. Wird das Standardmodell die neue „Weltanschauung" in der Elementarteilchenphysik?

Ungefähr 3.3 % der Z^0–Bosonen zerfallen in $\tau^+\tau^-$–Paare. Das τ –Lepton ist das schwerste der bekannten Leptonen. Seit seiner Entdeckung 1975 mißt man seine fundamentallen Grössen wie Masse, Spin, Punkförmigkeit, Zerfallskanäle und deren zugehörige Verzweigungsverhältnisse.

Das τ zerfällt über die schwache Wechselwirkung in die leichteren Leptonen (Elektronen und Myonen). Aufgrund seiner hohen Masse ($m_\tau \approx 1.78$ GeV) können aber auch Hadronen beim Zerfall entstehen. Somit ist die Anzahl der möglichen Zerfallskanäle sehr groß. Genaues Ausmessen des Verzweigungsverhältnisses in Leptonen liefert wichtige Informationen über die Lepton–Universalität. Die Theorie der schwachen Wechselwirkung liefert Vorhersagen über die leptonischen Zerfallskanäle. Bei Zerfällen des τ 's in Hadronen ist die Situation anders. Um hier genaue Vorhersagen machen zu können, müssen spezielle Modelle für den hadronischen Endzuständen benutzt werden. Eine weitere Schwierigkeit ist das Auftreten von Resonanzen in den hadronischen Endzuständen.

Das Thema dieser Arbeit war die Bestimmung der Polarisation des τ Leptons im Zerfall des Z^0 Bosons. Die Kopplung des Z^0 an Fermionen hängt von der Helizität ab, wodurch die τ's mit einer Polarisation ungleich null produziert werden. Dies ist ein Beispiel für die

---

[1] LEP ist die Abkürzung für Large Electron Positron Ring

Paritätsverletzung. Dies gilt auch für andere Z^0-Zerfälle. Jedoch läßt sich die Polarisation nur beim τ messen, da das τ über den paritätsverletzenden Prozeß der schwachen Wechselwirkung zerfällt. Die Zerfallsprodukte des τ's hängen dadurch vom Helizitätszustand des ursprünglichen Teilchens ab.

Zur Messung der τ-Polarisation wurde eine neue Methode entwickelt. Diese Methode nutzt die kinematischen Größen des Zerfalls in 3 Pionen aus, wobei theoretische Berechnungen von Kühn und Mirkes benutzt wurden. Die stark von der τ-Polarisation abhängigen Verteilungen wurden hergeleitet und es stellte sich heraus, daß die Sensitivität um ungefähr einen Faktor 2 höher war als bei den herkömmlichen Methoden, d. h. der statistische Fehler ist bei dieser neuen Methode nur halb so groß. Diese Verbesserung ist möglich durch Ausnutzung aller Winkelabhängigkeiten im Zerfall.

Mit Hilfe eines Datensamples von 1328 $\tau \rightarrow 3\pi\nu_\tau$ Kandidaten erhält man für die τ-Polarisation einen Wert von:

$$\boxed{P_\tau = -0.265 \pm 0.070_{stat} \pm 0.070_{syst} \pm 0.015_{theor}}$$

Hierbei ist der erste Fehler der statistische und der zweite der systematische. Der dritte Fehler beinhaltet die theoretischen Unsicherheiten, die durch die Modellabhängigkeit des hadronischen Formfaktors hervorgerufen werden. Dieser Fehler ist klein. Somit wird die neue Methode zur Messung der τ-Polarisation beim $\tau \rightarrow 3\pi\nu_\tau$ Zerfall selbst bei einer hohen Statistik nicht durch theoretische Unsicherheiten begrenzt.

Zusätzlich wurde im Rahmen dieser Arbeit das Verzweigungsverhältnis für den exklusiven Zerfall $\tau \rightarrow 3\pi(n\gamma)\nu_\tau$ ermittelt, da die Weltmittel der Verzweigungsverhältnisse einen Diskrepanz zwischen dem exklusiven und dem sogenannten topologischen Verzweigungsverhältnis aufzeigen. Bei der hier durchgeführten Analyse läßt sich ein Teil des Problems durch ein höheres gemessenes Verzweigungsverhältnis in drei geladene Teilchen beheben.
Aus einem Datensample von 1169 $\tau \rightarrow 3\pi n\gamma\nu_\tau$ ($n \geq 0$) Kandidaten wurde das Verzweigungsverhältnis für diesen Kanal bestimmt zu:

$$\boxed{Br(\tau \rightarrow 3\pi n\gamma\nu_\tau) = (13.28 \pm 0.39_{stat} \pm 0.17_{syst})\ \%}$$

Fordert man, daß beim Zerfall keine Photonen erzeugt werden, bleiben 570 $\tau \rightarrow 3\pi\nu_\tau$ Kandidaten übrig. Hierfür findet man ein Verzweigungsverhältnis von:

$$\boxed{Br(\tau \rightarrow 3\pi\nu_\tau) = (8.35 \pm 0.35_{stat} \pm 0.24_{syst})\ \%}$$

Bei beiden Messungen dominieren die statistischen Fehler. Bei der Analyse wurden die Zerfälle $\tau \rightarrow K^*\nu_\tau \rightarrow K_S\pi\nu_\tau \rightarrow \pi\pi\pi\nu_\tau$ als Untergrundereignisse angesehen. Von den oben angegebenen Verzweigungsverhältnissen wurden die Kaon-Zerfälle in drei geladene Teilchen ($\tau \rightarrow K\pi\pi\nu_\tau$, $\tau \rightarrow KK\pi\nu_\tau$) nicht subtrahiert. Insgesamt kann dieser Effekt die Verzweigungsverhältnisse um ca. 1% ändern.

Contents

List of Tables

List of Figures

Introduction

A quotation common to many Introductions to theses in Particle Physics is Democritus' atomism. However, the author must confess to some difficulty in understanding the connection between Particle Physics and Greek Philosophy, even if he did Classical Studies (or probably because of that). Ancient (as well as modern) philosophers are looking at the world as privileged observers, each of them with his own *Weltanschauung*. An experimental physicist would call this attitude systematic bias.

This thesis contains an experimental study of the properties of a specific decay mode of the τ lepton. The data used for the measurement have been collected by the DELPHI experiment. DELPHI is one of the four large-scale detectors ($\simeq 10 \times 10 \times 10$ m^3) installed around one of the interaction point of the Large Electron Positron (LEP) collider ring at CERN. The commissioning and operation of the experiment is the result of a common effort of many hundred of physicists, engineers and technicians. Electron and positron beams are accelerated in the LEP ring and collided at an energy of $\simeq 91$ GeV in the centre of mass. Several million of Z^0 particles have been produced thus far by these collisions.

The Z^0 and $W^\pm$ bosons were discovered with proton-antiproton collisions at CERN in 1984, exactly in the mass range predicted by the theory which unifies electromagnetic and weak force.

The large statistics collected at LEP allows an accurate determination of the Z^0 properties. Its mass has been measured very precisely at LEP, with a relative error of 10^{-4}. All the measurements performed at LEP confirm the so-called Standard Model of the electroweak interaction to a high degree of accuracy. No evidence for new physics beyond the Standard Model has been found. Is the Standard Model becoming the new *Weltanschauung* in Particle Physics?

Approximately 3.3% of the Z^0 bosons decay into $\tau^+\tau^-$ pairs, *i.e.* $Z^0 \to \tau^+\tau^-$. The τ lepton is the heaviest of the known leptons. Since its discovery in 1975, the fundamental properties of the τ lepton have been measured, including the mass, the spin, the pointlike structure, the many decay modes and the corresponding branching ratios.

The τ decays via the weak interaction into the lighter leptons, electron and muon. Also, hadronic states become possible products of the τ decay because of its heavy mass ($m_\tau \simeq 1.78$ GeV). Thus, the pattern of possible τ decay modes is very rich. Precise measurements of τ leptonic branching ratios provide important information on lepton universality. The theory

of weak interaction makes definite predictions of the leptonic decay modes properties. For the hadronic decay modes of the τ, the situation is different. To make definite predictions, specific models for the hadronic current must be used. A further complication is the presence of resonances in the hadronic final states.

One interesting aspect of τ decay physics is a 'might be' inconsistency which has been observed between the so-called τ topological branching ratios and the τ exclusive branching ratios. In the measurement of the topological branching ratios, τ decays are classified according to their charged track topology (one, three, or five tracks) and the relative branching fractions are determined. In the exclusive measurements, the final decay product is identified explicitly, and the branching fractions of $\tau \to e\nu\bar{\nu}$, $\tau \to \mu\nu\bar{\nu}$, $\tau \to \pi\nu$, $\tau \to 3\pi\nu_\tau$, $\tau \to 3\pi\pi^0\nu$, etc. are determined. The sum of the exclusive branching ratios which have a topology of one charged track (like $\tau \to e\nu\bar{\nu}$, $\tau \to \mu\nu\bar{\nu}$, $\tau \to \pi\nu$, etc.) should be equal to the topological determination of τ decay into one charged track. The sum of the exclusive branching ratios which have a topology of three tracks (like $\tau \to 3\pi\nu_\tau$, $\tau \to 3\pi\pi^0\nu$, etc.) should be equal to the topological determination of τ decay into three charged tracks. For a long time the experimental data were not compatible with these simple considerations. In particular, the sum of all the measured exclusive decay modes did not add up to 100%. Recent measurements have found no evidence for such a discrepancy. In particular, part of the problem seems to be solved by a higher branching ratio into three charged tracks.

In this thesis, the branching ratio for the exclusive decay $\tau \to 3\pi(n\gamma)\nu_\tau$ is measured with the DELPHI data. Both the τ decay into three charged particles with the possible presence of photons ($\tau \to 3\pi n\gamma\nu_\tau$ $(n \geq 0)$) and the decay without photons ($\tau \to 3\pi\nu_\tau$) are studied.

The Z^0 couples differently to fermions of opposite helicity. Thus, a τ^- (τ^+) lepton produced by a Z^0 decay will be found with different probabilities in a negative or in a positive helicity state, *i.e.* it will be partially polarized. This is an example of a parity violating process: under the parity operator, which inverts the sign of the helicity, the τ will behave differently. The couplings of the Z^0 to fermions, and thus the fermion polarization, are related to the fundamental parameter of the electroweak theory, $\sin^2\theta_W$. The argument outlined above is valid also for the other Z^0 decays. However, only the τ offers the experimental possibility of measuring such polarization, since the τ decay, through the weak interaction, is also parity violating. The τ decay product characteristics will depend on the helicity state of the parent τ. Measurements of the τ polarization, P_τ, have been performed successfully by the LEP experiments, using the different τ decay modes.

Up to now, the contribution of the $\tau \to 3\pi\nu_\tau$ decay mode to the P_τ measurement has been marginal with respect to the other decay channels. In this thesis, a new method, which improves significantly the sensitivity to P_τ in the $\tau \to 3\pi\nu_\tau$ decay, is used to perform the measurement.

The outline of the thesis is as follows. The general aspects of τ lepton physics are presented in Chapter 1. Particular attention is paid to introducing the concept of τ polarization observables.

A brief description of the experimental apparatus is given in Chapter 2, including the LEP accelerating system and the DELPHI detector.

Chapter 3 is devoted to the measurement of the $\tau \rightarrow 3\pi(n\gamma)\nu_\tau$ exclusive branching ratio from a sample of $\tau^+\tau^-$ events collected in the 1991 LEP run. A detailed discussion of the systematic error estimation is included.

The theoretical aspects the $\tau \rightarrow 3\pi\nu_\tau$ decay are reviewed in Chapter 4. In particular, the most general decay $\tau \rightarrow 3\pi\nu_\tau$ distribution derived by Kühn and Mirkes [1] is discussed. The comparison of different model predictions for the hadronic form factors is an original contribution.

The measurement of the τ polarization using the $\tau \rightarrow 3\pi\nu_\tau$ decay observables is described in Chapter 5. The data sample used for this measurement also includes the part of 1992 data reprocessed with correct detector calibrations which was available at the time the thesis was being written. The P_τ measurement is performed with a new method which takes advantage of the most complete decay distribution discussed in Chapter 4. The sensitivity of the method is determined, and a significant improvement with respect to previous methods is found. Given the novelty of the method, which makes use explicitly of the hadronic form factors, a detailed analysis of the theoretical model dependence is included.

Last is a statement of the main conclusions of this work.

Chapter 1

Physics of the τ lepton

The fundamental properties of the τ lepton are presented in this chapter. The observables in $e^+e^- \to Z^0 \to \tau^+\tau^-$ are introduced with a simple approach. The features of τ polarization measurement are presented.

1.1 Properties of the τ lepton

'Since muons exist in nature for no apparent reason, it is possible that other heavy leptons may also exist in nature. If one discovers heavy leptons, one may be able to understand why muons exist...'. These two speculations open the classical paper of Y. S. Tsai [2], *Decay Correlations of Heavy Leptons in $e^+ + e^- \to l^+ + l^-$* [2], written in 1971. The first evidence for a new heavy lepton was found in 1975 by M. Perl [4], from the observation in e^+e^- annihilation of events with a muon and an electron in the final state. These events were interpreted as being due to the production of a pair of new heavy leptons, which subsequently decay into electron and muon and the accompanying neutrinos. Thus, the first of Tsai speculations happened to be right. On the other hand, the reasons for the existence of the muon and the τ are still unknown.

After the discovery of the τ, the main question centered about its classification in the scheme of quarks and leptons. At that time all the known fundamental fermions could be classified into two generations: one containing the up and down quarks, electron and electron neutrino, and the second containing the strange and charm quark, muon and muon neutrino. The τ represented a puzzle, which was eventually resolved by postulating the existence of a third generation containing the τ and the τ neutrino, and the undiscovered bottom and top quarks. The bottom quark was discovered soon after the τ, and the top quark is the only remaining unobserved fundamental particle.

Comprehensive reviews of the physics of the τ lepton can be found in the literature [3]. Here, only the main properties of the τ lepton are given. The τ is a pointlike spin 1/2 particle. A new very precise measurement of the τ mass $m_\tau = 1776.9 \pm 0.4$ MeV [5] has been recently

performed. The τ lifetime is $\tau_\tau = 305 \pm 6\ fs$ [6]. A rich variety of decay modes has been observed. In fact, because of its large mass, the τ can decay not only into the lighter leptons (e and μ) but also into hadrons. In Table 1.1 the world average branching ratios for the observed τ decay modes are reported [7]. Also the measured values of the topological branching ratios

Exclusive decay mode	Branching ratio (%)
$e^- \bar{\nu}_e \nu_\tau$	17.85 ± 0.29
$\mu^- \bar{\nu}_\mu \nu_\tau$	17.45 ± 0.27
hadron$^- \nu_\tau$	12.47 ± 0.35
hadron$^- \pi^0 \nu_\tau$	23.4 ± 0.6
hadron$^- 2\pi^0 \nu_\tau$	9.0 ± 0.6
hadron$^- \geq 3\pi^0 \nu_\tau$	1.8 ± 0.6
2 hadron$^-$ hadron$^+ \nu_\tau$	8.0 ± 0.3
2 hadron$^-$ hadron$^+ \geq 1$ neutral ν_τ	5.2 ± 0.4
$B_5 = 3$ hadron$^-$ 2 hadron$^+ \nu_\tau$	0.11 ± 0.03
$\sum$ all	95.3 ± 1.3
$\sum$ 1-prong	82.0 ± 1.2
$\sum$ 3-prong	13.2 ± 0.5
Topological decay mode	Branching ratio (%)
B_1	85.94 ± 0.23
B_3	14.06 ± 0.20
Difference topological-exclusive	(%)
100-$\sum$ all	4.7 ± 1.3
B_1 - $\sum$ 1-prong	3.9 ± 1.2
B_3 - $\sum$ 3-prong	0.9 ± 0.5

Table 1.1: *The observed exclusive τ decay modes and the world average for their branching ratios. The sums ($\sum$) are performed over all the exclusive decay modes. Also the topological branching ratios are reported, and the difference with the corresponding sum of exclusive branching ratios is calculated.*

are reported in Table 1.1. Notice that the sum of all the measured exclusive branching ratios do not add up to 100%. This is the so-called 'τ decay problem'. The comparison with the measured topological branching ratios gives additional information. The difference is found essentially in the τ decays into one charged track (1-prong). The inconsistency is even larger ($100 - \sum$ all$=9.4\pm1.6\%$) if the recent measurements of ALEPH [8] and CELLO [9] are excluded from the world averages. These two experiments have measured all the exclusive decay modes listed in Table 1.1, and found no evidence for inconsistency (*i.e.* $\sum$ all $\simeq$ 100%). The main differences between the measurements of ALEPH and CELLO and the measurements performed previously can be found in the decay channels $\tau \to 3\pi\nu_\tau$ and $\tau \to \pi\pi^0\pi^0\nu$. In Table 1.2 the branching ratios for these decay modes as measured by ALEPH and CELLO (average) are compared with the world average values (ALEPH and CELLO excluded) [7].

However, ARGUS [10] has performed recently a measurement of exclusive one-prong and inclusive three-prong branching ratios which confirms the discrepancy.

Thus, the 'τ decay problem' is not solved yet, and new measurements with improved precision

Exclusive decay mode	ALEPH+CELLO (%)	World average
$\pi^- 2\pi^0 \nu_\tau$	10.4 ± 0.9	7.6 ± 0.9
$2\pi^- \pi^+ \nu_\tau$	9.4 ± 0.5	7.2 ± 0.4

Table 1.2: *The branching ratios for $\tau \to 3\pi\nu_\tau$ and $\tau \to \pi\pi^0\pi^0\nu$ as measured by ALEPH and CELLO (average) are compared with the world average values (ALEPH and CELLO excluded).*

are needed to clarify this interesting puzzle.

1.2 Observables in $e^+e^- \to Z^0 \to \tau^+\tau^-$

In this Section, the basic observables in the production of $\tau^+\tau^-$ pairs in electron-positron collisions by Z^0 exchange are derived. The results obtained are valid also for the other possible fermion-antifermion final states, but for the sake of simplicity the τ will be always referred.

Only basic concepts of relativistic quantum mechanics [11] are needed to obtain the phenomenological properties of the $\tau^+\tau^-$ production. The helicity conservation at high energy is one of these concepts. Note that for a fermion with a large energy compared to its mass the following relations are valid:

$$\frac{(1-\gamma^5)}{2}u = u_L, \qquad \frac{(1+\gamma^5)}{2}u = u_R, \tag{1.1}$$

where u is the fermion spinor, γ^5 is the Dirac chirality operator, and the subscript $L(R)$ stands for left(right)-handed. Therefore, at high energy $(1 \pm \gamma^5)/2$ project out the helicity $\lambda = \pm 1$ components of a spinor, respectively. In quantum electrodynamics (QED), processes like the electromagnetic scattering of a fermion are described by the electromagnetic current $\bar{u}\gamma^\mu u$, where γ^μ are the Dirac matrices. Using expressions (1.1), *i.e.* at high energy, the following result can be derived:

$$\bar{u}\gamma^\mu u \equiv (\bar{u}_L + \bar{u}_R)\gamma^\mu(u_L + u_R) = \bar{u}_L\gamma^\mu u_L + \bar{u}_R\gamma^\mu u_R. \tag{1.2}$$

The right hand part of the expression (1.2) implies that at high energies the electromagnetic interaction conserves the helicity of the scattered fermion. Using a similar argument, it can be shown that in the annihilation of a fermion-antifermion pair, for example e^+e^-, the electron and the positron will always be found in states of opposite helicity, *i.e.* only $e_R^+ e_L^-$ and $e_L^+ e_R^-$ are allowed.

Consider now the process $e^+e^- \to \gamma \to \tau^+\tau^-$. Helicity conservation requires that the incoming e^+ and e^- have opposite helicities. The same is true also for the τ^+ and τ^- in the final state. Therefore, in the centre of mass frame, scattering proceeds from an initial state with $J_z = +1$ or -1 to a final state of with $J_{z'} = +1$ or -1, where J is the angular momentum and the z and z' axes are along the ingoing e^- and outgoing τ^- direction, respectively. One of the four possible helicity configurations is represented in Fig. 1.1. The process proceeds via an intermediate photon of spin $j = 1$, and, from the quantum mechanical theory of angular momentum, the amplitude is proportional to the rotation matrix $d^j_{J_{z'}, J_z}(\theta)$.
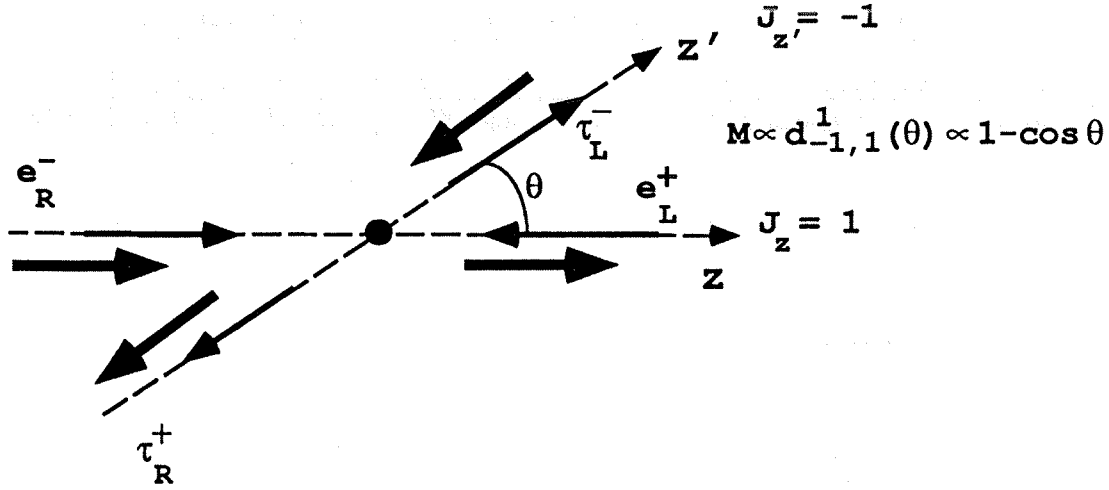
Figure 1.1: *One possible helicity configuration for the process $e^+e^- \to \tau^+\tau^-$. Thin arrows are used for particle momenta, thick arrows for particle spins.*

The four allowed helicity configurations and their corresponding amplitudes are:

$$e_L^+ e_R^- \to \tau_R^+ \tau_L^- \implies M_1 \propto d^1_{-1,+1}(\theta) \propto 1 - \cos\theta \tag{1.3}$$

$$e_R^+ e_L^- \to \tau_L^+ \tau_R^- \implies M_2 \propto d^1_{+1,-1}(\theta) \propto 1 - \cos\theta \tag{1.4}$$

$$e_L^+ e_R^- \to \tau_L^+ \tau_R^- \implies M_3 \propto d^1_{+1,+1}(\theta) \propto 1 + \cos\theta \tag{1.5}$$

$$e_R^+ e_L^- \to \tau_R^+ \tau_L^- \implies M_4 \propto d^1_{-1,-1}(\theta) \propto 1 + \cos\theta. \tag{1.6}$$

The differential cross section is obtained by spin averaging the helicity amplitudes:

$$\frac{d\sigma}{d\cos\theta} \propto \sum_{i=1}^{4} |M_i|^2 \propto (1 - \cos\theta)^2 + (1 + \cos\theta)^2 \propto 1 + \cos^2\theta. \tag{1.7}$$

This is a well known QED result.

Consider now the process $e^+e^- \to Z^0 \to \tau^+\tau^-$, and assume that it is parity violating. In the QED formalism, parity violation is readily obtained by multiplying the Dirac matrices with a term $(g_V - g_A\gamma^5)$. The reason can be better understood by writing the parity violation operator as:

$$g_V - g_A\gamma^5 = (g_V - g_A)\frac{1+\gamma^5}{2} + (g_V + g_A)\frac{1-\gamma^5}{2} = g_R\frac{1+\gamma^5}{2} + g_L\frac{1-\gamma^5}{2}, \tag{1.8}$$

where $g_R = (g_V - g_A)$ and $g_L = (g_V + g_A)$. The operator (1.8) extracts the right-handed component of a fermion spinor with the coupling constant g_R and the left-handed component with the coupling constant g_L (*cf.* expressions (1.1)). If $g_R \neq g_L$ the process will be parity violating, since a parity transformation $(x, y, z) \to (-x, -y, -z)$ inverts the sign of the helicities

and a process which is described by a probability $|g_R|^2$ in the (x, y, z) world would appear with a different probability $|g_L|^2$ in the $(-x, -y, -z)$ world. Notice that $g_R = g_L$ implies $g_A = 0$, and g_A is different from zero by construction.

To calculate the angular dependence expressions (1.3)-(1.6) can be used, but they must be multiplied by the coupling constants appropriate to the specific helicity configuration. For example, expression (1.3) becomes:

$$e_L^+ e_R^- \to Z^0 \to \tau_R^+ \tau_L^- \implies N_1 \propto [d_{-1,+1}^1(\theta)] g_R^e g_L^\tau \propto (1 - \cos\theta) g_R^e g_L^\tau, \tag{1.9}$$

where the g_R^e factor is produced by applying the parity violation operator (1.8) to the right-handed electron (or the left-handed positron) in the initial state current, and the g_L^τ factor is produced by applying the parity violation operator to the left-handed τ^- (or the right-handed τ^+) in the final state current. Notice that the coupling of the Z^0 to electrons could be different from its coupling to τ's, and a superscript has been used to keep the full generality. Analogous amplitudes can be derived for the three other possible helicity configurations:

$$e_R^+ e_L^- \to Z^0 \to \tau_L^+ \tau_R^- \implies N_2 \propto [d_{+1,-1}^1(\theta)] g_L^e g_R^\tau \propto (1 - \cos\theta) g_L^e g_R^\tau, \tag{1.10}$$

$$e_L^+ e_R^- \to Z^0 \to \tau_L^+ \tau_R^- \implies N_3 \propto [d_{+1,+1}^1(\theta)] g_R^e g_R^\tau \propto (1 + \cos\theta) g_R^e g_R^\tau, \tag{1.11}$$

$$e_R^+ e_L^- \to Z^0 \to \tau_R^+ \tau_L^- \implies N_4 \propto [d_{-1,-1}^1(\theta)] g_L^e g_L^\tau \propto (1 + \cos\theta) g_L^e g_L^\tau, \tag{1.12}$$

The differential cross section is obtained by spin averaging the helicity amplitudes:

$$\begin{aligned}
\frac{d\sigma}{d\cos\theta} &\propto \sum_{i=1}^4 |N_i|^2 \propto [(g_R^e g_L^\tau)^2 + (g_L^e g_R^\tau)^2](1 - \cos\theta)^2 + [(g_R^e g_R^\tau)^2 + (g_L^e g_L^\tau)^2](1 + \cos\theta)^2 \\
&\propto 1 + \cos^2\theta + 2 \frac{2g_V^e g_A^e}{(g_V^e)^2 + (g_A^e)^2} \frac{2g_V^\tau g_A^\tau}{(g_V^\tau)^2 + (g_A^\tau)^2} \cos\theta.
\end{aligned} \tag{1.13}$$

The last expression in (1.13) has been obtained by substituting the g_R and g_L couplings with the corresponding combinations of g_V and g_A.

Notice that a term proportional to $\cos\theta$ is present in the angular distribution (1.13). Experimentally, an angular asymmetry will be observed by studying the cross section for $e^+e^- \to \tau^+\tau^-$ as a function of $\cos\theta$. Thus, a new observable, commonly called forward-backward asymmetry (A_{FB}), can be introduced, rewriting the differential cross section as:

$$\frac{d\sigma}{d\cos\theta} \propto 1 + \cos^2\theta + \frac{8}{3} A_{FB} \cos\theta, \tag{1.14}$$

with

$$A_{FB} = \frac{3}{4} \frac{2g_V^e g_A^e}{(g_V^e)^2 + (g_A^e)^2} \frac{2g_V^\tau g_A^\tau}{(g_V^\tau)^2 + (g_A^\tau)^2}. \tag{1.15}$$

Another observable can be defined:

$$P_{\tau^-} = \frac{N_{\tau^-}(\lambda' = +1) - N_{\tau^-}(\lambda' = -1)}{N_{\tau^-}(\lambda' = +1) + N_{\tau^-}(\lambda' = -1)}, \tag{1.16}$$

where $N_{\tau^-}(\lambda' = \pm 1)$ is the number of τ^- with helicity $\lambda' = \pm 1$ defined with respect to the z' axis (see Fig. 1.1). Thus, P_{τ^-} is defined as the τ^- polarization. The probability of producing a positive and a negative helicity τ^- in the process $e^+e^- \to Z^0 \to \tau^+\tau^-$ is proportional to $(g_R^\tau)^2$ and $(g_L^\tau)^2$, respectively. Thus, the τ polarization defined in expression (1.16) is given by:

$$P_{\tau^-} = \frac{(g_R^\tau)^2 - (g_L^\tau)^2}{(g_R^\tau)^2 + (g_L^\tau)^2} = -\frac{2g_V^\tau g_A^\tau}{(g_V^\tau)^2 + (g_A^\tau)^2}, \tag{1.17}$$

where the last expression has been obtained by substituting the g_R and g_L couplings with the corresponding combinations of g_V and g_A.

The τ polarization defined in (1.16) is an average polarization, *i.e.* is obtained by averaging over $\cos\theta$. Also the angular dependence of P_τ can be derived:

$$P_{\tau^-}(\cos\theta) = \frac{N_{\tau^-}^+(\cos\theta) - N_{\tau^-}^-(\cos\theta)}{N_{\tau^-}^+(\cos\theta) + N_{\tau^-}^-(\cos\theta)} \tag{1.18}$$

where $N_{\tau^-}^\pm(\cos\theta)$ is the number of τ^- produced at a given $\cos\theta$ with helicity ± 1. The number of positive(negative) helicity τ^-'s at a given $\cos\theta$ is proportional to $|N_2|^2 + |N_3|^2 (|N_1|^2 + |N_4|^2)$. Introducing in (1.18) the expressions (1.9)-(1.12), and writing the couplings in terms of g_V and g_A, the angular dependence of P_{τ^-} becomes:

$$P_{\tau^-}(\cos\theta) = \frac{(1 + \cos^2\theta)P_{\tau^-} + 2\cos\theta P_{e^-}}{(1 + \cos^2\theta) + 2\cos\theta P_{\tau^-} P_{e^-}}, \tag{1.19}$$

where P_{e^-} is obtained by substituting in expression (1.17) all the τ^- coupling constants with the e^- coupling constants.

Notice that $P_{\tau^+} = -P_{\tau^-}$. Throughout the thesis, the convention $P_\tau \equiv P_{\tau^-}$ will be used.

Notice that the exchange of a Z^0 boson is not essential in the derivation of the observables discussed above. In fact, only the Z^0 parity violation property has been used.

For an appropriate treatment of the Z^0, one should include in the observables:

- the dependence on the Z^0 resonance properties, and

- the effect of radiative corrections.

However, for $\tau^+\tau^-$ produced at a centre of mass energy equal to the Z^0 mass, expressions (1.15), (1.17) and (1.19) are exact. Both the effect of $\tau^+\tau^-$ production at centre of mass energies within a few GeV from the Z^0 mass and the effect of radiative corrections are small. A complete treatment of these effects can be found in the literature [12].

In the Standard Model of electroweak interactions [13] the coupling constants g_V and g_A for leptons are related to the mixing angle $\sin^2\theta_W$, one of the fundamental parameters of the electroweak theory, through:

$$g_V = -\frac{1}{2} + 2\sin^2\theta_W, \tag{1.20}$$

$$g_A = -\frac{1}{2}. \tag{1.21}$$

Inserting (1.20)-(1.21) into expression (1.17), one obtains:

$$P_\tau = -\frac{2(1 - 4\sin^2\theta_W)}{1 + (1 - 4\sin^2\theta_W)^2} \simeq -2(1 - 4\sin^2\theta_W). \qquad (1.22)$$

Inserting (1.20)-(1.21) into expression (1.15) and assuming lepton universality in the electroweak interactions (i.e. $P_e = P_\tau$), one obtains:

$$A_{FB} = \frac{3}{4}P_e P_\tau \simeq 3(1 - 8\sin^2\theta_W + 16(\sin^2\theta_W)^2), \qquad (1.23)$$

where (1.22) has been used to obtain the last expression. Thus, the measurement of P_τ and A_{FB} can provide important information on the electroweak parameter $\sin^2\theta_W$. An interesting point is the sensitivity of these observables to $\sin^2\theta_W$. From (1.22) and (1.23), one can calculate the error on $\sin^2\theta_W$:

$$\Delta\sin^2\theta_{W\,A_{FB}} \simeq \frac{\Delta A_{FB}}{24(1 - 4\sin^2\theta_W)} = \frac{\Delta A_{FB}}{1.6}, \qquad (1.24)$$

$$\Delta\sin^2\theta_{W\,P_\tau} \simeq \frac{\Delta P_\tau}{8}, \qquad (1.25)$$

where $\sin^2\theta_W = 0.233$ has been used in (1.24). The error on $\sin^2\theta_w$ obtained from the measurement of the τ polarization is smaller by more than a factor 4 with respect to that obtained from the measurement of A_{FB}, for $\Delta P_\tau = \Delta A_{FB}$. Thus, even with limited statistics, the measurement of P_τ provides a competitive determination of the electroweak mixing parameter.

1.3 Decays of the τ as polarization analyzers

The decay characteristics of the τ lepton were already established in 1971 by Tsai [2]. In particular, it was clear that since τ^+ and τ^- decay via weak interactions where parity is maximally violated, the angular distribution of decay products depends strongly on the spin orientation of the τ. Thus, the τ decay works as a spin analyzer and gives the unique possibility of determining the τ polarization through the study of the decay products [14].

To clarify the ideas, it is worthwhile to present in some details the simplest case of $\tau^- \to \pi^- \nu_\tau$. Since this is a two body decay, ν_τ and π^- come out back to back in the τ rest frame, and the component of the orbital angular momentum along the direction of ν_τ is thus zero. Now, ν_τ has a negative helicity, and hence prefers to be emitted opposite to the direction of the spin of τ^- in order to conserve angular momentum (see Fig. 1.2). Therefore, π^- prefers to be emitted in the direction of the spin of the τ^-. A quantitative prediction for the pion angular distribution can be simply derived using quantum mechanics (see Fig. 1.2), and turns out to be $W_\pm \propto 1 \pm \cos\bar\theta$ (for τ helicity ± 1), where $\bar\theta$ is the angle between the pion direction and the τ spin quantization axis calculated in the τ rest frame.

Summing over the helicity states, the expected pion angular distribution is:

$$\frac{1}{N}\frac{dN}{d\cos\bar\theta} = \frac{1}{2}\left(1 + P_\tau \cos\bar\theta\right). \qquad (1.26)$$
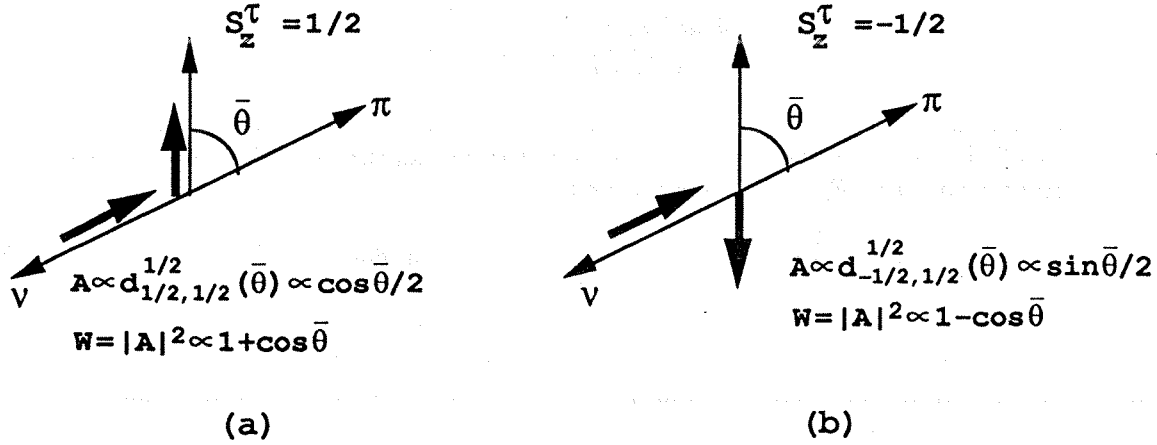
Figure 1.2: *The decay $\tau \to \pi\nu_\tau$ in the τ rest frame. The thin arrows represent particle momenta, the thick ones particle spins. Figures (a) and (b) correspond to the cases for positive and negative τ helicity, respectively.*

The Lorentz boost from the τ rest frame to the Laboratory determines a simple relation between the angle $\bar{\theta}$ and the energy of the pion measured in the Laboratory:

$$\cos\bar{\theta} = \frac{4E_\pi m_\tau^2 - 2E_{beam}(m_\tau^2 + m_\pi^2)}{(m_\tau^2 - m_\pi^2)\sqrt{4E_{beam}^2 - 4m_\tau^2}} \simeq 2x_\pi - 1, \qquad x_\pi = \frac{E_\pi}{E_{beam}}, \qquad (1.27)$$

where the approximation is valid when terms of the order $(m_\pi/m_\tau)^2$ and $(m_\tau/E_{beam})^2$ are neglected. The sensitivity to P_τ given by the pion angular distribution in the τ rest frame is thus recovered in the Laboratory by taking the pion energy distribution:

$$\frac{1}{N}\frac{dN}{dx_\pi} = 1 + P_\tau(2x_\pi - 1). \qquad (1.28)$$

The lepton energy distribution for the leptonic decays $\tau \to \mu\nu\bar{\nu}, e\nu\bar{\nu}$ is also sensitive to P_τ, but since these are not two body decays, the x_{lept} dependence is more complicated (a third order polynomial) resulting in a lower sensitivity to P_τ.

The hadronic decays $\tau \to \rho\nu, a_1\nu$ are similar to the decay into $\pi\nu$, but now the spin 1 hadron presents both longitudinal and transverse spin states, which give an additional factor α multiplying the $\cos\bar{\theta}$ term of Eq. (6), with $\alpha_\rho \simeq 0.46$ and $\alpha_{a_1} \simeq 0.12$. The corresponding reduced sensitivity to P_τ can be recuperated by measuring the helicity of the spin 1 hadron through the decay distribution of the hadronic system [15] [16] [17]. A second angle β, which characterizes the decay distribution of the hadron into final state pions and is expressed in terms of Laboratory observables, is introduced. For the ρ, this is the decay angle of the 2π system with respect to the ρ line of flight, and is given in terms of the energies of the two pions:

$$\cos\beta = \frac{m_\rho}{\sqrt{m_\rho^2 - 4m_\tau^2}} \frac{E_\pi - E_{\pi^0}}{|\vec{p}_\pi + \vec{p}_{\pi^0}|}, \qquad (1.29)$$

while for the a_1, β is the angle between the normal to the decay plane of the 3π system in the a_1 rest frame and the a_1 line of flight. A detailed description of the kinematical variables in the a_1 decay will be given in Section 4.4. A two-dimensional fit to $\cos\bar{\theta}$ and $\cos\beta$ is then performed.

It is interesting to compare the sensitivity of the different decay channels to P_τ. For all the

Decay mode	$S_X = (\Delta P_\tau \sqrt{N})^{-1}$	B_X	Relative weight $S_X^2 B_X$
$\tau \to \pi\nu$	0.6	0.11	1
$\tau \to \rho\nu$	0.52(0.28)	0.23	1.6
$\tau \to a_1\nu$	0.24(0.07)	0.08	0.1
$\tau \to e\nu\bar{\nu}$	0.22	0.18	0.2
$\tau \to \mu\nu\bar{\nu}$	0.22	0.18	0.2

Table 1.3: *Sensitivity, branching ratio and relative weight for the different τ decay modes. For $\tau \to \rho\nu$ and $\tau \to a_1\nu$ the sensitivity for the two-dimensional fit and, in parenthesis, for the one-dimensional fit are quoted. The relative weights are normalized with respect to the $\tau \to \pi\nu$ channel.*

decay modes the P_τ dependence can be expressed in a general way as $W(x) = f(x) + P_\tau g(x)$ with $\int f dx = 1$ and $\int g dx = 0$, where f and g are function of a certain variable x (for example a normalized energy). The error on P_τ obtained from a fit to the distribution $W(x)$ is asymptotically given by:

$$\Delta P_\tau = \frac{1}{\sqrt{N}} \left[\int \frac{g^2}{f + P_\tau g} dx \right]^{-\frac{1}{2}} = \frac{1}{S\sqrt{N}}, \tag{1.30}$$

where N is the number of events contained in the distribution and S represents an ideal sensitivity, *i.e.* in the limit of infinite statistics.

With a given channel X, the error on P_τ is:

$$(\Delta P_\tau)_X = \frac{1}{S_X \sqrt{B_X N_\tau}}, \tag{1.31}$$

where B_X is the branching ratio of $\tau \to X$. The error obtained combining all the decay modes will thus be:

$$\Delta P_\tau = \frac{1}{\sqrt{\sum_X \frac{1}{\Delta P_X^2}}} = \frac{1}{\sqrt{\sum_X S_X^2 B_X N_\tau}}. \tag{1.32}$$

The sensitivity S_X, the branching ratio B_X and the corresponding relative weight $S_X^2 B_X$ for the different decay modes are reported in Table 1.3. One can easily check that the error on P_τ is improved by almost a factor two compared to $\tau \to \pi\nu$ when all the decay modes are combined.

Chapter 2

The Experimental Apparatus

The experimental apparatus is presented in this chapter. After a description of the LEP machine, the DELPHI detector is presented in more detail. A brief description of the DELPHI software is also given.

2.1 The LEP Collider

At the beginning of the eighties, the european community of high energy physics based at CERN decided to build a Large Electron-Positron collider, LEP. The physics motivation was the precise measurement of the Z^0 and W boson properties. Thus, the accelerator was designed to operate, in its first phase (LEP 1), at centre of mass energies around 90 GeV. In a second phase, LEP will be operated up to 200 GeV to study essentially $W^\pm$ physics (LEP 200). In this Section, a brief description of the LEP complex is given. For a more detailed presentation see [18].

LEP is located on the franco-swiss border near Geneva at CERN and measures about 27 km in circumference. The 3.8 m diameter tunnel is situated 50 to 100 m below the surface.

LEP consists of a single ring, having the shape of an octagon, with eight arcs alternating with eight straight sections. Thus, when traveling along the ring, the beams meet eight times the same configuration : one 500 m long straight section followed by one 2800 m long arc. Electron and positron beams are maintained on a circular orbit by 3368 dipole magnets installed in the arcs. The beams are focused by 808 quadrupole magnets positioned both along the straight sections and the arcs of the ring. The collisions of the electron and positron beams take place at the centres of the straight sections. Four underground areas located every second beam intersection point are fully equipped with detectors (ALEPH, DELPHI, L3 and OPAL).

The electron and positron beams circulate in a 10 cm high and 25 cm wide aluminum tube where the vacuum is required to be in the low range of 10^{-9} Torr. In the neighbourhood of the intersection points, the vacuum is further reduced to, at least, 2.10^{-10} Torr in order to decrease beam particle interactions with residual gas molecules.

The positron and electron beams are injected into the LEP collider after having been pre-accelerated by a series of accelerators. In order (see figure 2.1): the LEP Injector Linac (LIL), the Electron Positron Accumulating ring (EPA), the Proton Synchrotron (PS) and the Super Proton Synchrotron (SPS). Inside the LIL, electrons or positrons are accelerated up to 600 MeV before being injected into the EPA where they are accumulated and cooled by synchrotron radiation. They are then injected into the PS where they are accelerated up to 3.5 GeV. Then, they are sent into the SPS for a further acceleration up to 20 GeV. Finally, bunches of electrons and positrons are transferred into the LEP ring. Four bunches per beam circulate in opposite direction and intersect in the four points where the experimental areas are installed. The acceleration of the beams is accomplished by a series of radio-frequency cavities, which also compensate for the synchrotron radiation losses along the rings.
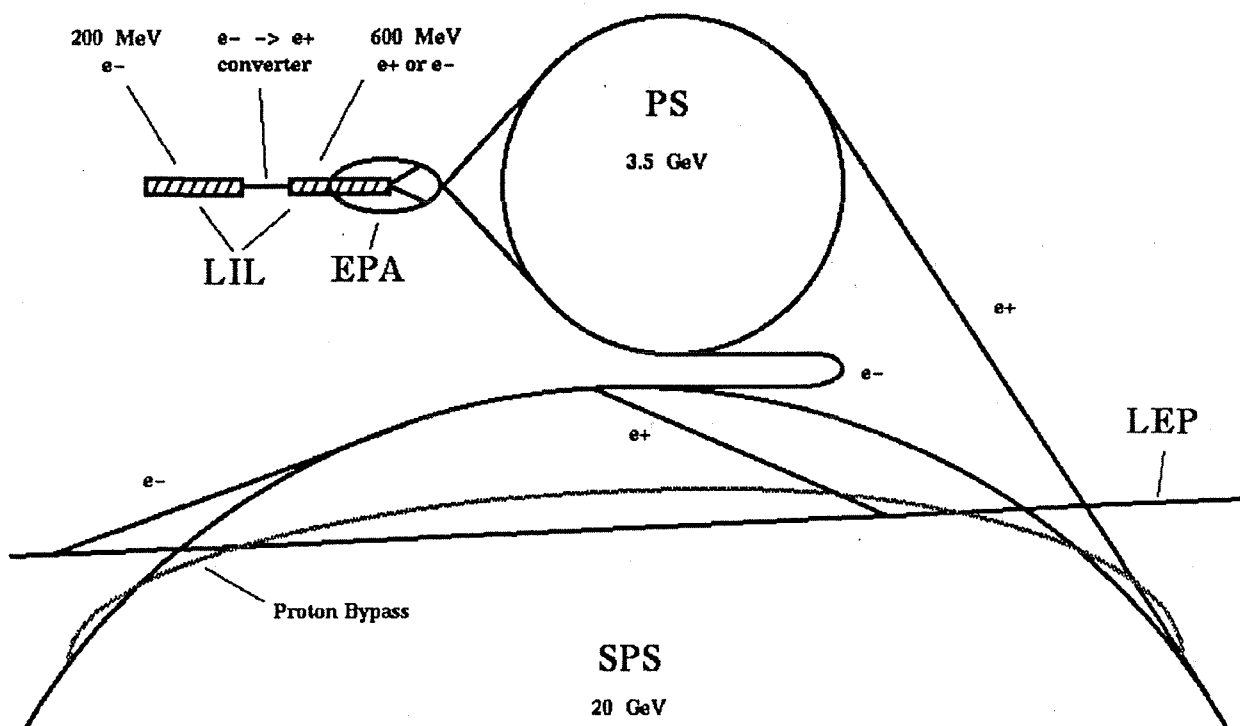
Figure 2.1: *Schematic view of the LEP injection system, which includes the two stage LEP Injector Linacs (LIL), the Electron Positron Accumulator (EPA), the Proton Synchrotron (PS), the Super Proton Synchrotron (SPS) and the LEP ring itself. The 10 MeV electron gun close to the e^- → e^+ converter is not shown.*

Two fundamental parameters provide the link between accelerator performances and physics results: the beam energy and the accelerator luminosity. In general, physics processes depend on the energy in the centre of mass. In particular, the Z^0 production is characterized by a strong resonant behaviour, and the maximum cross section ($\sigma \simeq 40$ nb) is obtained for energy in the centre of mass $\simeq M_{Z^0}$. The product of the luminosity $\mathcal{L}$ times the cross section σ of a given physics process determines the event production rate: $N = \mathcal{L} \cdot \sigma \cdot t$, where t is the data

taking time. Thus, once the cross section for a given physics process is fixed by the energy in the centre of mass, the number of events produced is determined by the luminosity and the data taking time. The luminosity is given by:

$$\mathcal{L} = \frac{n_e n_p k f}{4\pi \sigma_x \sigma_y} cm^{-2} s^{-1} \qquad (2.1)$$

where n_e and n_p are the numbers of electrons and positrons in each bunch ($\simeq 4.10^{11}$ particles), k is the number of bunches in each LEP beam (*i.e.* k=4), f is the revolution frequency and σ_x and σ_y are the horizontal and vertical r.m.s. beam overlapping widths at the intersection points. The high luminosity reached by LEP ($\mathcal{L} \simeq 10^{31}$ cm^{-2} s^{-1}) is achieved by reducing the values of σ_x and σ_y at the interaction region. Superconducting quadrupoles placed a few metres away from the intersection points 'squeeze' the beams in the interaction point to a size of $\simeq 300$ μm in the x direction[1] and $\simeq 12$ μm in the y direction.

The LEP collider is a Z^0 'factory': with a luminosity $\mathcal{L}$ of $10^{31} cm^{-2}$ s^{-1} and a cross section of 40 nb, the production rate is about 1440 Z^0 per hour.

2.2   The DELPHI Detector

The name DELPHI stands for DEtector for Lepton, Photon, Hadron Identification. The general layout is shown in Fig. 2.2. The ensemble consists of a cylindrical section, the barrel, and two end-caps, and it covers almost 4π solid angle around the interaction point. The transverse and longitudinal views of the detector are shown in Figs. 2.3-2.4. In Cartesian coordinates the z axis is parallel to the beam with positive z in the direction of the incident electron beam; the x direction is towards the centre of the LEP ring and y is in the vertical direction. In polar coordinates θ is the angle from the positive z axis and ϕ is the angle in the $x - y$ plane measured anticlockwise from the positive x axis. The radius r is the absolute distance from the z axis.

DELPHI is a general purpose detector for $e^+ e^-$ physics at LEP. It is composed by 17 sub-detectors with specific functions. An homogeneous magnetic field of 1.2 Tesla, provided by a superconducting magnet with diameter of 5.2 m and 7.2 m length, allows the determination of the charge and momentum of charged particles through the curvature of the corresponding tracks reconstructed in the tracking detectors. Given the high track multiplicity (typically 20 tracks are produced by an hadronic decay of the Z^0), tracking detectors have a fine spatial granularity, which allows the separation of close by tracks. Electromagnetic and hadronic calorimeters are used to identify neutral particles. In particular, photons are reconstructed with fine spatial granularity in the High-density Projection Chamber (HPC). A peculiar feature of the DELPHI detector is its ability of particle identification, which combines the properties of the main tracking device (Time Projection Chamber, TPC) with the Ring Imaging Cherenkov (RICH) technique, allowing the separation of protons, pions and kaons over a large momentum range.

[1] z is the direction along the beam axis and xz defines the plane of the accelerator.
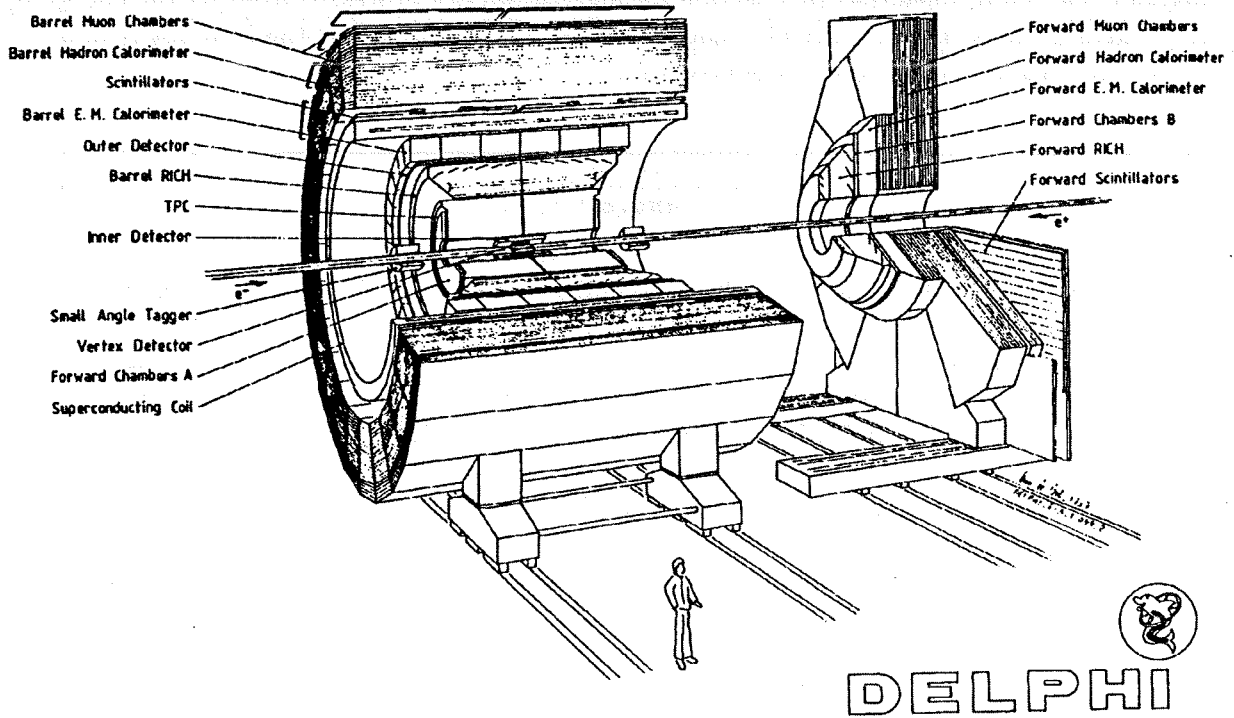
Figure 2.2: *Perspective view of the DELPHI detector, showing the general arrangement of detector components in the barrel and end-caps.*

A full list of DELPHI detector components and a brief summary of their structure and purpose is given below. The important sub-detectors in the specific analysis discussed in this thesis are explained in greater detail in subsequent Sections. A full description can be found in [19].

- **Microvertex detector (VD), Inner detector (ID), Time Projection Chamber (TPC) and Outer detector (OD)** are the tracking devices in the barrel region (see Section 2.2.1). Combining the ID, TPC and OD track elements, the momentum resolution in the barrel measured with muon pairs of $p = 45.6$ GeV is:

$$\frac{\sigma_p}{p} = 0.0015 \cdot \frac{p}{1 \text{ GeV}} \ . \tag{2.2}$$

When the microvertex detector is included in the track fit, the momentum resolution improves by almost a factor 2. The azimuthal track resolution measured with the ID, TPC and OD is:

$$\sigma_{r\phi} = 90 \ \mu\text{m} \ . \tag{2.3}$$

The track impact parameter in the r-ϕ plane measured by the VD detector is:

$$\sigma_{impact} = \sqrt{\left(\frac{69 \ \mu m}{p_t/1 \text{ GeV}}\right)^2 + 24^2 \ \mu m^2} \ . \tag{2.4}$$

- **Forward Chambers (FCA, FCB)** cover the end-cap region from $\theta = 33^0$ to $\theta = 11^0$ (and the symmetrical region between $\theta = 147^0$ and $\theta = 169^0$). They consist of layers of
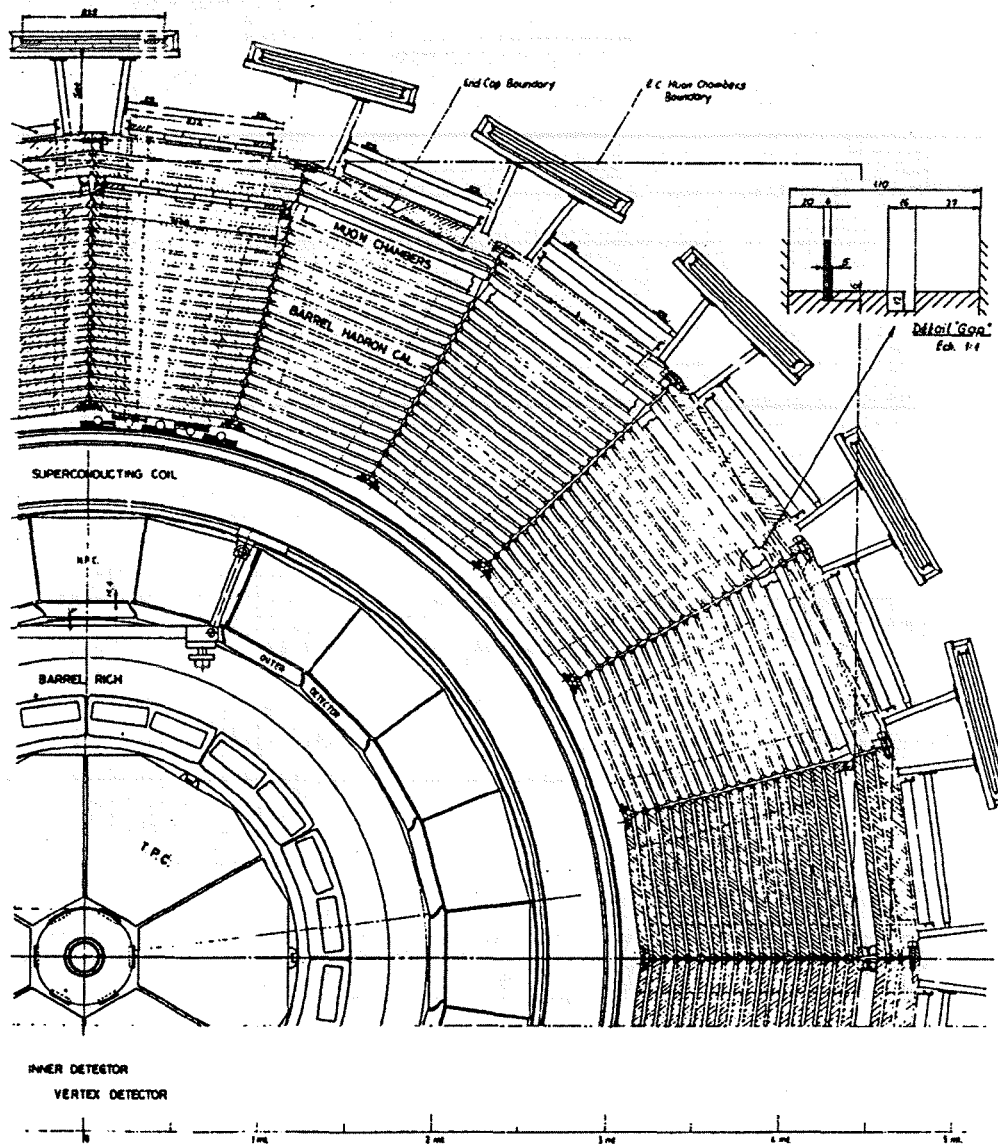
Figure 2.3: *Schematic view of the DELPHI detector along the beam pipe.*

drift chambers, mounted on both TPC endcaps (FCA) and between the forward RICH and the forward electromagnetic calorimeter (FCB). They provide fast trigger response and help the ID and TPC tracking in the forward region. The momentum resolution in the forward region with $(20^\circ \leq \theta \leq 35^\circ)$ is:

$$\frac{\sigma_p}{p} = 0.0037 \cdot \frac{p}{1\text{ GeV}} \quad , \qquad (2.5)$$

using the ID, TPC and Forward chambers information.

- **Rich Imaging Cherenkov counters (RICH)** use the detection of Cherenkov radiation to measure particle velocities and hence provide good particle identification over
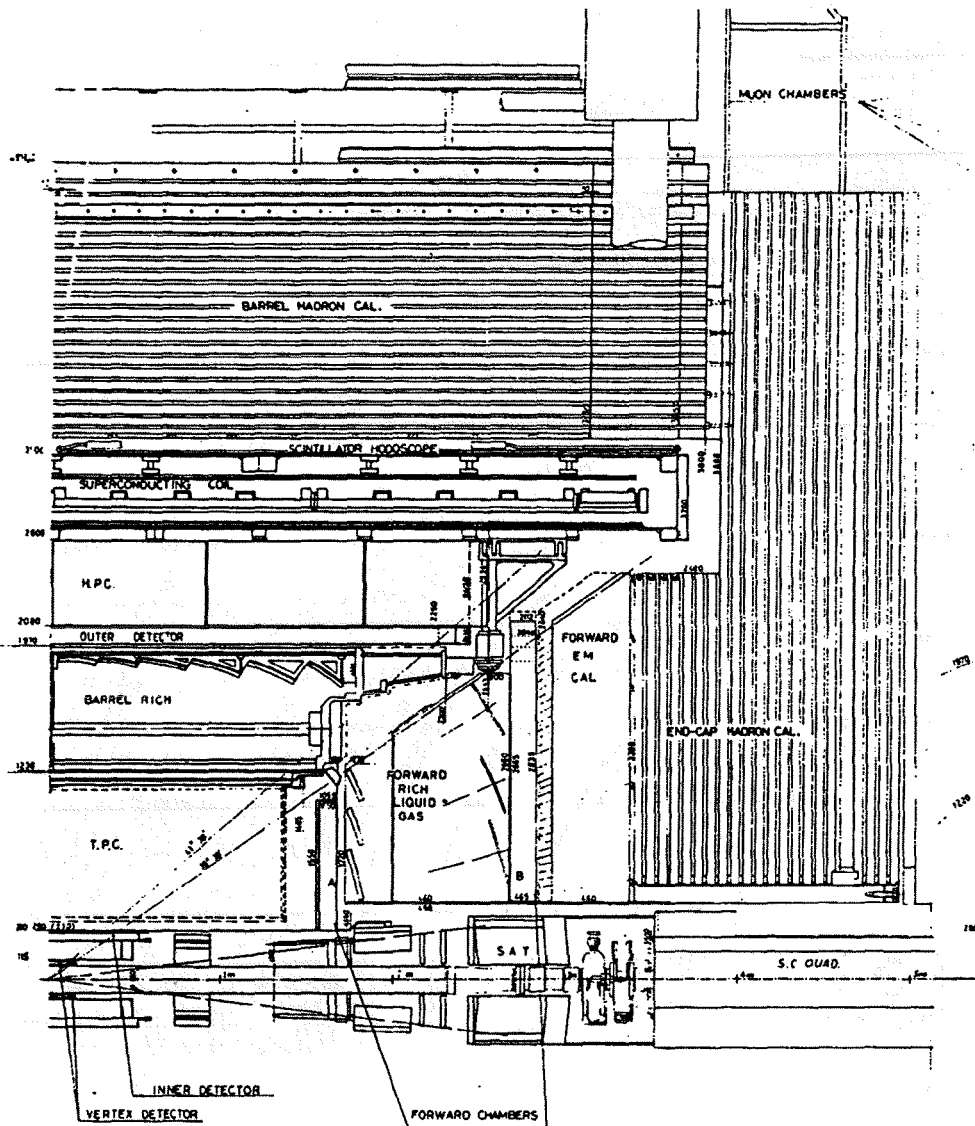
Figure 2.4: *Schematic view of the DELPHI detector perpendicular to the beam pipe.*

most of the momentum range of the particles detected in the DELPHI detector. This can be achieved using both gaseous and liquid radiators. The barrel RICH is now complete and fully operational. The forward part is partially operational.

- the **High-density Projection Chamber (HPC)** is the barrel electromagnetic calorimeter (see Section 2.2.2).

- The **Forward Electromagnetic Calorimeter (FEMC)** covers the angular region in θ between 10° and 36.5° and between 143.5° and 170°. It is made of 9064 (2×4532) lead glass scintillator blocks ($20\ X^{\circ}$ deep) with phototriode read out. FEMC also provides first level electromagnetic energy trigger information in less than 3 μs. The intrinsic energy resolution and accuracy in the shower position reconstruction as measured in a

test beam are:

$$\frac{\sigma(E)}{E} \simeq \left(0.35 + \frac{5.0}{\sqrt{E}}\right)\% \qquad (2.6)$$

$$\sigma(x,y) \simeq \frac{8.2}{\sqrt{E}} \, \text{mm} \qquad (2.7)$$

with E measured in GeV. In the DELPHI detector, the achieved fractional energy resolution is degraded by about a factor 4 because of the material in front of the calorimeter. The reconstruction of 45.5 GeV showers from e^+e^- events is $\frac{\sigma(E)}{E} \simeq 6\%$.

- **Scintillation Counters** are located both in the barrel (TOF) and in the end-cap (HOF) region. These counters consist of plastic scintillator strips equipped with photomultiplier readout. They provide a fast trigger response (less than 3 μs) and measure precisely the time of arrival of a particle, which help in removing background events such as cosmic muons at the trigger level. The measured time resolution is 1.2 ns for the TOF and 5 ns for the HOF counters.

- the **Hadron Calorimeter (HAC)** is built of 20 layers of plastic streamer tubes inserted into the 2 cm slots between the 5 cm thick iron plates of the segmented magnet return yoke in both barrel and end-caps. Hadronic showers are generated when incoming particles impact on the iron, and the streamer tubes sample the deposited energy in the layers between the modules. The HAC has four sampling layers and is in r-ϕ read out in projective towers of a typical size of $25 \times 25 \times 35$ cm^3. The energy resolution of the hadron calorimeter in about 98% of the solid angle is

$$\frac{\sigma_E}{E} = \frac{120}{\sqrt{E}}\% \quad , \qquad (2.8)$$

with E given in GeV .

- the **Muon Chambers (MUB, MUF)**, located in the barrel (MUB) and end-cap region (MUF), consist of two layers of drift tubes, which provide $r\phi$ information with a precision of $\simeq 4$ mm. The MUB have also a z position determination with $\simeq 2.5$ cm resolution.

- The **Small Angle Tagger (SAT)** is the principal luminosity monitor of DELPHI. Each arm is composed of an electromagnetic calorimeter and a track detector. The electromagnetic calorimeter covers an angular region in θ between 43 mrad and 120 mrad. It is made of eight 1 mm thick lead sheets placed in concentric rings around the beam axis, interspaced with 1 mm diameter scintillating fibers parallel to the beam axis. The track detector will consist of three planes of silicon strips placed in front of the lead scintillating fiber calorimeter. The luminosity is measured from the observed rate of Bhabha events $e^+e^- \rightarrow e^+e^-$ at small angle, whose cross section is very precisely known.

- The **Very Small Angle Tagger (VSAT)** is used to make an independent measure of the luminosity. Each arm consists of two rectangular W-Si calorimeter stacks, 24 X^0 deep, mounted at ± 7.7 m in z to both sides of the elliptic beam pipe. They cover polar angles from 5 to 7 mrad. This is also intended to measure single electron and photon background from the beams, and to check orbit position for LEP.

2.2.1   The Barrel Tracking Detectors

The microvertex Detector (VD)
This detector, which directly surrounds the beam pipe and covers an angular region in θ between 37° and 143°, is designed to have a high spatial resolution. It is made of three concentric shells of silicon microstrip detectors, located at at average radii of 6.3, 9 and 11 cm. The total amount of material traversed by a track is on average 1.5% of a radiation lenght. Each shell consists of 24 modules with about 10% overlap in ϕ between the modules. Each module consists of 4 silicon detectors, with strips parallel to the beam. The internal resolution of the VD detector has been measured to be 8 μm, and its impact parameter uncertainty is given by expression (2.4). The VD detector information, combined with the information obtained from the tracking chambers, is important for improving the primary vertex reconstruction but also for locating secondary vertices from the decays of short lived particles (with a lifetime of the order of 10^{-13} to 10^{-12} s) with a vertex reconstruction error of 80 μm in x, and 40 μm in y. It also provides a better separation of very close charged particle tracks.

The Inner Detector (ID)
The ID

- provides trigger information in $r\phi$ and z with a granularity of about one degree,

- measures charged particle track segments for an accurate extrapolation to the primary vertex, and

- separates charged particle tracks within a jet with an accuracy of 1 mm in $r\phi$.

The ID is composed of 2 concentric cylindrical chambers: a drift jet chamber surrounded by a set of 5 coaxial multiwire proportional chambers. The jet chamber measures with high accuracy the $r\phi$ coordinate, while the multiwire chambers measure in addition the z coordinate.

The jet chamber (11.6 cm $\leq r \leq$ 23 cm) is a classical cylindrical drift chamber covering an angular region in θ between 17° and 163° and segmented in 24 ϕ modules. It provides up to 24 coordinates at different radii with an accuracy in the $r\phi$ direction of 90 μm per point.

The coaxial multiwire proportional chambers (23 cm $\leq r \leq$ 28 cm) cover an angular region in θ between 30° and 150°. They provide up to 5 points, each with a precision $\sigma_z <$ 1 mm. These layers allow the ID to be used in the first level trigger due to their very short read out time (t < 3 μs).

The overall two track separation in the Inner Detector is about 900 μm.

The Time Projection Chamber (TPC)
The TPC is the main tracking detector in DELPHI and is used for:

- efficient charged particle track reconstruction with three-dimensional information and momentum determination,and

- the measurement of $\frac{dE}{dx}$ for particle identification.

The TPC is a cylindrical drift chamber with an inner radius of 35 cm, an outer radius of 111 cm and a length of 2×150 cm. It covers an angular region in θ between 20° and 160°. The TPC is divided into two identical symmetric halves at $z=0$. Each half is segmented in ϕ in six radial sectors.

The sectors are filled with a gas mixture of 80% argon and 20% methane operating at one atmosphere pressure. Particles traversing the sensitive gas volume create ionization along the trajectory. The free electrons, resulting from this ionization, drift under the influence of a uniform electric field parallel to the z axis to one of the end plates. There, they are detected by anode wires and cathode pads. The pads are disposed in 16 circular rows. The drift velocity is almost uniform and is about 65 μm/ns at the nominal voltage. The r and $r\phi$ positions of each point on the track are obtained from the cathode pad information and the z coordinate is calculated from the drift time measurement in the gas. The respective resolutions are 180 to 280 μm in $r\phi$, and less than 900 μm in z. These numbers are valid for at least three pad rows hit. Below the angular coverage mentioned above, the resolutions decrease rapidly. The overall two track separation is fixed by the geometrical pad segmentation (dimensions and separation) and is estimated to be 2 cm in $r\phi$ and 1 cm in z. On top of spatial information, it is also possible to get $\frac{dE}{dx}$ measurements in the TPC. It is performed by measuring the deposited charge in the anode wires. This quantity is directly associated to the ion density and to the ionization energy loss over the charged particle track length. This information can be used for particle identification. The $\frac{dE}{dx}$ resolution is at present 5.9% for muons of 45 GeV and 7.5% for pions between 280 and 400 MeV.

The Outer Detector (OD)
The OD provides:

- charged particle track positions with a good spatial resolution at 2 metres distance from the interaction region. Because the OD is able to measure particles at those large distances, the lever arm for the track reconstruction is increased and the momentum resolution for high momentum charged particles is greatly improved .

- trigger information in less than 3 μs. This may then be used by the first level trigger.

The OD also helps in the association of energy depositions in the barrel electromagnetic calorimeter with tracks detected in the TPC.

The OD detector consists of 24 identical overlapping modules at a radius between 197 and 208 cm and covering an angular region in θ between 43° and 137°. It is 486 cm long in z. Each module contains 5 layers of drift tubes operating in the limited streamer mode in a mixture of argon, isobutane and isopropanol. All layers provide $r\phi$ coordinates with an accuracy of better than 150 μm. Three of the layers provide in addition crude longitudinal information ($\sigma_z \simeq 5$ cm).
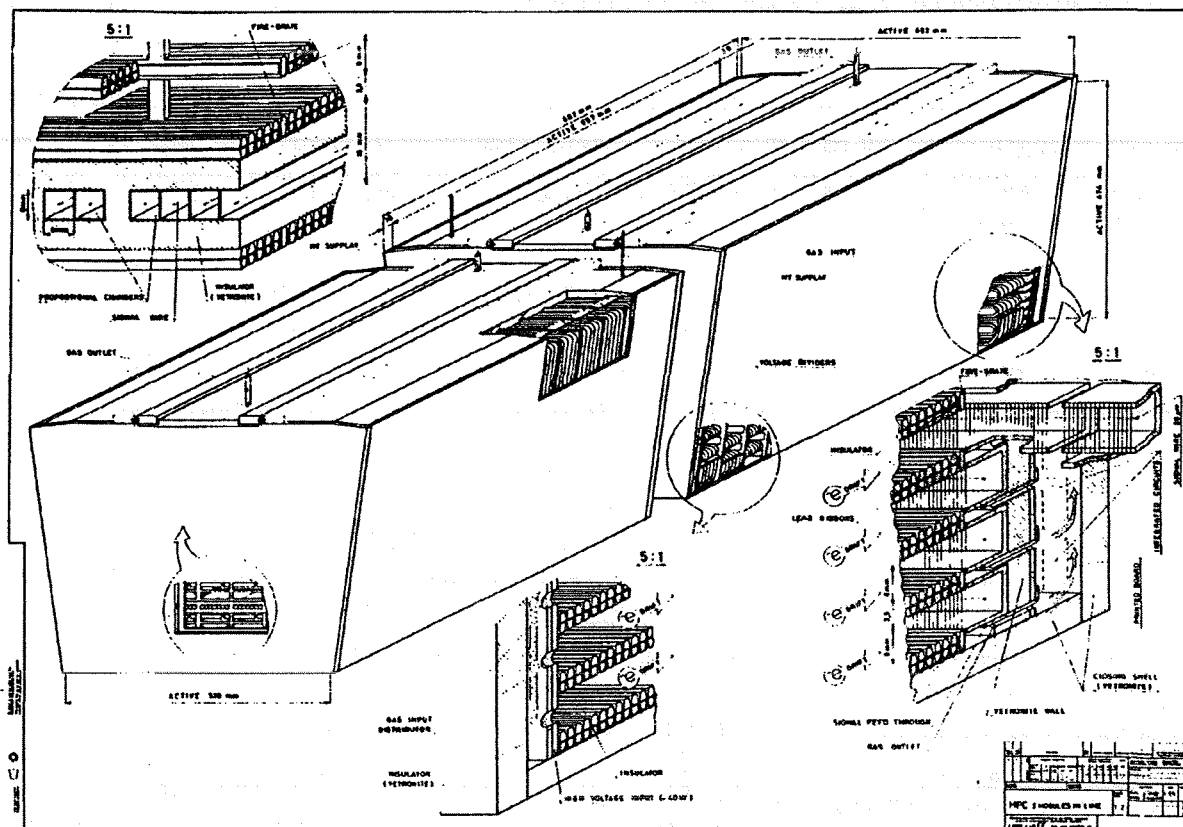
Figure 2.5: *The High Density Projection Chamber (HPC).*

2.2.2 The Barrel electromagnetic calorimeter

The High Density Projection Chamber (HPC) is the barrel electromagnetic calorimeter. The HPC technique as used in DELPHI provides not only reasonable energy resolution but also excellent spatial resolution for shower development. The HPC has a cylindrical structure and is placed inside the magnetic coil in order to minimize the thickness of the crossed matter. It is 505 cm long, has an inner radius of 208 cm and an outer radius of 260 cm. It is divided into 6 sectors along z and 24 sectors in ϕ covering the angular region $41.5^{\circ} < \theta < 138.5^{\circ}$. The HPC is therefore made of a total of 144 similar modules built with an accordion-like structure of lead wires. Inside each module, there is a series of layers formed with the lead wires providing about 18 radiation lengths (X_0). Between each layer, there is a 8 mm wide region containing a gaseous mixture $(Ar/CH_4\ 80/20\%)$. In Fig. 2.5, details of the mechanical construction are represented.

The working principle of the HPC is as follows. When a particle passes through a HPC module, it interacts electromagnetically with the lead accordion and produces an electromagnetic shower. By sampling the shower at very short intervals and measuring the deposited charge, the energy of the incoming particle is determined.

Ionization electrons drift under the influence of a longitudinal electric field, through the gaseous region, towards the end plates, where they are read out using a multiwire proportional chamber. The arrival position on the end plates gives $r\phi$ information and z is determined from the drift time. The subdivision of the HPC in 6 longitudinal sectors limits the maximum drift distance to about 85 cm.

A layer of scintillation counters is placed after 5 radiation lengths in each HPC module in order to provide a first level trigger.

The HPC has a good granularity and allows three-dimensional reconstruction of the shower position $(r, r\phi, z)$. Typical values for shower separation are about 4 mm along the drift direction and about 4 cm in azimuth. The achieved resolutions in the shower direction are:

$$\sigma_\theta \simeq \left(\frac{36}{\sqrt{E}} + 2.5\right) \text{ mrad}, \quad \sigma_\phi \simeq \left(\frac{97}{\sqrt{E}} + 10\right) \text{ mrad} \tag{2.9}$$

Recent data give the following value for the energy resolution:

$$\frac{\sigma(E)}{E} \simeq (7 + \frac{25}{\sqrt{E}})\% \tag{2.10}$$

where E is the energy measured in GeV.

2.3 The trigger

In this Section, the general structure of the DELPHI trigger is presented. A comprehensive description of the complete online system, which includes the Data Acquisition System (DAS), can be found in [20].

A fundamental role in the data taking chain is played by the trigger system. The trigger system decides if the Data Acquisition System (DAS) has to write out a certain event to a data storage device (tape, cassette) or if DAS has to clear its buffers and wait for the next event.

At LEP, the bunch crossing repetition rate is 44 kHz. The maximum rate at which DAS can record events on a permanent storage is of a few Hz. It must be remembered that, at the design luminosity of LEP, 1.6×10^{31} cm^{-2} s^{-1}, the Z^0 rate would be ~ 0.5 Hz. At this luminosity, other potentially interesting events, like Bhabha scattering, can add a further 0.5-0.6 Hz.

The DELPHI collaboration designed a four-level trigger system to cope with all trigger requirements. During the first two years of operation only the first two levels have been implemented. Since 1992 the full trigger system is operational. In the four level trigger scheme, the first two levels are synchronous with the Beam Cross Over (BCO), which occurs every 22 μs. The trigger decisions for the first two levels (T1 and T2 respectively) are taken 3 and 40 μs after the BCO, respectively. The second level trigger uses data from detectors with long drift time,

causing the loss of one BCOs for an event having passed the first level trigger. If a positive second level decision is taken, another 4.5 ms are needed to free the Front End Buffers (FEBs) and to prepare for a next event. This implies that whenever there is a positive second level trigger decision, the experiment is 'blind' for the next ~ 200 BCOs. The third and fourth level filters are software triggers and are asynchronous with respect to BCO. The processing time is about 30 ms and 300-500 ms, respectively. The redundancy of the various components of the trigger has been used to study trigger efficiencies for hadronic and leptonic events of usual topologies. With a luminosity of about 8×10^{30} cm^{-2} s^{-1}, typical trigger rates are about 400 Hz for the first level and 2-4 Hz for the second level trigger. The third level trigger, which has been implemented in 1992, further reduces the trigger rate to 2-2.5 Hz. The fourth level trigger is used to tag the different event types.

2.4 The Offline System

The offline software consists of the following three main components

- DELGRA: the **DELPHI G**raphics program,

- DELSIM: the **DELPHI S**imulation program, and

- DELANA: the **DELPHI A**nalysis program.

The DELGRA 3-D interactive colour display program visualizes the detector response of an event. It is useful for investigation of the detector performance and for checks of the results of the analysis program, for example shower reconstruction and track fits. An example of a $\tau^+\tau^-$ event presented by DELGRA is shown in Fig. 2.6.

The DELSIM [21] Monte Carlo program consists of three different parts:

1. the input Monte Carlo generator,

2. the simulation of particle interaction with detector material, and

3. the signal response of each detector.

The input Monte Carlo generator is chosen according to the physical process one is interested in. The KORALZ [22] generator is used for the $\tau^+\tau^-$ final state.

Particles are tracked through the detector material, and their interactions are simulated taking into account electromagnetic processes (Compton scattering, pair production, bremsstrahlung, photon conversion, *etc.*), nuclear interaction and absorption, multiple scattering and decay of short lived particles.

Then, the response to particles crossing each subdetector is simulated, and the results are stored in a data bank structure analogous to the real 'raw data' events.

	TD	TE	TS	TK	TV	ST	PA
	44	45	0	8	0	0	0
Act	(44)	(48)	(0)	(9)	(9)	(0)	(0)
	0	0	0	0	0	0	0
Deact	(0)	(4)	(0)	(6)	(9)	(0)	(0)

DELPHI Interactive Analysis
Beam: 45.6 GeV   Run: 23438   DAS: 18-Jun-1991
                               03:22:19
Proc: 8-Mar-1992 Evt: 581   Scan: 29-Apr-1992
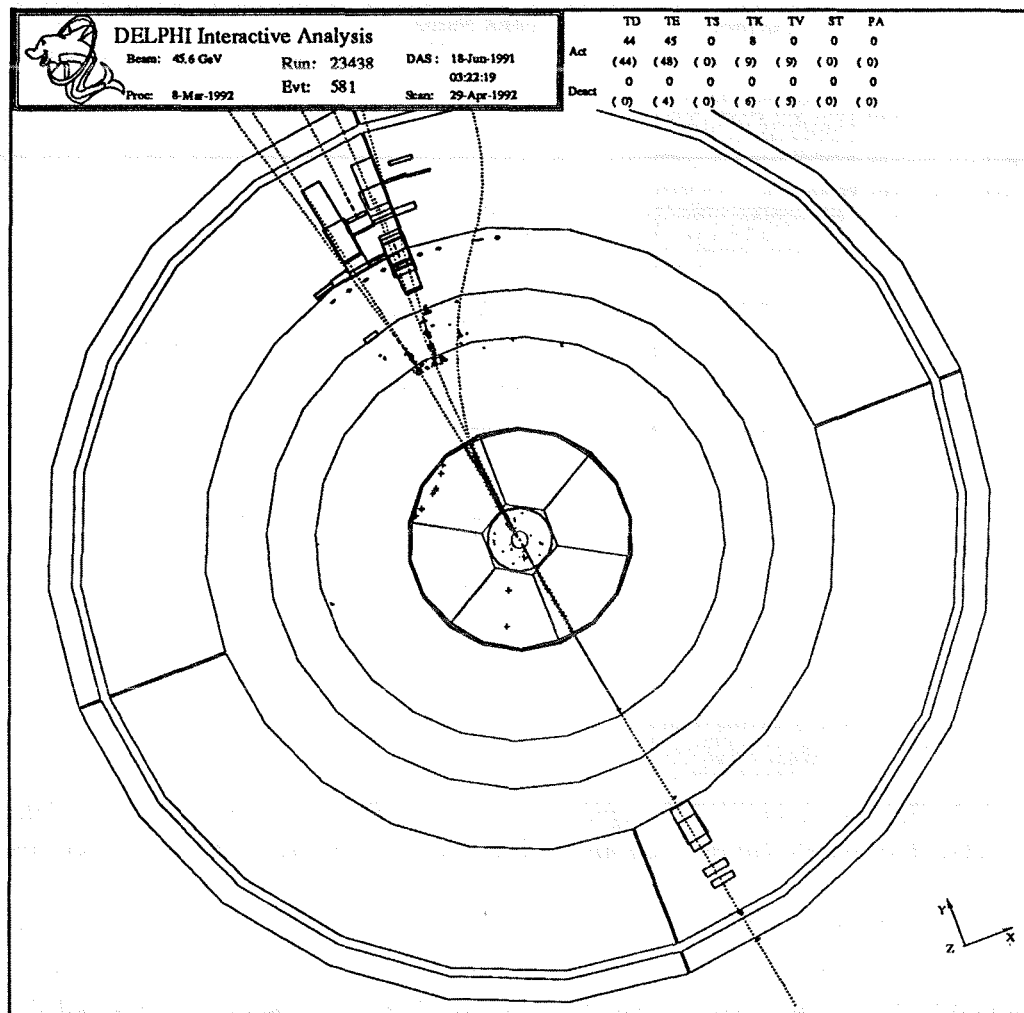
Figure 2.6: *A $\tau^+\tau^-$ event recorded with the DELPHI detector and presented with the DEL-GRA event display program. The charged tracks are represented with lines and the hits in the calorimeter with boxes. The event is viewed in the $r - \phi$ plane.*

The 'raw data', either from simulated or real events, are processed by the DELANA [23] analysis program. A scheme of the offline processing is shown in Fig. 2.7. The whole program is embedded in a data structure format called TANAGRA [24], and is divided into two parts, the first and the second stage pattern recognition. In the first stage pattern recognition, the 'raw data' are unpacked, calibrated and stored in a detector dependent TANAGRA format (TD banks). Then, the first stage pattern recognition algorithms combine the TD banks of each subdetector into track elements (TE), like tracks in the tracking detectors and showers in the calorimeters. In the second stage pattern recognition, track elements of the different tracking detectors are combined, and fitted to the hypothesis of a single track (TK). Then, tracks are extrapolated to the calorimeters, and showers are associated to the tracks. Unassociated showers in the electromagnetic calorimeter and in the hadronic calorimeter are considered photons

Action	Format	Bank Name	
	Raw Data		
	TANAGRA		
Calibration			
	TD	Patt. Rec Input	Frist Stage Pattern Recognition
Patt. Recogn.			
	TE	Track Element	
Track Search			
	TS	Track String	
Track Fit			
	TK	Fitted Track	Second Stage Pattern Recognition
Vertex Search			
	TB	Bundle of Tracks	
Vertex Fit			
	TV	Vertex	
Summary			
	DST		
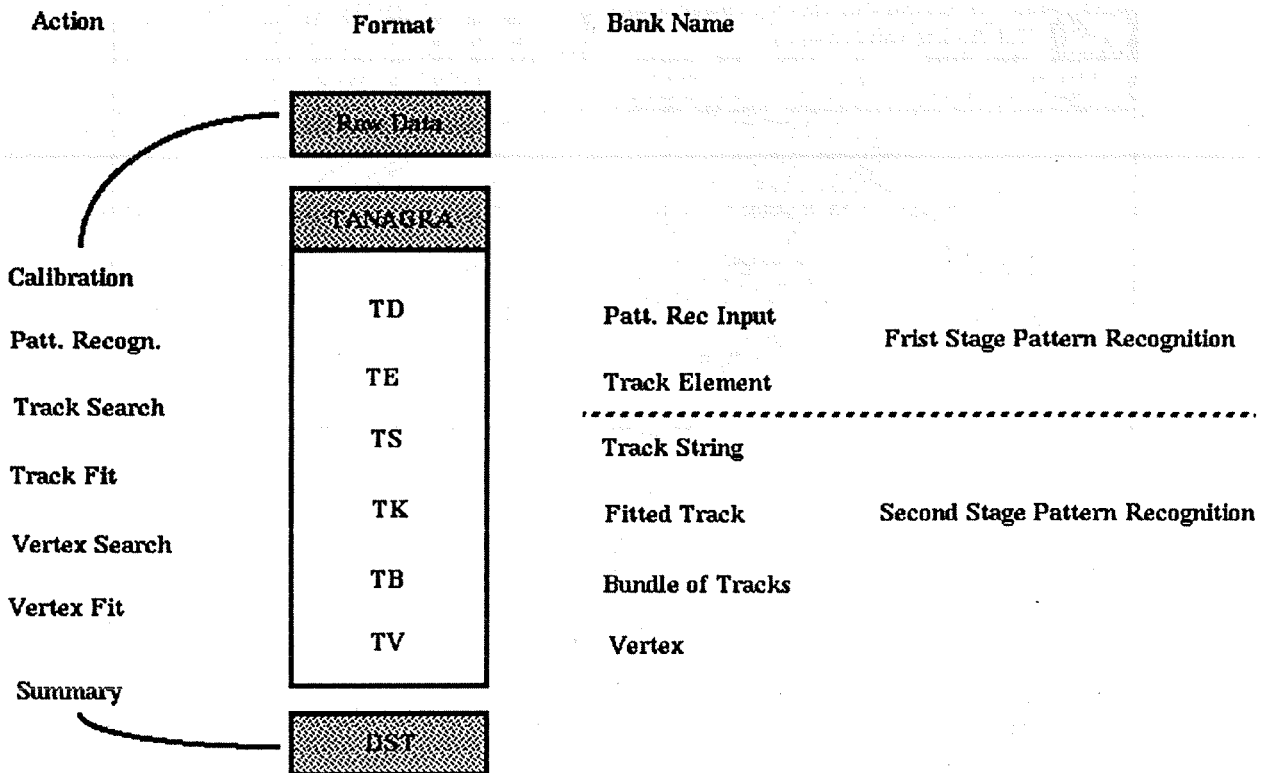
Figure 2.7: *Schematic view of the offline processing. The input are either simulated events or real data. For simplification they are called 'raw data' because the format is, apart from some details, the same. The steps from the TDs to the TVs are described in the text. Finally the Data Summary Tape (DST) is written out to reduce space and provide a faster data access.*

and neutral hadrons, respectively. Finally, a global fit to the tracks is performed in order to determine the production vertex, and track parameters are correspondingly recalculated (TV banks).

The fundamental information for the physics analysis is extracted from the TANAGRA structure and stored in a Data Summary Tape (DST).

Chapter 3

Measurement of the branching ratio $\tau \rightarrow 3\pi(n\gamma)\nu_\tau$

The importance of a precise measurement of the branching ratio $\tau \rightarrow 3\pi(n\gamma)\nu_\tau$ has been discussed in Chapter 1. Recently, ALEPH [8] and CELLO [9] have measured a significantly higher value of the $\tau \rightarrow 3\pi\nu_\tau$ branching ratio than previously, which helped them to claim to have solved the longstanding discrepancy in τ decays between the topological branching ratios and the sum of the exclusive branching ratios. However, ARGUS [10] still reports a significant discrepancy.

The branching ratio $Br(\tau \rightarrow X\nu_\tau)$, where $X = 3\pi n\gamma$ $(n \geq 0)$ and $X = 3\pi$, is readily obtained from the expression:

$$Br(\tau \rightarrow X\nu_\tau) = \frac{N_X(1 - f_{bkg}^{non-\tau \rightarrow X\nu_\tau})/\epsilon_{\tau \rightarrow X\nu_\tau}}{2N_{\tau^+\tau^-}(1 - f_{bkg}^{non-\tau})/\epsilon_\tau}, \tag{3.1}$$

where N_X is the number of $\tau \rightarrow X\nu_\tau$ candidates, $f_{bkg}^{non-\tau \rightarrow X\nu_\tau}$ is the background fraction in the $\tau \rightarrow X\nu_\tau$ sample which includes both contributions from other τ decay modes and from non-τ sources, $\epsilon_{\tau \rightarrow X\nu_\tau}$ is the efficiency for selecting $\tau \rightarrow X\nu_\tau$, $N_{\tau^+\tau^-}$ is the number of $e^+e^- \rightarrow \tau^+\tau^-$ events selected from the data, $f_{bkg}^{non-\tau}$ is the expected background fraction, of non-τ events in the tt sample and ϵ_τ is the efficiency for selecting $\tau^+\tau^-$ events.

In this chapter the criteria used for selecting τ events and for identifying the $\tau \rightarrow 3\pi(n\gamma)\nu_\tau$ decays are described. The goal is the determination of the branching ratio through expression 3.1. Throughout this chapter, $\tau \rightarrow 3\pi n\gamma\nu_\tau$ should always be understood with $n \geq 0$ unless otherwise specified, and $\tau \rightarrow 3\pi(n\gamma)\nu_\tau$ refers to both $\tau \rightarrow 3\pi n\gamma\nu_\tau$ and $\tau \rightarrow 3\pi\nu_\tau$ decays. The notation $\tau \rightarrow 3\pi\nu_\tau$ explicitly excludes all events with photons.

3.1   Selection of $e^+e^- \to \tau^+\tau^-$ events

Due to the τ decay properties and its high energy at the Z^0 peak, a $\tau^+\tau^-$ event may be characterized by two low-multiplicity, approximately back-to-back jets of particles. The neutrinos coming from τ decays will, in addition, result in a significant missing energy in the event.

On the other hand, possible backgrounds also have clear signatures. Two high momentum tracks ($p_{tot} \simeq 2E_{beam}$) with small acollinearity[1] angle characterize a $Z^0 \to \mu^+\mu^-$ event. A $Z^0 \to e^+e^-$ event will leave, in addition, a large amount of energy in the electromagnetic calorimeters ($E_{tot} \simeq 2E_{beam}$). High multiplicity particle jets coming from the quark hadronization identify a $Z^0 \to q\bar{q}$ event. The two-photon processes ($e^+e^- \to e^+e^- f\bar{f}$) produce particle jets with low momentum and energy, and a large acollinearity angle.

To identify the τ jets, the event axis is defined using the thrust axis[2]. The plane perpendicular to it divides the event into two hemispheres corresponding to each τ. In order to be independent of the number of charged tracks in the hemisphere, the most energetic track of each side is chosen to define the corresponding τ quantities. To define calorimetric energies, a cone of 30^0 (half opening angle) around the charged track is defined and all deposited electromagnetic energy inside it is added as the τ energy. Given the high Lorentz boost, almost all the τ decay products are contained inside the chosen cone.

To ensure a good detector response, it is required to have the event in the barrel region ($43^0 < \theta < 137^0$). As the $e^+e^- \to \tau^+\tau^-$ are acollinear events, the requirement that both τ's be within this polar angle range is too strict. It is seen that allowing one of the τ's to be outside this region does not introduce higher systematic errors and recovers an appreciable number of events. Thus, the criteria of having at least one leading track in the barrel is used.

A first set of cuts is applied to remove $e^+e^- \to q\bar{q}$ and $e^+e^- \to e^+e^- f\bar{f}$ events:

- $2 \leq N_{trk} \leq 6$

- $\theta_{iso} \geq 160^0$

- $E_{vis} > 8$ GeV

where N_{trk} is the number of 'good' charged tracks, θ_{iso} is the minimum angle between two tracks in opposite hemispheres and E_{vis} is the total energy, computed by adding the charged particle momenta and the neutral electromagnetic energies. A track is considered 'good' if it comes from a fiducial region around the interaction point, in particular if the impact parameter r of the track is within 5 cm of the interaction point and the longitudinal (along

---

[1] The acollinearity of a two tracks event is defined as 180^0 minus the angle between the two tracks.

[2] The thrust T is defined as:

$$T = max \frac{\sum_i |\vec{p}_i \cdot \vec{n}_i|}{\sum_i |\vec{p}_i|},$$

where $\vec{p}_i$ is the momentum vector of particle i and the sums are over all the particles in the event. The vector $\vec{n}_i$ which maximizes the sum gives the direction of the thrust axis.
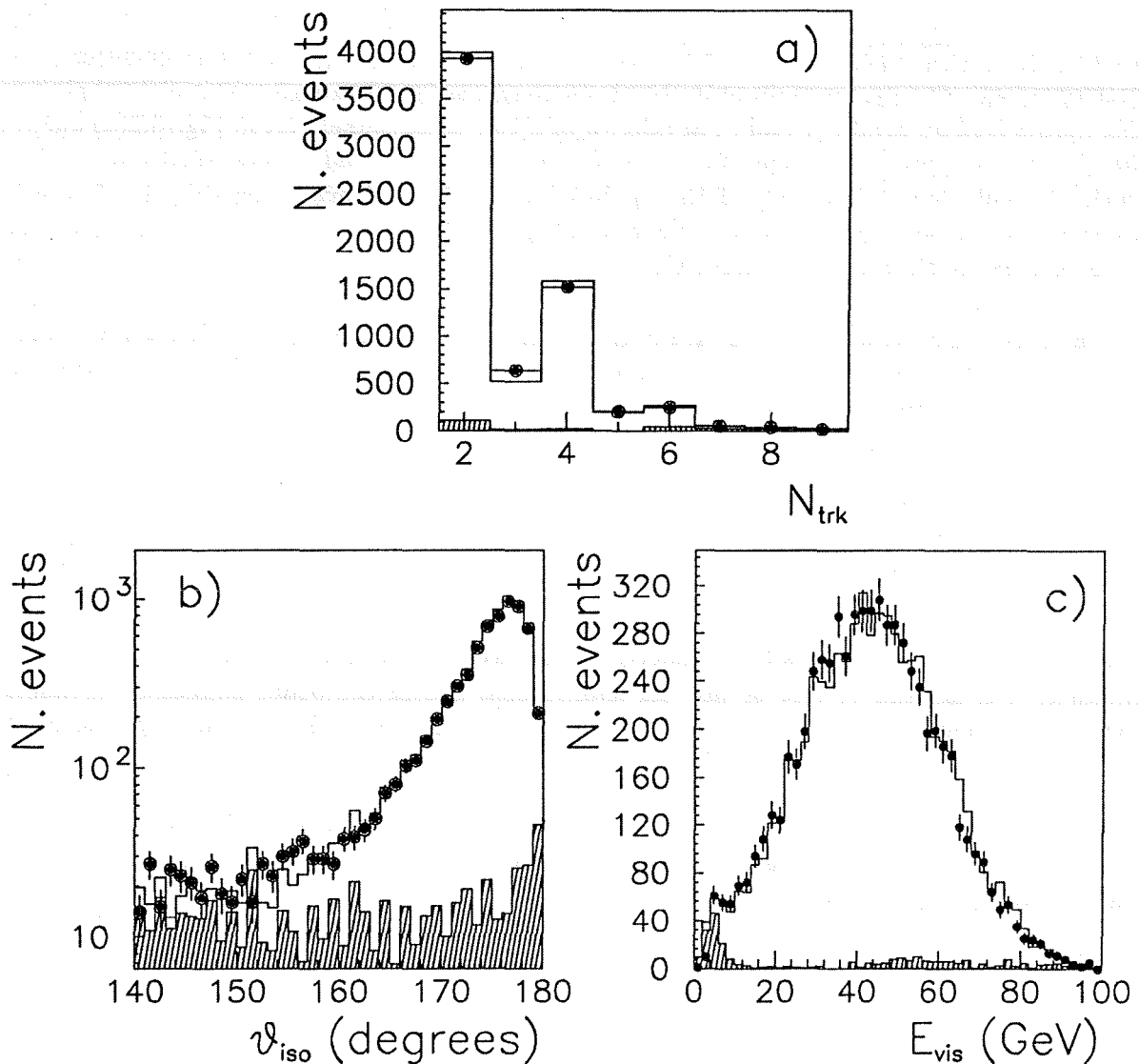
Figure 3.1: *a) Track multiplicity, b) isolation angle, and c) visible energy for the selected* τ *sample. All the* τ *selection cuts are applied, except the one relative to the variable which is plotted. The full line represents the Monte Carlo expectation for* $\tau^+\tau^-$ *plus the background, the hatched area shows the expected Monte Carlo background and the dots represent the data.*

beam direction) distance z between the point of closest approach and the interaction point is within 10 cm. Distributions of these variables for data and simulated events ($\tau^+\tau^-$ and backgrounds) are shown in Fig. 3.1(a-c).

The following cuts are used to reject the leptonic decays $Z^0 \rightarrow e^+e^-, \mu^+\mu^-$:

- $P_{rad} < 1$

- $E_{rad} < 1$

where $P_{rad} = \sqrt{p_1^2 + p_2^2}$, $E_{rad} = \sqrt{E_1^2 + E_2^2}$, and $p_1(p_2)$ and $E_1(E_2)$ are the momentum and electromagnetic energy, normalized to the beam energy, assigned to each τ as explained above. The normalized momenta p_1 and p_2 are shown in a two-dimensional plot in Fig. 3.2(a) before the P_{rad} cut is applied. The leptonic decays $Z^0 \rightarrow e^+e^-, \mu^+\mu^-$ tend to have their two leading track momenta (or at least one of them) close to $p = 1$. The events passing the P_{rad} cut are those inside the superimposed circle arc, where most $\tau^+\tau^-$ events lie. The P_{rad} and E_{rad} distributions are shown in Fig. 3.2(b-c).

Background events like cosmic rays passing through the detector or interaction of the beams with the gas molecules present inside the beam pipe are rejected by requiring the two leading tracks to come from a restricted region around the interaction point:

- $|z_1| < 4.5$ cm and $|z_2| < 4.5$ cm

- $|r_1| < 1.5$ cm and $|r_2| < 1.5$ cm

where r_1 and r_2 are the impact parameter of the two leading charged tracks respect to the interaction point and z_1 and z_2 are the longitudinal (along the beam direction) distances between the point of closest approach and the interaction point. The z position of the track point of closest approach is shown in Fig. 3.3(a).

After all these cuts, the background is strongly reduced, but there are still some cosmic and $e^+e^- \rightarrow e^+e^- f\bar{f}$ events remaining. As they are mostly two-prong events, new cuts are applied only for two-prong events.

- $\theta_{acol} > 0.5^0$

- $|z_1 - z_2| < 3$ cm

- $|\vec{P}_T| > 0.4$ GeV

where θ_{acol} is the acollinearity of the event and $\vec{P}_T$ is the transverse component of the total momentum of the event (adding momenta vectorially). The acollinearity distribution for two-prong events is shown in Fig. 3.3(b).

The total number of selected $e^+e^- \rightarrow \tau^+\tau^-$ events is 6528 for an integrated luminosity of 10.4 pb^{-1} collected in the 1991 LEP run. The selected sample of $\tau^+\tau^-$ events is used in the DELPHI τ physics analysis group as a common basis for cross sections and forward-backward asymmetry measurements as well as branching ratios and τ polarization measurements. In the following, the aspects of efficiency and background estimate, which are related to the $\tau \rightarrow 3\pi(n\gamma)\nu_\tau$ branching ratio measurement, will be discussed. A more complete presentation can be found in [31].
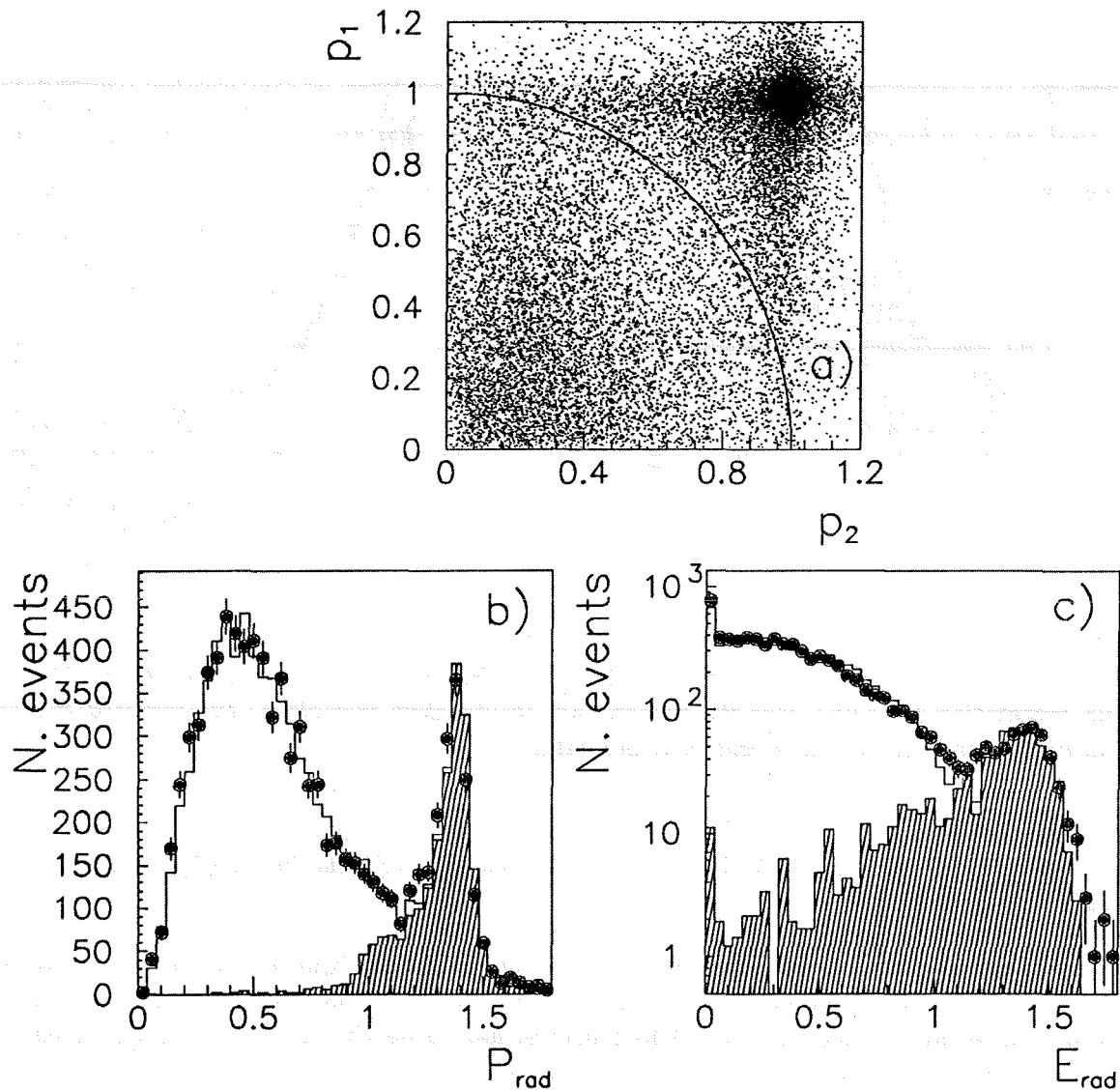
Figure 3.2: a) p_1 versus p_2 for leptonic events (data) with the cut line corresponding to $P_{rad} < 1$ superimposed. p_1 and p_2 are the momenta of the leading tracks in hemispheres 1 and 2 respectively. b) the P_{rad} distribution, c) the E_{rad} distribution. All the τ selection cuts are applied, except the one relative to the variable which is plotted. The full line histogram represents the Monte Carlo expectation for $\tau^+\tau^-$ plus the background, the hatched area shows the expected Monte Carlo background and the dots represent the data.

3.1.1 Efficiency calculation

The selection efficiency has been determined from a complete Monte Carlo simulation. The KORALZ [22] Monte Carlo program is used to generate $e^+e^- \to Z^0 \to \tau^+\tau^-$ events. Radiative corrections are properly taken into account in the program. The detector response is simulated
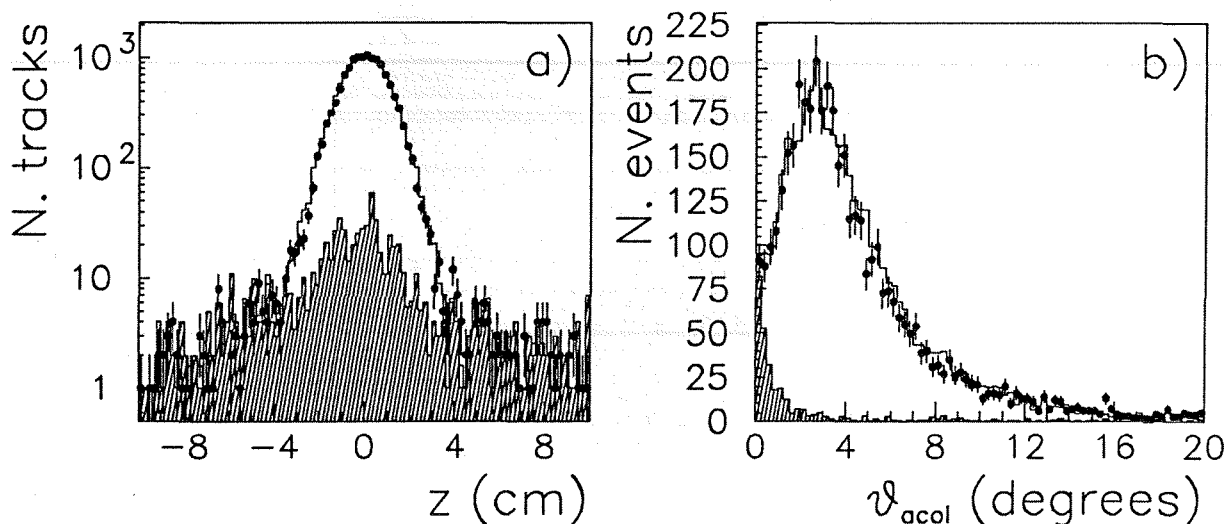
Figure 3.3: *a) The z position of the track point of closest approach to the vertex, b) the acollinearity distribution for two-prong events. All the τ selection cuts are applied, except the one relative to the variable which is plotted. The full line histogram represents the Monte Carlo expectation for $\tau^+\tau^-$ plus the background, the hatched area shows the expected Monte Carlo background and the dots represent the data.*

with DELSIM [21], and the standard DELPHI analysis programs (DELANA [23]) are used to reconstruct the event characteristics. Then, the selection criteria discussed in the previous Section are applied.

The selection efficiency ϵ_τ is given by the ratio of the Monte Carlo $\tau^+\tau^-$ events passing the selection cuts to the number of generated $\tau^+\tau^-$ events in the full solid angle. Its value estimated from Monte Carlo, $\epsilon_\tau = 53.43 \pm 0.18\%$, has to be corrected for small differences between data and simulation:

1. TPC cracks are not perfectly modelled in Monte Carlo (0.9935 ± 0.0025),

2. electromagnetic energy resolution is worse in the data (0.9975 ± 0.0010),

3. the P_{rad} distribution is slightly shifted (1.002 ± 0.002), and

4. the impact parameter distribution is wider in data (0.997 ± 0.002).

Dead areas in the TPC exist in azimuth ϕ at the boundaries between the six TPC sectors and at $\theta = 90°$ where the two halves of the TPC are separated by a wall. The first correction factor is computed from the differences between data and Monte Carlo in the ϕ distribution of the tracks folded in 60°. More details will be given in Section 3.6.1, where the effect is studied for the $\tau \to 3\pi(n\gamma)\nu_\tau$ branching ratio measurements. The Monte Carlo simulation reproduces well the crack region around $\theta = 90°$, and no correction is needed. The second

correction factor is obtained directly by smearing the Monte Carlo, according to the resolution obtained from the data. In the third case, a fit to the dimuon P_{rad} peak is done both in data and Monte Carlo. A shift downwards of the mean value of the data with respect to the Monte Carlo of 0.8% is observed. It is assumed that this is a linear effect, and thus P_{rad} is rescaled in all simulated events, giving the 1.002 factor above. To compute the last correction factor, a similar procedure as for the second factor is used.

The data have been collected at different centre of mass energies around the Z^0 mass. Thus, the efficiency has been checked with $\tau^+\tau^-$ events generated at different energy points and simulated with a simplified detector response (FASTSIM [27]). The effect is found to be negligible.

A test of all the variables used for the selection is done in the following way. All the cuts are applied except the one which is investigated; several distributions can be seen in Figs. 3.1, 3.2 and 3.3. In each case, the resolution of the variable is estimated and the cut is varied by the corresponding resolution, computing the relative variation in the number of selected events in data and Monte Carlo. The main contributions to this systematic error estimate come from E_{rad} ($\frac{\Delta \epsilon_\tau}{\epsilon_\tau} = 0.3\%$), θ_{acol} (0.2%) and θ_{iso} (0.1%).

The trigger efficiency is calculated by studying a set of independent and redundant trigger components, and is found to be $99.9 \pm 0.1\%$.

Another possible systematic error comes from the uncertainty in $\sin^2\theta_W$, which affects the momentum and energy distributions, through P_τ. From a study of generated $\tau\tau$ events for $\sin^2\theta_W$ varying from 0.22 to 0.24, this effect is estimated to be less than 0.05 %.

Finally, the uncertainty on τ branching ratios can introduce an error if any decay mode is biased. Due to the well-known tau decay problem (see Section 1.1), the sum of the measured branching ratios of all decay channels is less than 100%, while in the Monte Carlo the sum must be 100%. This means that the exclusive branching ratios in any τ generator are not exactly Particle Data Group values (PDG) [6], but they are tuned to fit the topological branching ratios (which are better understood) increasing the ratios of the worst known channels near to the maxima allowed by existing measurements. In Table 3.1 the efficiencies for the main decay channels simulated by KORALZ as well as for the different topologies are summarized. The possible bias is expected to be small, since the efficiencies for the various decay modes are similar. Varying the branching ratio values within the experimental errors of PDG, one finds that the only important contribution comes from the multipion final states, and even this one is small ($\Delta\epsilon = 0.06\%$).

After all corrections and assuming that all systematic sources are independent (adding the errors in quadrature), an efficiency $\epsilon_\tau = 52.82 \pm 0.33\%$ is obtained. This is equivalent to $81.9 \pm 0.5\%$ within the fiducial region. All errors are summarized in Table 3.2.

3.1.2 Background estimate

The backgrounds have been estimated directly from the data, and the results checked with simulated events : $e^+e^- \rightarrow e^+e^-$ generated with BABAMC [26], $e^+e^- \rightarrow \mu^+\mu^-$ with DYMU3

	ϵ_i (%)
$\tau^- \to e^- \bar{\nu}_e \nu_\tau$	53.5 ± 0.3
$\tau^- \to \mu^- \bar{\nu}_\mu \nu_\tau$	56.7 ± 0.3
$\tau^- \to \pi^- \nu_\tau$	51.4 ± 0.4
$\tau^- \to \rho^- \nu_\tau$	53.7 ± 0.3
$\tau^- \to a_1^- \nu_\tau \ (2\pi^- \pi^+)$	51.8 ± 0.4
$\tau^- \to a_1^- \nu_\tau \ (\pi^- 2\pi^0)$	52.8 ± 0.4
$\tau^- \to n\pi$	50.2 ± 0.4
$\tau \to 1 \ prong$	53.8 ± 0.1
$\tau \to 3 \ prong$	50.9 ± 0.3

Table 3.1: *Selection efficiency for different τ decays (and their charge conjugates) estimated from Monte Carlo. $n\pi$ stands for every multipion final state not mentioned above.*

source	$\Delta\epsilon_\tau / \epsilon_\tau$ (%)
TPC ϕ cracks correction	0.2
P_{rad} shift correction	0.2
impact parameter correction	0.15
E_{rad}	0.35
acollinearity	0.2
isolation	0.1
MC stat	0.34
P_{tau} and BR assumed in MC	0.1
total on efficiency	0.63
	$\Delta f_{bkg}^{non\tau} / f_{bkg}^{non-\tau}$ (%)
$\mu^+\mu^-$	0.2
e^+e^-	0.4
$q\bar{q}$	0.3
two-photon	0.1
total on background	0.55
total	0.84

Table 3.2: *Systematic error summary for the selection (above) and background subtraction (below).*

[25], $e^+e^- \to q\bar{q}$ with LUND 7.3 [29] and $e^+e^- \to e^+e^- f\bar{f}$ with the Berends-Daverveldt-Kleiss Monte Carlo [30].

To compute the background from the data, the most significant variable used in the selection to remove a particular kind of background is chosen. Then all cuts are applied, except the cut corresponding to this variable (as is done for Fig. 3.1 to 3.3), giving a distribution with two overlapping zones each dominated by signal or background. At this stage, to enhance the background events (making easier the estimate) an identification procedure is applied to select background and reject $\tau^+\tau^-$ events, so that the sample is dominated by the kind of background events which are to be studied. The distribution for these events in data and Monte Carlo is plotted, and, looking at the shape of the MC distribution, an extrapolation
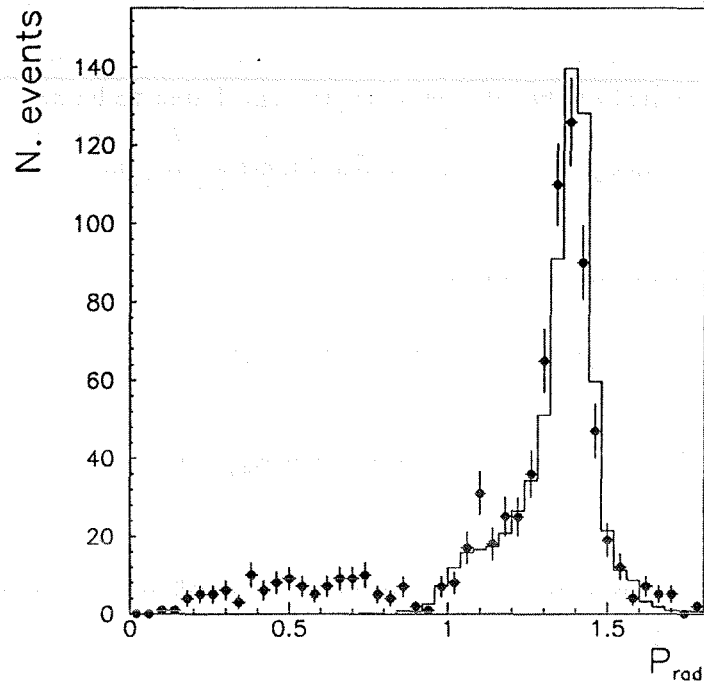
Figure 3.4: *The P_{rad} distribution (dots) for selected $\mu^+\mu^-$ in the $\tau^+\tau^-$ data sample before the P_{rad} cut. The solid line is the same distribution for simulated $e^+e^- \to \mu^+\mu^-$ events.*

is done from the zone dominated by the background to the zone dominated by $\tau^+\tau^-$. From this extrapolation it is possible to estimate the number of background events inside the data sample.

In the case of $\mu^+\mu^-$, for example, the P_{rad} variable is used and the background enhancement is based on the Muon Chambers, requiring at least one hit associated to each leading track. The efficiency for $\mu^+\mu^-$ is 80% (due to the angular coverage of the chambers), while most $\tau^+\tau^-$ are removed, leaving only events where both taus decay into muons and a small fraction where one τ decays to a μ and the other to a hadron with 'punch through'. The P_{rad} distributions for these selected $\mu^+\mu^-$ events in the $\tau^+\tau^-$ sample before the P_{rad} cut and for simulated $e^+e^- \to \mu^+\mu^-$ are shown in Fig. 3.4. From the extrapolation to $P_{rad} < 1$, a value of $0.4 \pm 0.2\%$ is obtained for this background.

For the e^+e^-, E_{rad} is used in an analogous way. The background is enhanced requiring less than 2 GeV deposited in the hadron calorimeter in each side. From the extrapolation to $E_{rad} < 1$ the value $1.1 \pm 0.4\%$ is obtained.

Both for $q\bar{q}$ and $e^+e^- \to e^+e^-f\bar{f}$ events the distribution in isolation angle is used to estimate the background. The enhacement cuts are $E_{vis} > 20$ GeV for hadronic events and $E_{vis} < 15$ GeV for $e^+e^- \to e^+e^-f\bar{f}$, obtaining $0.8 \pm 0.3\%$ and $0.3 \pm 0.1\%$ respectively.

The background contamination estimated directly from the data has been crosschecked with

the Monte Carlo expectation for the various channels, and good agreement has been found for each background.

Finally, the possible remaining background from cosmic events has been checked using the time of flight measurement of the OD detector [28], and found to be negligible.

The overall estimated background is $2.6 \pm 0.5\%$. All errors are summarized in Table 3.2.

3.1.3   Total number of τ events

Given the selected number of $\tau^+\tau^-$ candidates $N_{\tau^+\tau^-}$, the corrected total number of τ events is given by (*cf.* expression 3.1):

$$N_\tau^{corr} = 2 \frac{N_{\tau^+\tau^-}(1 - f_{bkg}^{non-\tau})}{\epsilon_\tau}. \tag{3.2}$$

The global systematic uncertainty on the corrected number of τ events is directly obtained from Table 3.2, *i.e.* $\frac{\Delta N_\tau^{corr}}{N_\tau^{corr}} = 0.84~\%$.

The final values which will be used for the $\tau \to 3\pi(n\gamma)\nu_\tau$ branching ratio measurement through expression 3.1 are reported in Table 3.3.

$N_{\tau^+\tau^-}$	6528
$\epsilon_\tau~(\%)$	52.82 ± 0.33
$f_{bkg}^{non-\tau}~(\%)$	2.6 ± 0.5
N_τ^{corr}	$24075 \pm 298 \pm 202$

Table 3.3: *The number of selected $\tau^+\tau^-$ events $(N_{\tau^+\tau^-})$, the $\tau^+\tau^-$ selection efficiency (in 4π solid angle) (ϵ_τ), the background fraction in the τ sample $(f_{bkg}^{non-\tau})$, and the corrected number of τ events (N_τ^{corr}). The first error on N_τ^{corr} is statistical, the second is systematic.*

3.2   Selection of $\tau \to 3\pi(n\gamma)\nu_\tau$ candidates

Once a low background $e^+e^- \to \tau^+\tau^-$ sample has been selected from the data, further cuts are applied in order to identify the $\tau \to 3\pi(n\gamma)\nu_\tau$ decays. Three tracks coming from the interaction region are the clear signature for this kind of event. The absence of photons in the same hemisphere will distinguish $\tau \to 3\pi\nu_\tau$ from $\tau \to 3\pi n\gamma\nu_\tau$. The main source of background comes from other types of τ decays, in which the apparent topology is not the true topology, e.g. if a photon converts to an e^+e^- pair. A radiative $\tau \to e\nu\bar{\nu}\gamma$, where the photon converts into a e^+e^- pair before it reaches the TPC, will fake a three-track event. Similarly, a $\tau \to \rho\nu \to \pi\pi^0$ event will appear as a three-prong τ if one of the photons coming from the π^0 decay converts or (less frequently) the π^0 decays with a Dalitz pair $(\pi^0 \to \gamma e^+e^-)$. However, photon conversions tend to accumulate in regions of the detector where significant material is located (typically after the microvertex detector). In addition, two tracks coming

from a converted photon show correlations in their kinematics.

The decay $\tau \to K^*\nu_\tau \to K_S\pi\nu_\tau \to \pi\pi\pi\nu_\tau$ will also produce three tracks in the detector. However, the vertex of the two charged pions from the K_S decay generally will be found to be far from the interaction point, given the K_S lifetime. Thus, this decay will not be considered a signal for the $\tau \to 3\pi(n\gamma)\nu_\tau$ analysis presented here, but it will be included in the background (see Section 3.4). Only a small fraction of the background comes from non-τ events, mainly radiative Bhabhas $e^+e^- \to e^+e^-\gamma$, $e^+e^- \to q\bar{q}$ with a low multiplicity of charged tracks, and the two-photon process $e^+e^- \to e^+e^-\tau^+\tau^-$.

The first step in the selection of $\tau \to 3\pi n\gamma\nu_\tau$ events is to isolate τ jets with three 'good' tracks coming from a fiducial region around the interaction point (5 cm in r and 10 cm in z). The term 'three-prong hemisphere' will be used to refer to those τ decays with three charged particles. The sum of the charges of the tracks should be equal to unity in absolute value. The vectorial sum of the charged track momenta is required to have its polar angle in the range $43^\circ < \theta < 137^\circ$.

The background from two-photon processes and radiative Bhabha events is eliminated by the cuts:

- $P^{3\pi}_{vis} > 10$ GeV

- $E_{e.m.} < 55$ GeV

where $P^{3\pi}_{vis}$ is the sum of the charged track momenta and $E_{e.m.}$ is the total electromagnetic energy of the event. In Fig. 3.5(a-b) the corresponding distributions for data and Monte Carlo are shown.

The initial requirement of having three tracks originating from the interaction region already rejects quite a few photon conversions. However, many of them still remain and additional cuts are necessary to get rid of this kind of background. Most of the conversions take place after the microvertex detector, which accounts for only $\simeq 1.5\%$ of a radiation length of material, and thus the corresponding e^+e^- tracks are not expected to produce a signal in the microvertex detector. On the contrary, given the high efficiency of the microvertex detector ($\simeq 97\%$ for isolated tracks coming from the interaction point), $\tau \to 3\pi n\gamma\nu_\tau$ events very rarely have less that two tracks with VD hits associated. A first cut is applied:

- at least two tracks with associated hits in the microvertex detector.

The number of tracks with associated VD hits for the $\tau \to 3\pi n\gamma\nu_\tau$ candidates is plotted in Fig. 3.6. However a π^0 Dalitz decay can still escape the previous cut. Also, some photon conversions which occur in the microvertex detector or have a false association of tracks with VD hits may pass this cut. To reject such events, a pair finding algorithm is used, which reconstructs the decay vertex of the photon. Since the magnetic field in DELPHI is perpendicular to the $r\phi$ plane, the projection of a track on this plane is a circle. Thus, two tracks coming from a common vertex appear in this plane as two circles, which in general intersect at two separate points. In order to choose between the two intersections, the intersection where
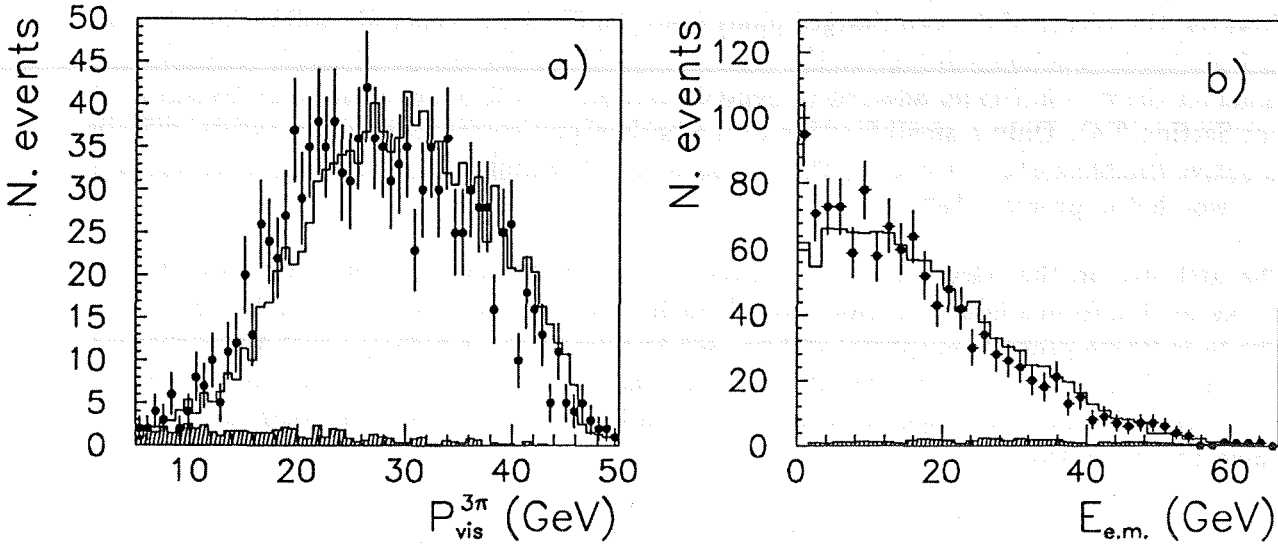
Figure 3.5: a) The visible momentum in the three-prong hemisphere $P_{vis}^{3\pi}$, b) the electromagnetic energy $E_{e.m.}$ for $\tau \to 3\pi n\gamma\nu_\tau$ candidates. The full line represents the Monte Carlo expectation for $\tau \to 3\pi n\gamma\nu_\tau$ plus the background, the hatched area shows the expected Monte Carlo background and the dots represent the data.

the two tracks are closer in z is considered as a first estimate of the vertex point. Starting from this point, the standard DELPHI vertex fitting algorithm [32] is applied to determine the best vertex, at which point the track parameters are finally recalculated. The two possible combinations of opposite charge pairs in a three-prong hemisphere undergo the procedure described above, and for each of them the difference, $\Delta\theta$, of the polar angles of the two tracks and the distance, R_{xy}, of the vertex from the interaction point in the $r\phi$ plane are calculated. Given the zero mass of the photon, photon conversions are caracterized by a small value of $\Delta\theta$. Moreover, photon conversions tend to accumulate starting from the beam pipe, which is located at 5.2 cm in the $r\phi$ plane, while practically all τ decay vertexes are contained within a few millimeters from the interaction point (τ average decay length is $\simeq$ 2.2 mm). To be kept, the two opposite charge combinations are thus required to satisfy one of the following conditions:

- $\Delta\theta \geq 0.3°$

- $\Delta\theta < 0.3°$ and $R_{xy} < 2$ cm.

The $\Delta\theta$ distribution and R_{xy} when $\Delta\theta < 0.3°$ are shown in Fig. 3.7(a-b).

In addition, the invariant mass of the three tracks is required to be:

- $m_{3\pi} < 2$ GeV,
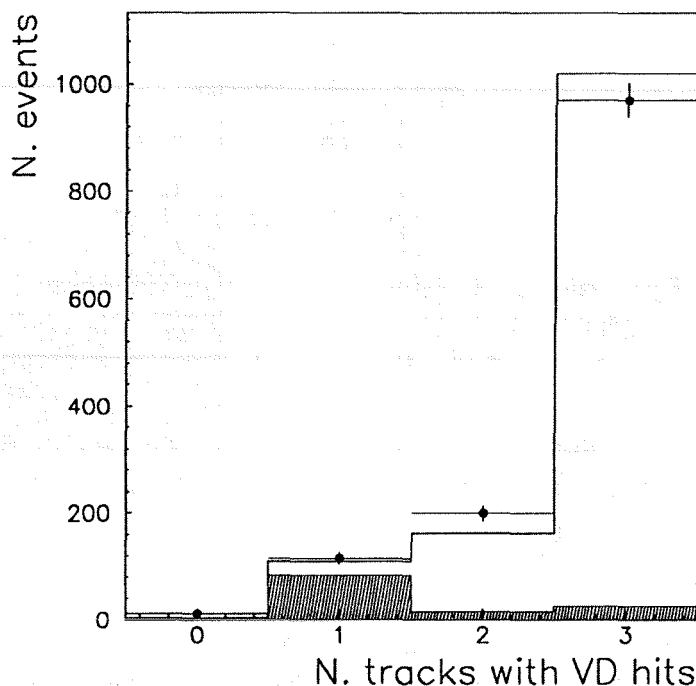
Figure 3.6: *The number of tracks with associated VD hits for the $\tau \rightarrow 3\pi n\gamma\nu_\tau$ candidates. The full line represents the Monte Carlo expectation for $\tau \rightarrow 3\pi n\gamma\nu_\tau$ plus the background, the hatched area shows the expected Monte Carlo background and the dots represent the data.*

which takes into account the fact that the 3π system is the product of a τ decay ($m_\tau \simeq 1.78$ GeV), and also ensures good track reconstruction. The invariant mass distribution of the three tracks is plotted in Fig. 3.8.

Thus far, the selection is valid for both $\tau \rightarrow 3\pi n\gamma\nu_\tau$ and $\tau \rightarrow 3\pi\nu_\tau$ decays. To proceed in the identification of $\tau \rightarrow 3\pi\nu_\tau$, events where the three prongs are accompanied by photons are rejected. A neutral electromagnetic shower is considered a photon if:

- it deposits energy in at least 3 HPC layers,

- it starts in the first three layers of HPC, and

- $E_\gamma > 0.5$ GeV.

Finally, the photon is assigned to the 3π hemisphere if:

- $\theta_{\gamma-3\pi} < 30^\circ$

where $\theta_{\gamma-3\pi}$ is the angle between the photon and the 3π momentum direction. In case the shower is found in the forward electromagnetic calorimeter only the last two cuts are used.
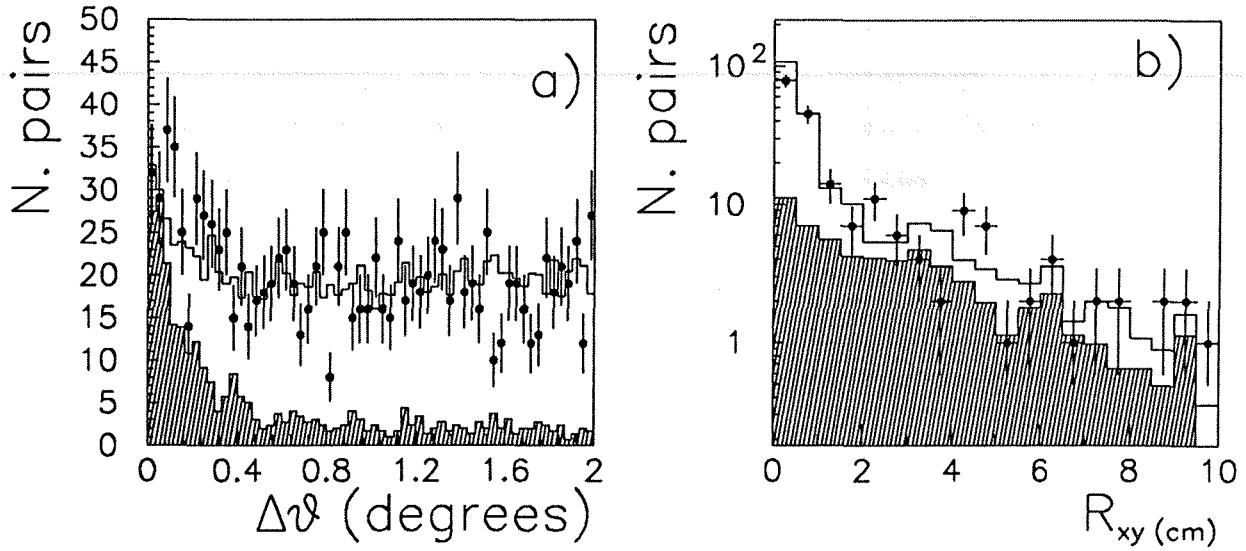
Figure 3.7: a) The $\Delta\theta$ distribution, b) R_{xy} when $\Delta\theta < 0.3°$ for the $\tau \to 3\pi n\gamma\nu_\tau$ candidates. The full line represents the Monte Carlo expectation for $\tau \to 3\pi n\gamma\nu_\tau$ plus the background, the hatched area shows the expected Monte Carlo background and the dots represent the data.

Given the high Lorentz boost, all the particles coming from the τ decay are collimated and will be found within a few degrees of the τ direction: the $\theta_{\gamma-3\pi}$ cut is, thus, mainly intended to reject possible noise in the detector. The requirement of energy deposit in at least 3 HPC layers also eliminates some noise and some wrong energy cluster associations in the pattern recognition. Hadronic interactions sometimes produce energy satellites around the charged track, which can fake a real photon. However, most of them are concentrated in the last HPC layers, and will be rejected by requiring an energy deposit in the first $\simeq 4$ radiation lengths (corresponding to 3 layers) where almost all the real photons have already started showering. The number of HPC layers with deposited energy for a neutral electromagnetic shower and the starting layer of the shower are plotted in Fig. 3.9(a-b). The neutral shower energy and the angle between the shower and the three prong direction are shown in Fig. 3.10(a-b). The number of photons per event in the $\tau \to 3\pi n\gamma\nu_\tau$ candidates is shown in Fig. 3.11.

Some $\tau \to 3\pi n\gamma\nu$ $(n > 0)$ can fake a $\tau \to 3\pi\nu_\tau$ event if the photons overlap with the charged tracks and are associated to them. To reject these events and further suppress photon conversions, an additional cut is applied:

- $\frac{E_5^{3\pi}}{P_{vis}^{3\pi}} < 0.2$

where $E_5^{3\pi}$ is computed summing the energy deposited in the first five layers of the HPC and associated to the tracks. In fact, a large fraction of the hadrons will be seen as minimum ionizing particles in the first layers of the electromagnetic calorimeter and will interact after the fifth layer, which corresponds to roughly 0.3 interaction lengths starting from the collision
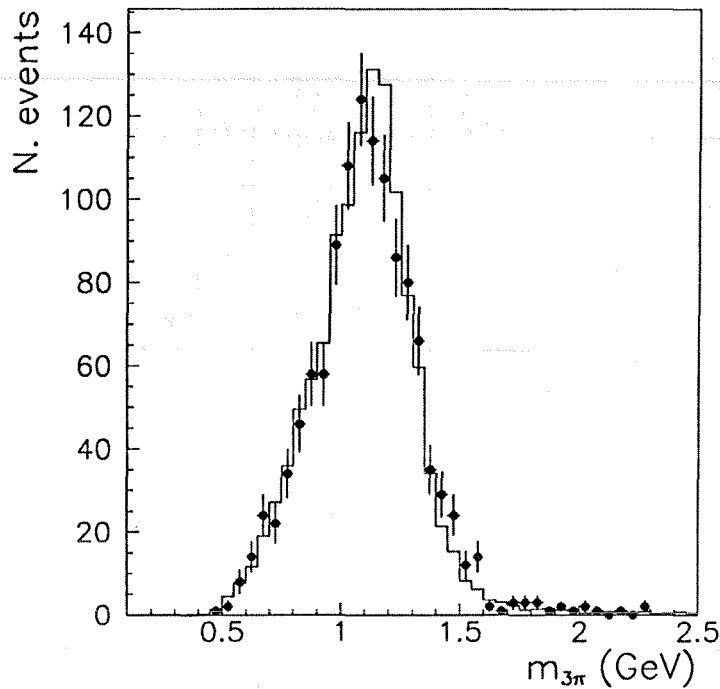
Figure 3.8: *The invariant mass of the three tracks for the $\tau \to 3\pi n\gamma\nu_\tau$ candidates. The full line represents the Monte Carlo expectation for $\tau \to 3\pi n\gamma\nu_\tau$ plus the background, and the dots represent the data.*

point. On the contrary, the electron and positron produced by a photon conversion will tend to release a large portion of their energy in the first five HPC layers ($\simeq$ 8 radiation lengths), thus increasing the ratio $E_5^{3\pi}/P_{vis}^{3\pi}$. The wrong association of a photon with a charged track produces a similar effect. The $E_5^{3\pi}/P_{vis}^{3\pi}$ distribution for the $\tau \to 3\pi\nu_\tau$ candidates is shown in Fig. 3.12.

3.3 Efficiency calculation

The selection efficiency has been determined from Monte Carlo simulation. The main features of the selection efficiency are reported in Table 3.4, where $\epsilon_\tau^{\tau \to 3\pi(n\gamma)\nu_\tau}$ is the efficiency (over 4π solid angle) of the τ selection for $\tau \to 3\pi(n\gamma)\nu_\tau$ (*cf.* Table 3.1), ϵ_{3-prg} is the efficiency of finding, after the τ selection, a $\tau \to 3\pi(n\gamma)\nu_\tau$ decay as a three-prong in the fiducial region, and ϵ_{sel} is the $\tau \to 3\pi(n\gamma)\nu_\tau$ selection efficiency, normalized to the number of three-prong events selected in the fiducial region. The total efficiency ϵ_{tot} in 4π solid angle is given by the product of the previous efficiencies. The $\epsilon_\tau^{\tau \to 3\pi(n\gamma)\nu_\tau}$ has been discussed in Section 3.1.1.

The probability that a $\tau \to 3\pi(n\gamma)\nu_\tau$ event, once selected, is seen as a three-prong event (ϵ_{3-prg}) is determined by either loss of tracks due to cracks in the TPC and overlap between very close tracks or by increase of tracks due to photon conversions.
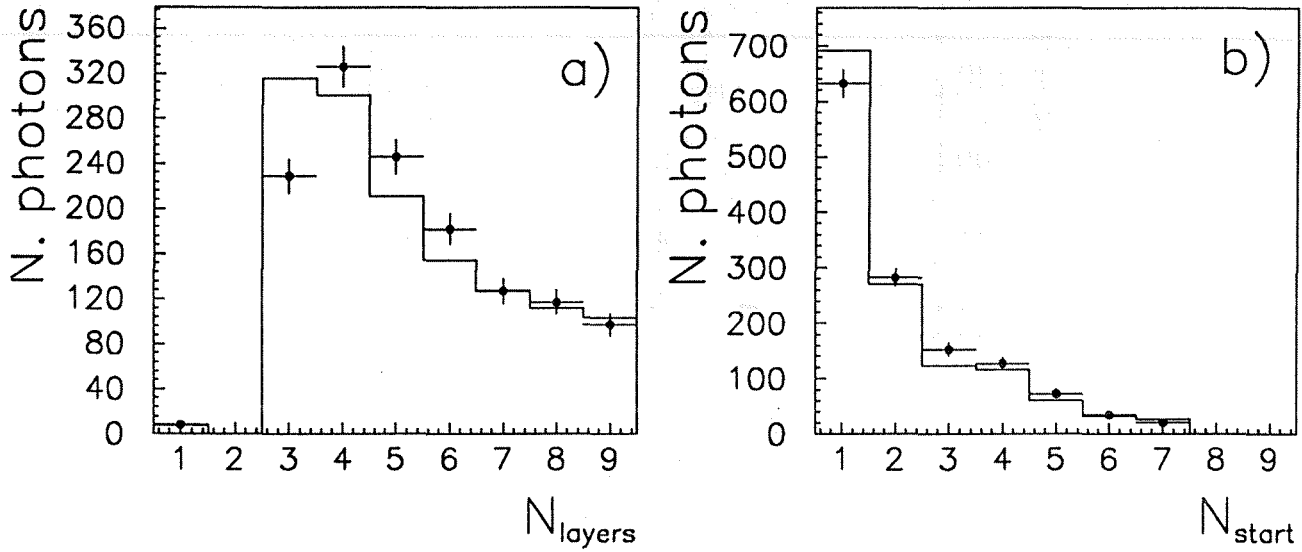
Figure 3.9: *a) The number of HPC layers with deposited energy for a neutral electromagnetic shower, b) the starting layer of the shower. The full line represents the Monte Carlo expectation and the dots represent the data. Showers with one layer hit in a) are located in the forward electromagnetic calorimeter.*
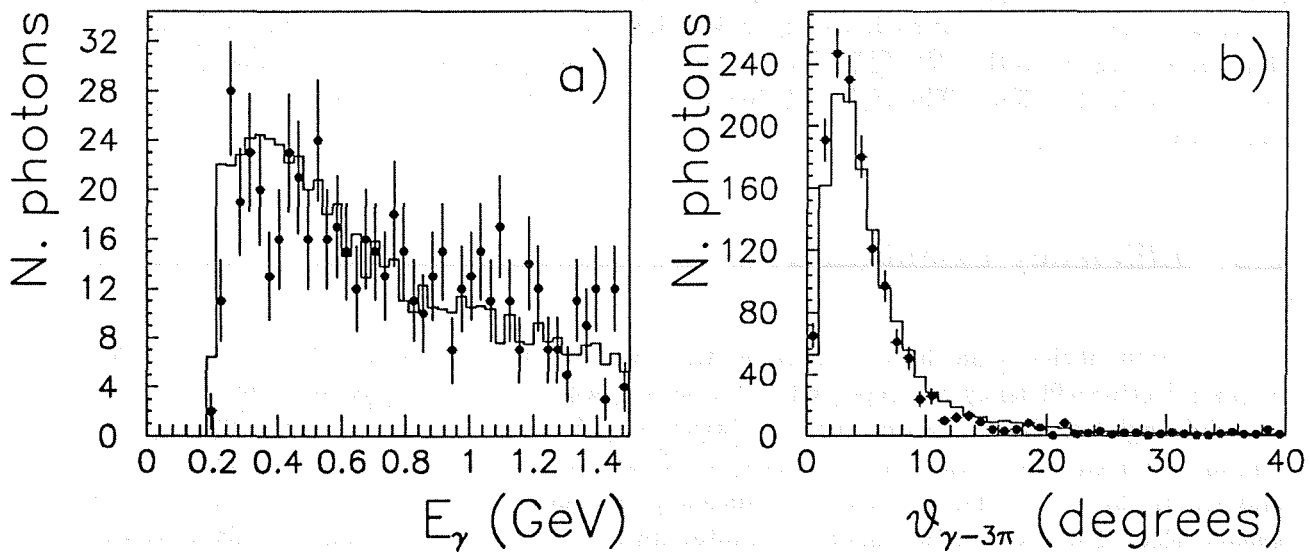
Figure 3.10: *a) The neutral shower energy, b) the angle between the shower and the three prong direction. The full line represents the Monte Carlo expectation and the dots represent the data.*
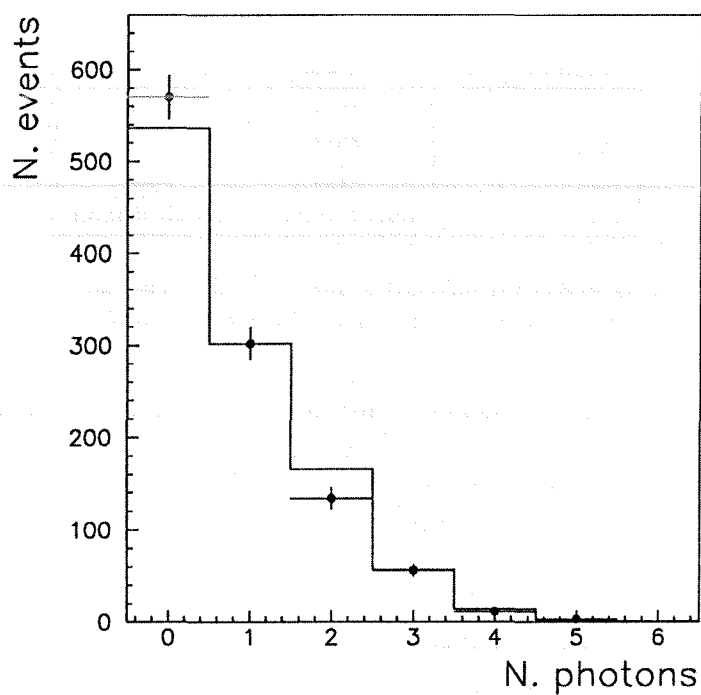
Figure 3.11: *The number of photons per event for the $\tau \to 3\pi n\gamma\nu_\tau$ candidates. The full line represents the Monte Carlo expectation and the dots represent the data.*
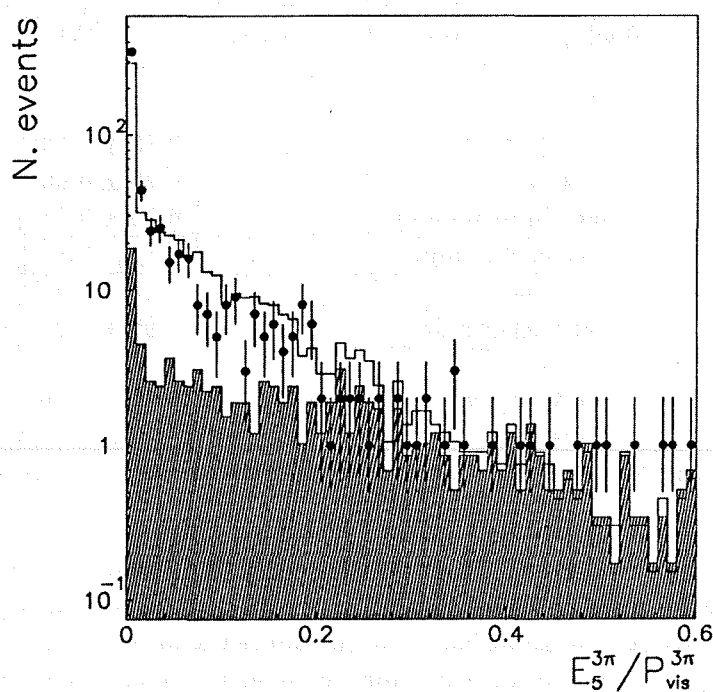
Figure 3.12: *The $E_5^{3\pi}/P_{vis}^{3\pi}$ distribution for the $\tau \to 3\pi\nu_\tau$ candidates. The full line represents the Monte Carlo expectation for $\tau \to 3\pi\nu_\tau$ plus the background, the hatched area shows the expected Monte Carlo background and the dots represent the data.*

efficiency (%)	$\tau \to 3\pi n\gamma\nu_\tau$	$\tau \to 3\pi\nu_\tau$
$\epsilon_\tau^{\tau \to 3\pi(n\gamma)\nu_\tau}$	50.8	51.8
ϵ_{3-prg}	75.2	77.7
ϵ_{sel}	91.0	65.2
ϵ_{tot}	34.74 ± 0.31	26.23 ± 0.39

Table 3.4: *Summary of selection efficiency for $\tau \to 3\pi n\gamma\nu_\tau$ and $\tau \to 3\pi\nu_\tau$. The quoted errors come from the Monte Carlo statistics used to determine the efficiencies.*

The actual selection efficiency ϵ_{sel} comes from the cuts described in Section 3.2.

The possibility of a systematic bias in the efficiencies and several crosschecks and systematic studies on data and Monte Carlo compatibility will be discussed in Section 3.6.

3.4   Background calculation

All the backgrounds have been obtained by applying the $\tau \to 3\pi(n\gamma)\nu_\tau$ selection on simulated events (*cf.* Section 3.1.2). The estimated values are reported in Tables 3.5 and 3.6.

$\tau \to 3\pi n\gamma\nu_\tau$ $(n \geq 0)$	
Backgrounds from other τ decays	f_{bkg} (%)
$\tau \to \rho\nu$	1.53 ± 0.13
$\tau \to \pi\pi^0\pi^0\nu$	1.11 ± 0.11
$\tau \to \pi\pi^0\pi^0\pi^0\nu$	0.80 ± 0.10
$\tau \to K^*\nu$	0.26 ± 0.05
others (multipions)	0.13 ± 0.04
Non-τ backgrounds	f_{bkg} (%)
$e^+e^- \to q\bar{q}$	0.10 ± 0.03
Total background	3.93 ± 0.21

Table 3.5: *Summary of background fractions in the $\tau \to 3\pi n\gamma\nu_\tau$ selection. The background contamination from processes other than those listed in this Table is negligible. The quoted errors come from the Monte Carlo statistics used to determine the backgrounds.*

The background to $\tau \to 3\pi n\gamma\nu_\tau$ decay is due mainly to one-prong τ events with photon conversions, while the main contribution to the $\tau \to 3\pi\nu_\tau$ background comes from $\tau \to 3\pi\pi^0\nu$ events. A detailed study of possible biases in the Monte Carlo description of photon conversion rejection efficiency and photon identification in the electromagnetic calorimeter is presented in Section 3.6.

The background estimate reported in Table 3.5 and 3.6 depend on the decay modes and branching ratios which are used in the KORALZ Monte Carlo. As previously discussed (*cf.* Section 3.1.1), exclusive branching ratios in any τ generator do not correspond exactly to the world average values, but they are tuned to fit the topological branching ratios. The actual

$\tau \to 3\pi\nu_\tau$	
Backgrounds from other τ decays	f_{bkg} (%)
$\tau \to \rho\nu$	0.27 ± 0.09
$\tau \to 3\pi\pi^0\nu$	9.48 ± 0.48
$\tau \to K^*\nu$	0.33 ± 0.09
multipions, $\tau \to \pi\pi^0\pi^0\nu$, $e^+e^- \to q\bar{q}$	0.16 ± 0.06
Total background	10.24 ± 0.50

Table 3.6: *Summary of background fractions in the $\tau \to 3\pi\nu_\tau$ selection. The background contamination from processes other than those listed in this Table is negligible. The quoted errors come from the Monte Carlo statistics used to determine the backgrounds.*

values used in KORALZ are compared with the Particle Data Group averages in Table 3.7. Notice that significant differences exist between the average measured values and the ones

τ decay mode	Branching ratio (%) KORALZ MC	Branching ratio (%) PDG
$\tau \to e\nu\bar{\nu}$	18.42	17.93 ± 0.26
$\tau \to \mu\nu\bar{\nu}$	17.92	17.58 ± 0.27
$\tau \to \pi\nu$	11.26	11.6 ± 0.4
$\tau \to K\nu$	0.77	0.67 ± 0.23
$\tau \to \rho\nu$	23.00	24.0 ± 0.6
$\tau \to K^*\nu$	1.52	1.43 ± 0.17
$\tau \to 3\pi\nu_\tau$	7.85	8.4 ± 0.4
$\tau \to \pi\pi^0\pi^0\nu$	7.87	10.3 ± 0.9
$\tau \to 3\pi\pi^0\nu$	6.39	5.3 ± 0.4
$\tau \to \pi\pi^0\pi^0\pi^0\nu$	4.85	2.7 ± 0.9
$\tau \to K\pi\pi\nu$	-	0.22 ± 0.16
$\tau \to KK\pi\nu$	-	0.22 ± 0.17
$\tau \to 1-prong$	85.12	85.82 ± 0.25
$\tau \to 3-prong$	14.73	14.06 ± 0.25
$\tau \to 5-prong$	0.15	0.111 ± 0.024

Table 3.7: *The τ branching ratios used in KORALZ Monte Carlo compared to the current world average values.*

used in the Monte Carlo, especially in the hadronic decays ($\tau \to \pi\pi^0\pi^0\nu$, $\tau \to 3\pi\pi^0\nu$, and $\tau \to \pi\pi^0\pi^0\pi^0\nu$). This affects the background estimate of Table 3.5 and 3.6. In particular, the $\tau \to 3\pi\pi^0\nu$ background in the $\tau \to 3\pi\nu_\tau$ sample could be overestimated. On the other hand, the background contamination to the $\tau \to 3\pi n\gamma\nu_\tau$ sample is not expected to vary significantly, since it comes from one-prong τ events and $\tau \to 1-prong$ is reasonably well described by the Monte Carlo.

The three-prong kaon modes ($\tau \to K\pi\pi\nu$ and $\tau \to KK\pi\nu$) are not present in the Monte Carlo and thus they have not been included in Table 3.6. Since no explicit particle identification is performed in order to identify kaons, these modes are included in the $\tau \to 3\pi(n\gamma)\nu_\tau$ branching ratio measurement. The selection efficiency is assumed to be the same as that

of $\tau \to 3\pi\nu_\tau$, since the $K - \pi$ mass difference is not expected to change dramatically the kinematical characteristics of the three tracks.

3.5   Uncorrected $\tau \to 3\pi(n\gamma)\nu_\tau$ branching ratios

Inserting the efficiency and background estimate discussed in the previous Sections into expression 3.1, a value for the $\tau \to 3\pi(n\gamma)\nu_\tau$ branching ratio is obtained. In Table 3.8 the results are summarized. Systematic effects have not yet been included in the measurement. Final results, which include the estimate of the systematic error, will be presented in Section 3.7.

	$\tau \to 3\pi n\gamma\nu_\tau$	$\tau \to 3\pi\nu_\tau$
$N_{\tau \to 3\pi(n\gamma)\nu_\tau}$	1169	570
$\epsilon_{\tau \to 3\pi(n\gamma)\nu_\tau}$ (%)	34.74	26.23
$f_{bkg}^{non-\tau \to 3\pi(n\gamma)\nu_\tau}$ (%)	3.93	10.24
$Br(\tau \to 3\pi(n\gamma)\nu_\tau)$ (%)	13.43 ± 0.40	8.10 ± 0.33

Table 3.8: *Summary of uncorrected $\tau \to 3\pi(n\gamma)\nu_\tau$ branching ratios. The quoted errors are statistical only.*

3.6   Estimate of the systematic error

A study of systematic biases to the $\tau \to 3\pi(n\gamma)\nu_\tau$ branching ratio measurement is performed in this Section. In particular, systematic uncertainties arising from selection efficiency and background estimate are discussed. The branching ratio $Br(\tau \to X\nu_\tau)$ is calculated as (*cf.* expressions 3.1 and 3.2):

$$Br(\tau \to X\nu_\tau) = \frac{N_X(1 - f_{bkg})}{\epsilon_\tau \epsilon_{3-prg}\epsilon_{sel}} \frac{1}{N_\tau^{corr}}.$$

If, for example, a systematic effect changes ϵ_τ by a fraction α (positive or negative):

$$\epsilon_\tau \Longrightarrow \epsilon_\tau(1 + \alpha),$$

the corresponding relative variation in the branching ratio is given by:

$$\frac{\Delta Br}{Br} = \frac{\alpha}{1 + \alpha}. \tag{3.3}$$

The same result is valid also for the other efficiencies.

Consider a variation of a fraction β of the the background B. The corresponding variation of the background fraction is given by:

$$f_{bkg} = \frac{B}{S + B} \Longrightarrow \frac{B(1 + \beta)}{S + B(1 + \beta)} \simeq f_{bkg}(1 + \beta),$$

where S is the signal and the approximation is valid for βB small compared to S. The corresponding relative shift in the branching ratio is:

$$\frac{\Delta Br}{Br} = \frac{\beta f_{bkg}}{1 - f_{bkg}}. \tag{3.4}$$

In the following, expression 3.3 and 3.4 will be used to estimate systematic uncertainties.

3.6.1 Systematic uncertainty from efficiency estimate

Systematic biases can affect the $\tau \rightarrow 3\pi(n\gamma)\nu_\tau$ selection efficiencies $\epsilon_\tau^{\tau \rightarrow 3\pi(n\gamma)\nu_\tau}$, ϵ_{3-prg} and ϵ_{sel}.

• $\epsilon_\tau^{\tau \rightarrow 3\pi(n\gamma)\nu_\tau}$

In Section 3.1.1 the global τ selection efficiency has been corrected for small differences between Monte Carlo and data. The correction factors used to take into account the energy and momentum resolution and the impact parameter distribution apply also in the case of $\epsilon_\tau^{\tau \rightarrow 3\pi(n\gamma)\nu_\tau}$, which thus has to be multiplied by 0.9965 ± 0.0030. Notice that the sample of $\tau \rightarrow 3\pi(n\gamma)\nu_\tau$ candidates used for the branching ratio measurement is a subsample of the selected $\tau^+\tau^-$ events. A systematic bias common to the $\tau^+\tau^-$ selection efficiency and the $\epsilon_\tau^{\tau \rightarrow 3\pi(n\gamma)\nu_\tau}$ will cancel in first approximation, since expression (3.1) is used to calculate the branching ratio. Thus, no systematic error is assigned for this correction.

The TPC cracks must be treated differently. The correction factor to the global τ selection efficiency determined in Section 3.1.1 is essentially due to loss of events with one-prong τ decays in both hemispheres. The effect is expected to be smaller for a three-prong event, since the probability of losing all three tracks in the $\tau \rightarrow 3\pi n\gamma\nu_\tau$ hemisphere is negligible. To illustrate the problem, in Fig. 3.13(a) the ϕ distribution of the tracks, folded in $60°$, is shown for a selected sample of $\tau^+\tau^-$ with only one track in each hemisphere (1-1 topology). The analogous distribution of the three prong momentum for $\tau \rightarrow 3\pi n\gamma\nu_\tau$ candidates is shown in Fig. 3.13(b). The dip visible around $30°$ corresponds to the boundary region between contiguous TPC sectors. The loss of events in the 1-1 topology due to ϕ cracks can be estimated in the following way. The events outside the dead region show a flat distribution in ϕ, and one can assume that this would be the observed behaviour if the cracks were not present. One can then estimate the expected number of events which should be in the plot. From the number of events which are actually in the plot, the loss is obtained. From Fig. 3.13(a) one can estimate a loss of $\delta_{1-1} = 1.6\%$ of the 1-1 events in Monte Carlo and $2.5 \pm 0.3\%$ in data. Events of the 1-1 topology are lost because they migrate to 1-0 and 0-0 topologies. Assuming the probability δ_1 of losing a track in a ϕ crack in a given hemisphere to be independent on the track in the opposite hemisphere, $\delta_1 = \delta_{1-1}/2$. This assumption is not perfectly correct since, given the typical acollinearity of an $e^+e^- \rightarrow \tau^+\tau^-$ event, when a track is pointing to a crack the track in the opposite hemisphere has a bigger probability of being lost in the symmetrical ϕ crack. However, according to Monte Carlo calculations, the losses of 1-1 into 0-0 are much smaller ($\simeq 0.1\%$) than those into 1-0, and the previous estimate of δ_1 is approximately correct. Thus $\delta_1^{MC} = 0.8\%$ and $\delta_1^{data} = 1.25 \pm 0.15\%$. Assuming that events with a 1-3 topology are lost only when the track in the one-prong hemisphere disappears into
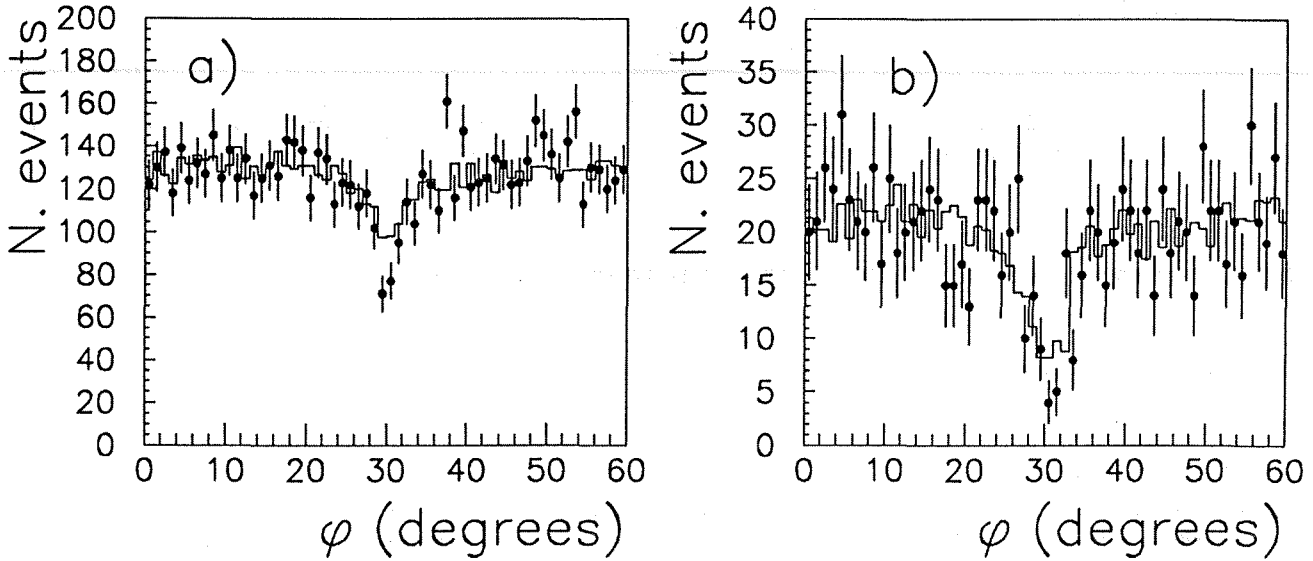
Figure 3.13: *a) The ϕ distribution of the tracks (folded in $60°$) for a selected sample of 1-1 prong topology, b) the ϕ distribution of the three-prong momentum for $\tau \to 3\pi n\gamma\nu_\tau$ candidates. The full line represents the Monte Carlo expectation and the dots represent the data.*

a ϕ crack, the expected relative change of the efficiency $\epsilon_\tau^{\tau \to 3\pi(n\gamma)\nu_\tau}$ can be calculated:

$$\alpha = 1 - \frac{1 - \delta_1^{data}}{1 - \delta_1^{MC}} = 0.45\%.$$

This value gives only an indication of the maximum possible bias, and should not be considered a correction factor to be directly applied to $\epsilon_\tau^{\tau \to 3\pi(n\gamma)\nu_\tau}$, since many events originally in the 1-3 topology will appear as 2-3 or 3-3 topology due to photon conversions, and in this case the relative efficiency change is expected to be smaller. In addition, notice that the ϕ distribution of Fig. 3.13(b) is affected both by $\epsilon_\tau^{\tau \to 3\pi(n\gamma)\nu_\tau}$, corresponding to the track lost in the hemisphere opposite to $\tau \to 3\pi n\gamma\nu_\tau$, and by ϵ_{3-prg}, corresponding to tracks lost in the $\tau \to 3\pi n\gamma\nu_\tau$ hemisphere with a change in the detected topology. A systematic error which includes both $\epsilon_\tau^{\tau \to 3\pi(n\gamma)\nu_\tau}$ and ϵ_{3-prg} will be assigned in the following on the basis of Fig. 3.13(b).

- ϵ_{3-prg}

An imperfect description of ϕ cracks, tracks overlaps and photon conversions in the Monte Carlo can bias the efficiency ϵ_{3-prg} of reconstructing a $\tau \to 3\pi(n\gamma)\nu_\tau$ decay as a three prong event. For sake of simplicity, problems in the pattern recognition of the tracking detectors are included in the class of track overlaps. Cracks and overlaps tend to reduce the number of reconstructed tracks, while photon conversions tend to increase it.

The effect of TPC ϕ cracks has already been shown in Fig. 3.13(b). To study overlaps from close tracks, the minimum angle between the three tracks is plotted in Fig. 3.14. In both cases the agreement between Monte Carlo and data is good and there is no evidence of discrepancy within the statistical error.
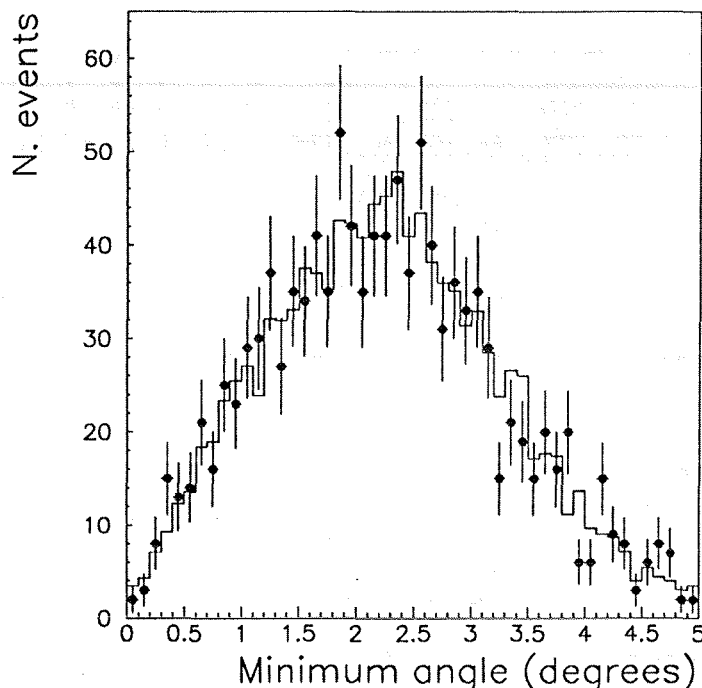
Figure 3.14: *The minimum angle between the three tracks for the $\tau \to 3\pi n\gamma\nu_\tau$ candidates. The full line represents the Monte Carlo expectation and the dots represent the data.*

To further check possible systematics, a visual scan of 600 events in the 1-2 topology (after the photon conversion rejection) has been performed. An illustrative example of a 1-2 topology event caused by a track lost in a TPC ϕ crack is shown in Fig. 3.15. From the scan, $2.5 \pm 0.5\%$ of 1-3 events are reconstructed as 1-2 due to ϕ cracks and $6.8 \pm 0.6\%$ due to overlaps. Both numbers are in good agreement with the Monte Carlo expectations. From Fig. 3.13(b), the fraction of events lost in ϕ cracks is estimated to be $5.0 \pm 0.5\%$, which compares quite well with the Monte Carlo expectation of 4.8%. As previously discussed, this value includes both the loss of events due to the one-prong (opposite to the $\tau \to 3\pi(n\gamma)\nu_\tau$ hemisphere) disappearing in a ϕ crack ($\epsilon_\tau^{\tau \to 3\pi(n\gamma)\nu_\tau}$) and that due to the change of topology of the $\tau \to 3\pi(n\gamma)\nu_\tau$ hemisphere (ϵ_{3-prg}). The variation of the $\tau \to 3\pi(n\gamma)\nu_\tau$ branching ratio caused by a one standard deviation change in the fraction of events lost in ϕ cracks, as measured from the data distribution, is taken as an estimate of the systematic error (*i.e.* $\alpha = 0.5\%/\epsilon_{3-prg}$).

As far as the overlaps are concerned, a small systematic error is expected, given the good agreement between Monte Carlo and data seen in Fig. 3.14 and the result of the visual scanning. A conservative estimate of the systematic error for overlaps is 0.1% of the branching ratios.

Another potential bias to ϵ_{3-prg} comes from the description of photon conversions in the simulation. If the material before the TPC is underestimated(overestimated) in the Monte Carlo, more(less) $\tau \to 3\pi n\gamma\nu_\tau$ ($n > 0$) events would appear as five-prong in the data due to photon conversions. The number of events with five reconstructed prongs in one hemisphere
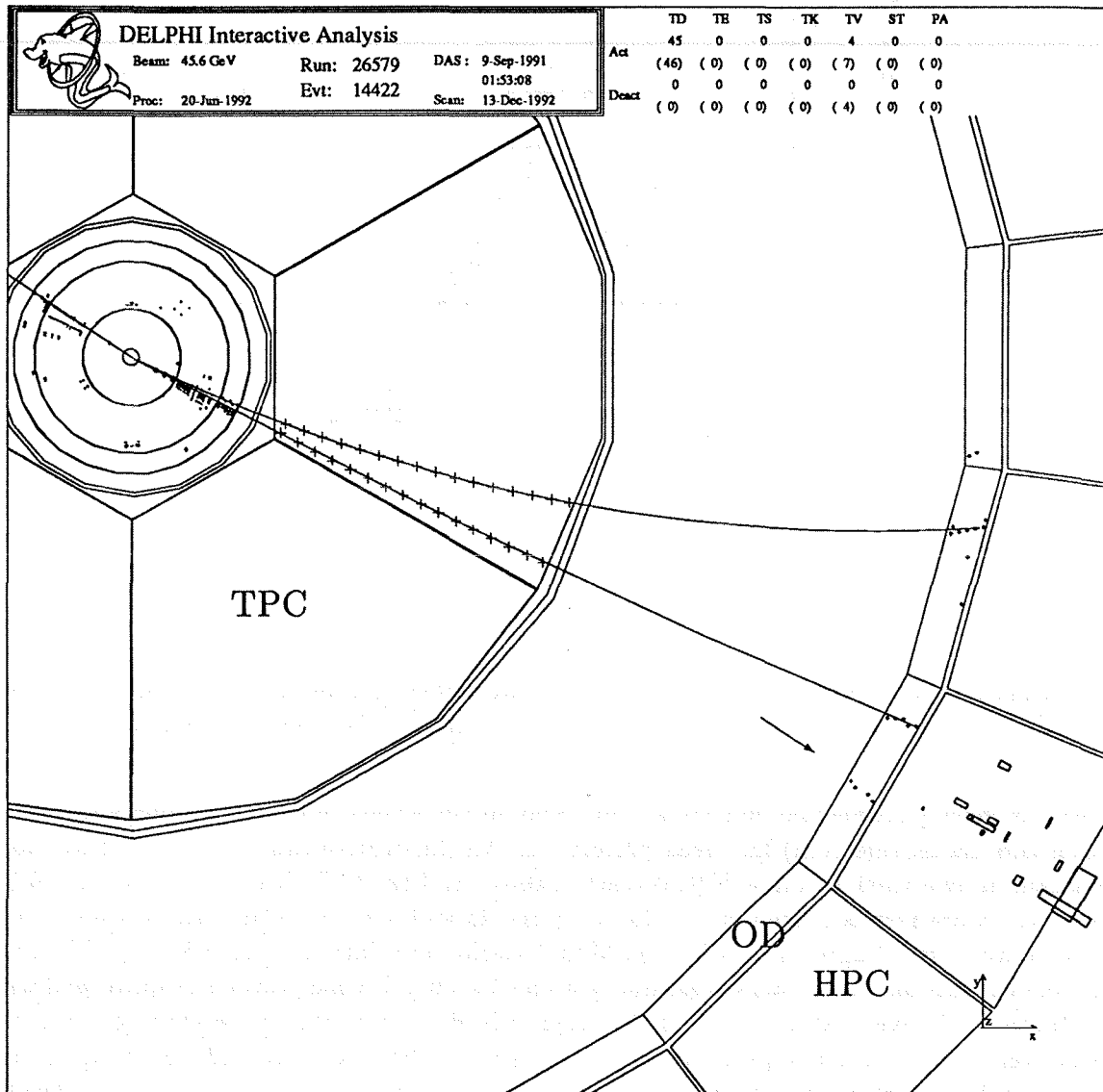
Figure 3.15: *An example of a 1-2 topology event caused by a track lost in a TPC ϕ crack. A track element in the Outer Detector corresponding to the TPC boundary is indicated by an arrow.*

in data is $0.51 \pm 0.06\%$ of all selected τ, to be compared with the Monte Carlo expectation of 0.50%. The number of reconstructed three-prong events (before the $\tau \to 3\pi(n\gamma)\nu_\tau$ selection) in data is 14.67% of the selected τ events. One standard deviation change in the fraction of five-prong events would correspond to a $0.06/14.67 = 0.4\%$ variation in the number of three-prong hemispheres. Thus, a systematic error of 0.4% of the $\tau \to 3\pi n\gamma\nu_\tau$ branching ratio is assigned.
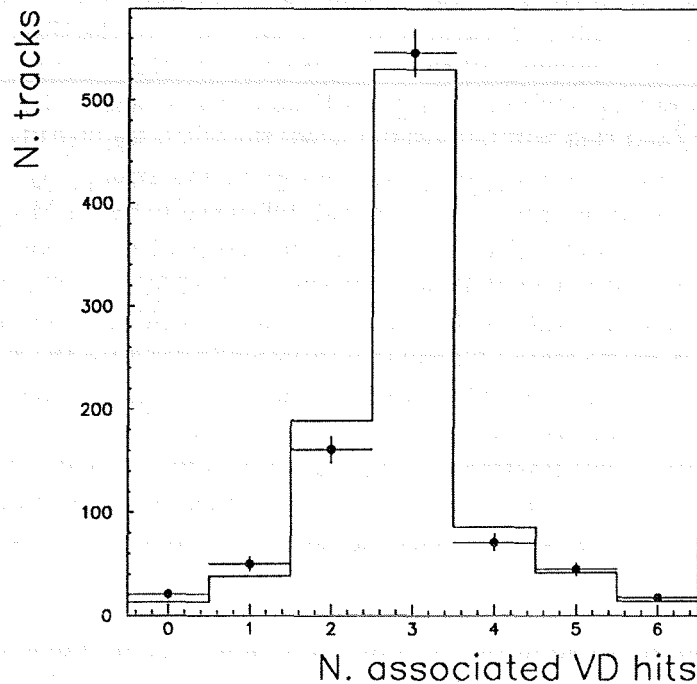
Figure 3.16: *The number of microvertex hits associated to the track in one-prong hemispheres. The full line represents the Monte Carlo expectation and the dots represent the data.*

• ϵ_{sel}

Systematic biases in ϵ_{sel} can be estimated from the agreement between Monte Carlo and data in the distributions of the variables used for the selection. The usual procedure is to vary selection cuts in a reasonable range (related to the resolution of the variable studied), and to take the observed shift in the branching ratio as a measure of the systematic uncertainties. Such shifts, however, may also be caused by statistical fluctuations. In case a large deviation is seen, the systematic effect can be recognized and corrected. But, if the observed shifts are within the expected statistical fluctuations, they can only be considered an upper limit to the size of the systematic uncertainties.

Several distributions relative to the selection cuts are shown in Figs. 3.5-3.11, and the agreement between data and Monte Carlo is good. As a consequence the corresponding systematic errors are well within the statistical error of the measurement. The results are summarized in Table 3.10, where the range of variation used for each cut is reported as well.

A specific study is done for the use of microvertex in the photon conversion rejection procedure. To check microvertex detector efficiency, the number of hits associated to the track in one-prong hemispheres is shown in Fig. 3.16. The inefficiency is very small: only 2.3 ± 0.5% of tracks originating from the main vertex have no hits associated in data, and 1.5% in Monte Carlo. The small difference between data and simulation has no practical effect when estimating the inefficiency for three tracks coming from the interaction point. In fact, assuming that each track behaves independently from the others, the probability of having two tracks

with no hits associated is at the per mil level, and thus is negligible. In this case the inefficiency is due mainly to problems in the pattern recognition which fails to associate external tracks to microvertex hits. The number of tracks with associated hits in the three-prong hemisphere is shown in Fig. 3.6, after applying all the $\tau \to 3\pi n\gamma\nu_\tau$ selection cuts with the exception of the minimum number of tracks with associated VD hits. The fraction of events with less than two tracks associated (and that will be rejected when the cut is applied) is $9.8 \pm 0.8\%$ in data and 8.8% in Monte Carlo. According to the Monte Carlo simulation, only 17% of this fraction is composed of $\tau \to 3\pi n\gamma\nu_\tau$ events. The observed difference between Monte Carlo and data (1.0%) on the fraction of events rejected by the microvertex hits cut can be interpreted as a variation of the selection efficiency of $17\% \times 1.0\%/\epsilon_{sel} = 0.17\%/\epsilon_{sel}$. The corresponding shift in the $\tau \to 3\pi n\gamma\nu_\tau$ branching ratio is $0.17\%/\epsilon_{sel}$ of the branching ratio and this is taken as an estimate of the systematic error. A similar calculation is done for the $\tau \to 3\pi\nu_\tau$ branching ratio. In this case, the fraction of events with less than two tracks associated (and that will be rejected when the cut is applied) is $5.3 \pm 0.9\%$ in data and 3.3% in Monte Carlo. According to Monte Carlo, only 33% of this fraction is composed of $\tau \to 3\pi\nu_\tau$ events. The variation of the selection efficiency is $33\% \times 2\%/\epsilon_{sel} = 0.66\%/\epsilon_{sel}$. The corresponding shift in the $\tau \to 3\pi\nu_\tau$ branching ratio, is $0.66\%/\epsilon_{sel}$ of the branching ratio and this is taken as an estimate of the systematic error.

The systematic errors discussed in this Section are summarized in Table 3.10.

3.6.2   Systematic uncertainty from background contamination

The procedure of varying the selection cuts also changes the background estimate from the Monte Carlo. Therefore, the systematic errors assigned in the previous Section include the possibility of systematic effects in the background estimate. In the following, other possible systematic biases will be considered. Notice that the photon conversion rejection can bias both $\tau \to 3\pi n\gamma\nu_\tau$ and $\tau \to 3\pi\nu_\tau$ branching ratios, while the photon identification can bias only the $\tau \to 3\pi\nu_\tau$ measurement.

• Photon conversions
The observed difference in the number of events rejected by requiring at least two tracks with associated microvertex hits can be interpreted as a change in the background fraction. In the case of $\tau \to 3\pi\nu_\tau$, according to the Monte Carlo simulation, 67% of the events rejected by the VD hits cut are background. Thus, the observed difference between Monte Carlo and data (2.0%) on the fraction of events rejected by the microvertex hits cut corresponds to a background increase, before the cut, of $\Delta_{bkg} = 2.0 \times 0.67/5.3 = 25.3\%$. Notice that one should not conclude that the final background (after the cut) is increased by 25.3%. In fact, the main background in the $\tau \to 3\pi\nu_\tau$ candidates comes from $\tau \to 3\pi\pi^0\nu$, and only 8% of the events rejected by the VD cut are $\tau \to 3\pi\pi^0\nu$ according to the Monte Carlo, while the rest are events with photon conversions. Thus, given the high efficiency for rejecting photon conversions with the VD cut, the expected variation in the background after the cut is applied is much smaller than 25.3%. A quantitative estimate can be obtained as follows. Let f_{bkg-i}^{cut} be the fraction of background events of type i ($i = \tau \to e\nu\bar{\nu}$, $\tau \to \mu\nu\bar{\nu}$, etc.) in the background events rejected
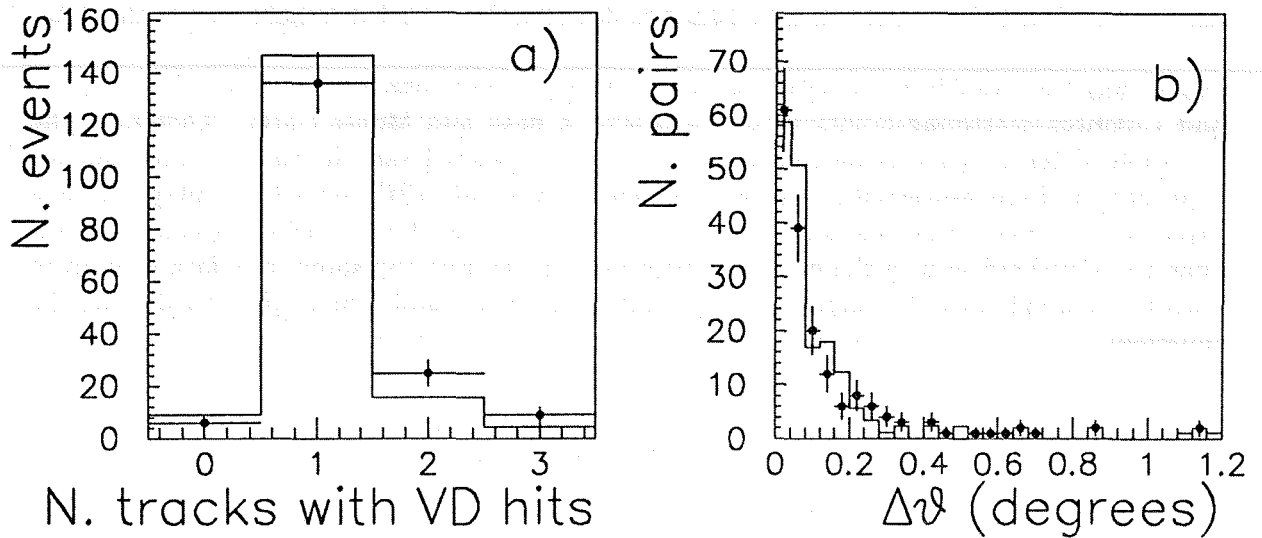
Figure 3.17: *a) The number of tracks in the three-prong hemisphere with associated microvertex hits, b) the $\Delta\theta$ distribution. The plot refers to radiative events $e^+e^- \to e^+e^-\gamma$ with photon conversion. The full line histogram represents the Monte Carlo expectation and the dots represent the data.*

by the cut. The variation of the final background fraction f_{bkg} is given by the expression

$$\beta = \frac{\sum_i f_{bkg-i}(1 + \Delta_{bkg} f_{bkg-i}^{cut}) - f_{bkg}}{f_{bkg}}, \qquad (3.5)$$

where f_{bkg-i} is the final background fraction from background of type i (*cf.* Table 3.5). A variation in the background fraction of 2.4% is calculated from expression (3.5). The corresponding relative shift in the $\tau \to 3\pi\nu_\tau$ branching ratio is 0.3% and this is taken as an estimate of the systematic error. Using a similar procedure for the $\tau \to 3\pi n\gamma\nu_\tau$, a variation of 2.6% in the background fraction is found, which corresponds to a relative shift in the $\tau \to 3\pi n\gamma\nu_\tau$ branching ratio of 0.1%, and is taken as an estimate of the systematic error.

Another check has been performed by selecting a sample of radiative events $e^+e^- \to e^+e^-\gamma$ with photon conversions, requiring three good tracks in one hemisphere, $E_{rad} > 1$ and $P_{vis} > 70$ GeV. The expected background from $\tau^+\tau^-$ events is negligible. In Fig. 3.17(a-b) the number of tracks in the three-prong hemisphere with associated microvertex hits and the $\Delta\theta$ distribution are shown. The photon conversion rejection cuts are applied, and the rejection efficiency determined with the data sample is 94 ± 6% which compares well with the Monte Carlo expectation of 97%.

• Photon definition
A detailed study of photon visibility in the HPC has been performed. The photon identification is based on requirements (*c.f.* Section 3.3) on minimum energy seen in the detector, the minimum number of HPC layers with deposited energy, and the shower starting before

a certain number of radiation lengths. All the variables used in the photon definition are obviously correlated to the minimum energy visible in the detector. The energy threshold used in the simulation should then be tuned to describe the actual threshold seen in the data.

The energy threshold has been studied using a sample of electrons selected from $e^+e^- \to e^+e^-$ and Compton-scattering events $(e^+e^- \to (e)e\gamma)$ in data and Monte Carlo. Therefore, the threshold determination is independent of the $\tau^+\tau^-$ selected sample which is used for the branching ratio measurements. The energy deposited in the HPC layers (one entry per each layer hit) by these electrons is plotted in Fig. 3.18(a): the Monte Carlo threshold is lower than the threshold seen in the data. To determine the correct threshold, the data content in each bin is divided by the corresponding Monte Carlo value and a fit is performed using the function:

$$F(E_{layer}) = P1 - \frac{P2}{1 + exp\left(\frac{E_{layer} - P3}{P4}\right)}, \tag{3.6}$$

where Pi $(i = 1, .., 4)$ are the fitted parameters. The result is plotted in Fig. 3.18(b). The threshold $(P3)$ is found to be 30.3 ± 1.6 MeV. The following procedure is used to modify photons in Monte Carlo events according to the new threshold. The energy in each layer of the photon is weighted using the fitted function as a probability function. Then, the photon definition cuts are applied again. The improvement in the comparison between Monte Carlo and data is clearly seen in Fig. 3.19(a-b), where the energy deposited in the HPC layers is plotted for the candidate photons (i.e. before the photon identification criteria) before and after the tuning of the Monte Carlo threshold.

All the distributions of Fig. 3.9-3.10 have been produced after the adjustment of the threshold, and good agreement between Monte Carlo and data is seen. To check further, distributions other than the ones used to define a good photon have been looked at and good agreement has been found. For example, the number of consecutive HPC layers with energy in a photon shower is plotted in Fig. 3.20(a) and the energy deposited in the first three layers is shown in Fig. 3.20(b).

The improvement in terms of systematic uncertainty can be quantified: without the threshold tuning and applying the same photon identification cuts the $\tau \to 3\pi\nu_\tau$ branching ratio becomes 8.53% ($\simeq 1.3$ standard deviation change), and the variation of the E_γ cut produces a relative shift in the branching ratio of 3.8% to be compared with only a 1.3% shift observed after the threshold tuning.

To estimate a systematic error on the energy threshold, its value has been varied within a range corresponding to the error from the fit and the observed variation on the branching ratio is taken as an estimate of the systematic uncertainty.

Finally, the systematic error associated to the requirement of a minimum energy deposit in the first three HPC layers should be estimated. One possible approach is to vary the minimum energy value used for the cut and take the corresponding maximum observed shift in the branching ratio. However, the minimum energy deposited in the first three layers is highly correlated to the minimum photon energy (particularly for low energy photons), whose associated systematic error has already been taken into account. The observed variation in the
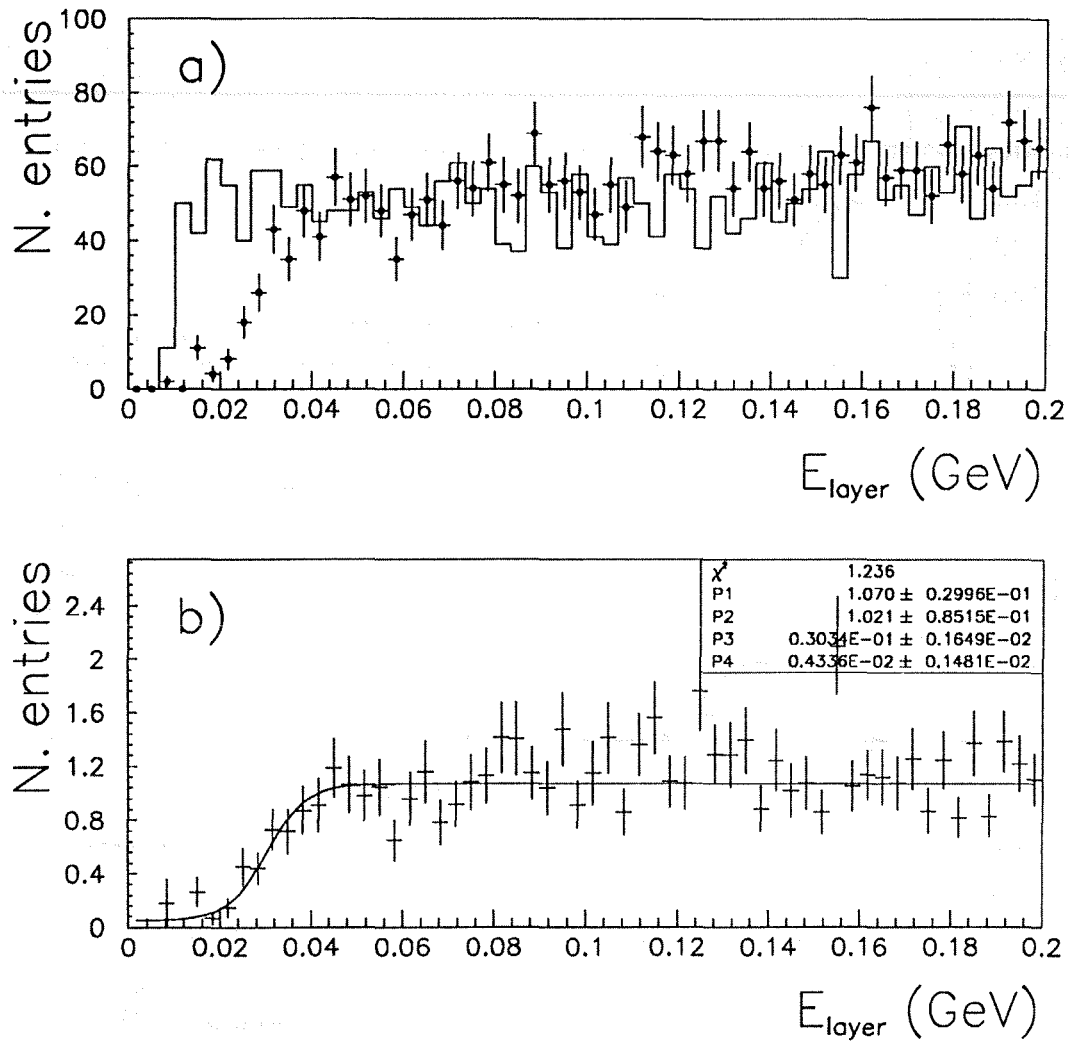
Figure 3.18: *a) The energy deposited in the HPC layers (one entry per each layer hit) by selected electrons. The full line represents the Monte Carlo expectation and the dots represent the data. b) the data content in each bin of a) divided by the corresponding Monte Carlo value. A fit is performed in order to determine the correct threshold(solid line).*

branching ratio when the cut is not applied is taken instead as an estimate of the systematic error.

All the systematic errors from the background estimate are summarized in Table 3.10.

3.6.3   Treatment of Monte Carlo branching ratios

The differences between the branching ratios used in the Monte Carlo and the world average measured values are a possible source of bias. To study the effect on the $\tau \to 3\pi n\gamma\nu_\tau$ branching ratio measurement, the background contribution from each channel estimated from Monte
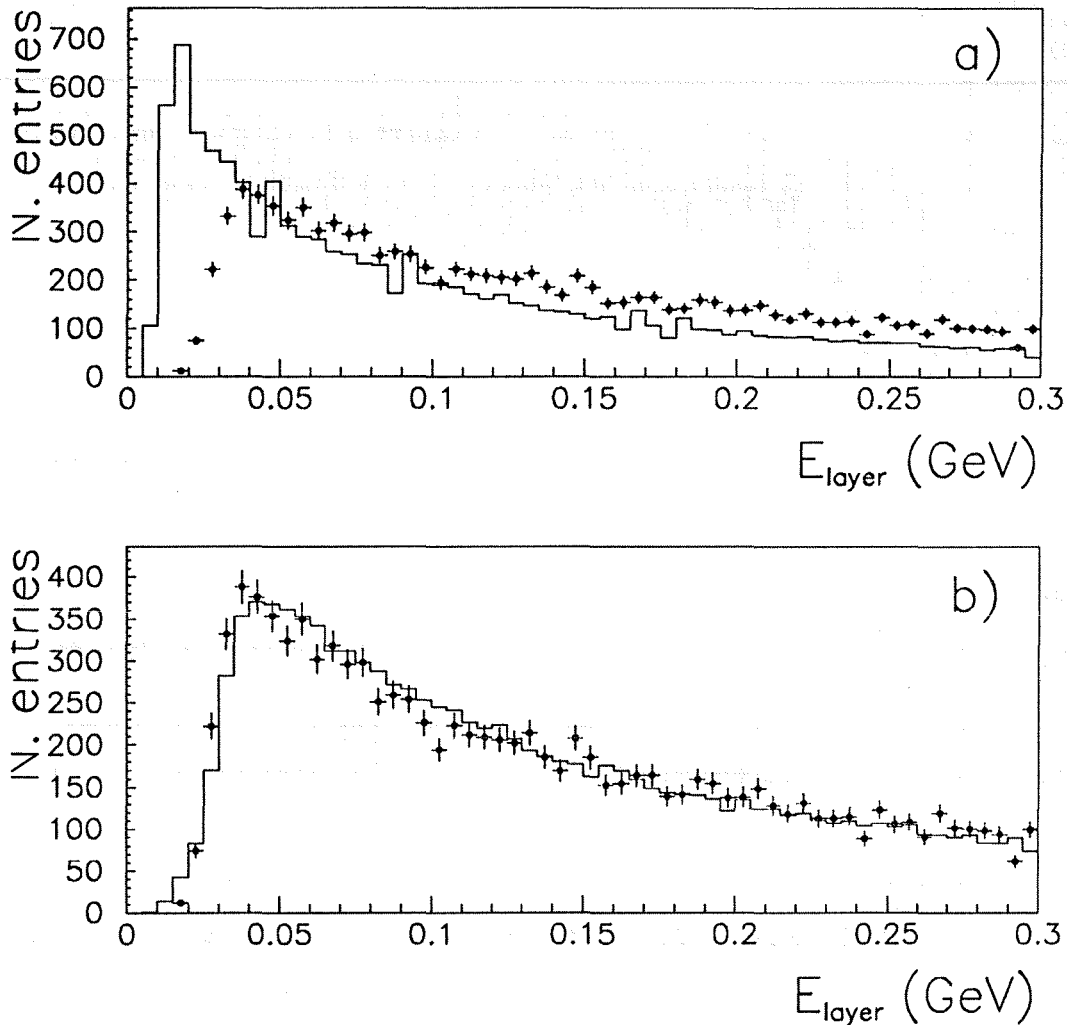
Figure 3.19: *The energy deposited in the HPC layers (one entry per each layer hit) by candidate photons before a) and after b) the tuning of the threshold. The full line represents the Monte Carlo expectation and the dots represent the data.*

Carlo has been rescaled according to the Particle Data Group values. The total background comes out to be the same, which means that the variation of the individual channel contributions to it compensate somewhat. This was expected since the background originates from one-prong τ events and the $\tau \to 1 - prong$ branching ratio is well described by the Monte Carlo. The experimental uncertainties in the PDG averages give a possible variation of the background contamination of 8%, corresponding to a relative variation in the branching ratio of 0.3% which is taken as an estimate of the systematic error.

Also, the estimated efficiencies can be biased. In fact, the $\tau \to 3\pi n\gamma\nu_\tau$ channel in KORALZ is given by $\tau \to 3\pi\nu_\tau$ and $\tau \to 3\pi\pi^0\nu$. Therefore, the efficiency determined with the Monte

Figure 3.20: a) The number of consecutive HPC layers with energy in a photon shower, b) energy deposited in the first three layers. The full line represents the Monte Carlo expectation and the dots represent the data.

Carlo is:

$$
\epsilon_{tot}^{\tau \to 3\pi n\gamma\nu_\tau} = \frac{N_{\tau \to 3\pi\nu_\tau}\epsilon_{3\pi n\gamma}^{\tau \to 3\pi\nu_\tau} + N_{\tau \to 3\pi\pi^0\nu}\epsilon_{3\pi n\gamma}^{\tau \to 3\pi\pi^0\nu}}{N_{\tau \to 3\pi\nu_\tau} + N_{\tau \to 3\pi\pi^0\nu}} =
$$

$$
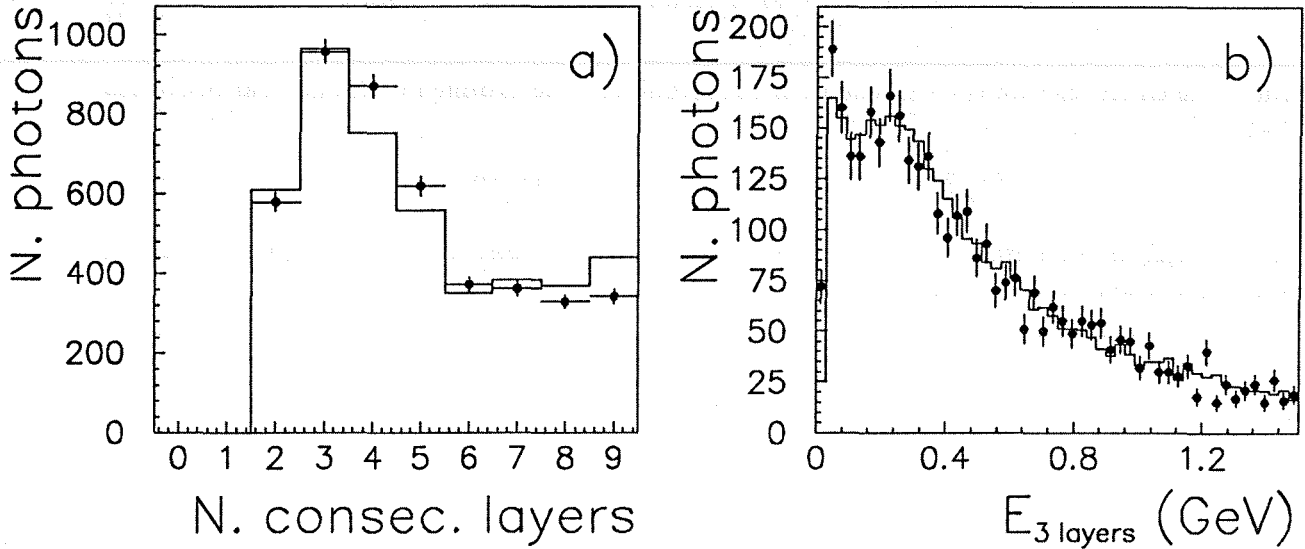= \frac{Br(\tau \to 3\pi\nu_\tau)\epsilon_{3\pi n\gamma}^{\tau \to 3\pi\nu_\tau} + Br(\tau \to 3\pi\pi^0\nu)\epsilon_{3\pi n\gamma}^{\tau \to 3\pi\pi^0\nu}}{Br(\tau \to 3\pi\nu_\tau) + Br(\tau \to 3\pi\pi^0\nu)}, \tag{3.7}
$$

where $\epsilon_{3\pi n\gamma}^{\tau \to 3\pi\nu_\tau}$ and $\epsilon_{3\pi n\gamma}^{\tau \to 3\pi\pi^0\nu}$ are the total efficiencies for $\tau \to 3\pi\nu_\tau$ and $\tau \to 3\pi\pi^0\nu$ corresponding to the $\tau \to 3\pi n\gamma\nu_\tau$ selection. Their values, as determined by Monte Carlo, are 37.77% and 31.01% respectively. Notice that if the efficiencies in expression (3.7) are equal, the branching ratios in the numerator and denominator cancel. If the efficiencies are different, the final result will depend on the branching ratios for $\tau \to 3\pi\nu_\tau$ and $\tau \to 3\pi\pi^0\nu$ which are used in the Monte Carlo.

One way to solve the problem is to use the world average measured values (*cf.* Table 3.7). The efficiency ϵ_{tot} for $\tau \to 3\pi n\gamma\nu_\tau$ would change from 34.74% to 35.15%, thus changing the $\tau \to 3\pi n\gamma\nu_\tau$ branching ratio from 13.43% to 13.27%. Notice that an analogous problem exists when estimating $\tau \to 3\pi\pi^0\nu$ background in the $\tau \to 3\pi\nu_\tau$ sample. In fact, using PDG branching ratio values, the background fraction in the $\tau \to 3\pi\nu_\tau$ sample changes from 10.24% to 8.78% and the branching ratio goes from 8.10% to 8.23%.

Another possibility, which is independent of measurements performed by other experiments, is to correlate the measurement of the $\tau \to 3\pi(n\gamma)\nu_\tau$ branching ratios to the $\tau \to 3\pi\pi^0\nu$ branching ratio, *i.e.* one assumes:

$$
Br(\tau \to 3\pi\pi^0\nu) = Br(\tau \to 3\pi n\gamma\nu_\tau) - Br(\tau \to 3\pi\nu_\tau). \tag{3.8}
$$

Then, expression (3.7) can be written as:

$$\epsilon_{tot}^{\tau \to 3\pi n\gamma\nu_\tau} = \frac{Br(\tau \to 3\pi\nu_\tau)}{Br(\tau \to 3\pi n\gamma\nu_\tau)}\left(\epsilon_{3\pi n\gamma}^{\tau \to 3\pi\nu_\tau} - \epsilon_{3\pi n\gamma}^{\tau \to 3\pi\pi^0\nu}\right) + \epsilon_{3\pi n\gamma}^{\tau \to 3\pi\pi^0\nu} \qquad (3.9)$$

where the efficiencies on the right hand of the formula are determined by Monte Carlo. Notice that

$$\epsilon_{tot}^{\tau \to 3\pi n\gamma\nu_\tau} Br(\tau \to 3\pi n\gamma\nu_\tau) = N_{3\pi n\gamma}^{corr}/N_\tau^{corr}, \qquad (3.10)$$

where $N_{3\pi n\gamma}^{corr}$ is the number of selected $\tau \to 3\pi n\gamma\nu_\tau$ events, corrected for background. Thus, from expression (3.9) one can write:

$$Br(\tau \to 3\pi\nu_\tau)A + Br(\tau \to 3\pi n\gamma\nu_\tau)B = C \qquad (3.11)$$

where

$$A = \epsilon_{3\pi n\gamma}^{\tau \to 3\pi\nu_\tau} - \epsilon_{3\pi n\gamma}^{\tau \to 3\pi\pi^0\nu}, \qquad B = \epsilon_{3\pi n\gamma}^{\tau \to 3\pi\pi^0\nu} \qquad C = N_{3\pi n\gamma}^{corr}/N_\tau^{corr}. \qquad (3.12)$$

On the other hand, the $\tau \to 3\pi\nu_\tau$ branching ratio is given by:

$$Br(\tau \to 3\pi\nu_\tau) = \frac{N_{3\pi}(1 - f_{bkg}^{\tau \to 3\pi\pi^0\nu} - f_{bkg}^{rest})/\epsilon_{tot}^{\tau \to 3\pi\nu_\tau}}{N_\tau^{corr}}, \qquad (3.13)$$

where $f_{bkg}^{\tau \to 3\pi\pi^0\nu}$ is the fraction of background in the $\tau \to 3\pi\nu_\tau$ sample coming from $\tau \to 3\pi\pi^0\nu$ decays, and f_{bkg}^{rest} is the fraction corresponding to the remaining background. The $\tau \to 3\pi\pi^0\nu$ background fraction can be written as:

$$f_{bkg}^{\tau \to 3\pi\pi^0\nu} = \frac{N_{3\pi\pi^0}^{cut}}{N_{3\pi}}, \qquad (3.14)$$

where $N_{3\pi\pi^0}^{cut}$ is the number of $\tau \to 3\pi\pi^0\nu$ events passing the $\tau \to 3\pi\nu_\tau$ selection cuts. Substituting (3.14) into (3.13), an equation similar to (3.11) is obtained:

$$Br(\tau \to 3\pi\nu_\tau)A' + Br(\tau \to 3\pi n\gamma\nu_\tau)B' = C' \qquad (3.15)$$

where

$$A' = \epsilon_{tot}^{\tau \to 3\pi\nu_\tau} - \epsilon_{cut}^{\tau \to 3\pi\pi^0\nu}, \qquad B' = \epsilon_{cut}^{\tau \to 3\pi\pi^0\nu} \qquad C' = N_{3\pi}^{corr}/N_\tau^{corr}. \qquad (3.16)$$

$N_{3\pi}^{corr}$ is the number of selected $\tau \to 3\pi\nu_\tau$ candidates corrected only for the background contamination corresponding to f_{bkg}^{rest}, and $\epsilon_{cut}^{\tau \to 3\pi\pi^0\nu} = N_{3\pi\pi^0}^{cut}/N_\tau^{corr}$.

A, B, C, A', B' and C' can be calculated using the values reported in Tables 3.6, 3.8 and 3.9. Expressions (3.11) and (3.15) can be seen as a system of two equations with two unknown parameters, $Br(\tau \to 3\pi\nu_\tau)$ and $Br(\tau \to 3\pi n\gamma\nu_\tau)$. Solving the system, the following values are obtained for the branching ratios:

$$Br(\tau \to 3\pi n\gamma\nu_\tau) = 13.23\%, \qquad Br(\tau \to 3\pi\nu_\tau) = 8.32\%. \qquad (3.17)$$

Notice that inserting the branching ratios (3.17) in expression (3.8) a value $Br(\tau \to 3\pi\pi^0\nu) = 4.91\%$ is obtained, which is in good agreement with the PDG value of 5.3 ± 0.4. Also, the

$\epsilon_{3\pi n\gamma}^{\tau \to 3\pi\nu_\tau}$	0.3777
$\epsilon_{3\pi n\gamma}^{\tau \to 3\pi\pi^0\nu}$	0.3101
$\epsilon_{cut}^{\tau \to 3\pi\pi^0\nu}$	0.0340

Table 3.9: *Various efficiencies used to calculate the effect of Monte Carlo branching ratio values. See text for explanation.*

values (3.17) are close to those obtained by rescaling the branching ratios in the Monte Carlo with the PDG averages (see discussion above).

To estimate the systematic error, the $\tau \to 3\pi\nu_\tau$ branching ratio obtained with the above procedure is varied by its statistical error (± 0.33). Then, the $\tau \to 3\pi n\gamma\nu_\tau$ branching ratio is recalculated using the solution:

$$Br(\tau \to 3\pi n\gamma\nu_\tau) = \frac{C - ABr(\tau \to 3\pi\nu_\tau)}{B}. \tag{3.18}$$

A relative shift of 0.6% in the $\tau \to 3\pi n\gamma\nu_\tau$ branching ratio is found, and this is taken as an estimate of the systematic uncertainty. A similar procedure is used for the $\tau \to 3\pi\nu_\tau$ branching ratio, and relative systematic error of 0.6% is found.

The experimental uncertainties in the PDG averages give a possible variation of the background contamination in the $\tau \to 3\pi\nu_\tau$ sample of 3% (excluding the $\tau \to 3\pi\pi^0\nu$ contribution which is already taken into account in the procedure described above) corresponding to a relative variation in the branching ratio of 0.4%, which is taken as an estimate of the systematic error.

All the systematic errors discussed in this Section are summarized in Table 3.10.

3.7 The $\tau \to 3\pi(n\gamma)\nu_\tau$ branching ratios

All the systematic uncertainties which have been discussed in Sections 3.6.1-3.6.3 are summarized in Table 3.10. The efficiencies, backgrounds and branching ratios for $\tau \to 3\pi n\gamma\nu_\tau$ and $\tau \to 3\pi\nu_\tau$ are summarized in Table 3.11. The values reported have been corrected for the systematic effects discussed in Section 3.6.

In particular, a correction factor of 0.9965 has been applied to the efficiency (*cf.* systematic bias in $\epsilon_\tau^{\tau \to 3\pi(n\gamma)\nu_\tau}$), and efficiency and background have been corrected for the Monte Carlo branching ratios as discussed in Section 3.6.3.

Some remarks are needed in order to compare the results of this analysis with measurements performed by other experiments:

- the decay $\tau \to K^*\nu_\tau \to K_S\pi\nu_\tau \to \pi\pi\pi\nu_\tau$ is treated as a background, and

- the three-prong kaon modes ($\tau \to K\pi\pi\nu$, $\tau \to KK\pi\nu$) are treated as signal.

	$\Delta Br/Br$ (%)		
Origin	$\tau \to 3\pi n\gamma\nu_\tau$	$\tau \to 3\pi\nu_\tau$	Range
$\epsilon_\tau^{\tau \to 3\pi(n\gamma)\nu_\tau}$ and ϵ_{3-prg} TPC cracks	0.68	0.66	
ϵ_{3-prg} overlaps	0.1	0.1	
γ conversions	0.4	-	
ϵ_{sel} and f_{bkg} $P_{vis}^{3\pi}$	0.36	0.20	9-11 (GeV)
$E_{e.m.}$	0.36	0.38	50-60 (GeV)
$\Delta\theta$	0.36	0.89	0.225-0.375 (degrees)
R_{xy}	0.22	0.25	0.8-1.2 (cm)
$m_{3\pi}$	0.15	0.25	1.8-2.2 (GeV)
HPC thresh.	-	0.38	28-32 (MeV)
E_γ	-	1.27	0.3-0.7 (GeV)
Start layer	-	0.70	no cut
$\theta_{\gamma-3\pi}$	-	0.50	20-40 (degrees)
$E_5^{3\pi}/P_{vis}^{3\pi}$	-	1.52	0.1-0.3
ϵ_{sel} VD association	0.2	1.0	
f_{bkg} VD association	0.12	0.3	
PDG Br errors	0.3	0.4	
MC Br values	0.6	0.6	
TOTAL	1.26	2.82	

Table 3.10: *Summary of relative systematic errors for the $\tau \to 3\pi n\gamma\nu_\tau$ and $\tau \to 3\pi\nu_\tau$ branching ratio measurement. Whenever the error has been estimated varying a selection cut, the corresponding range of variation is reported.*

	$\tau \to 3\pi n\gamma\nu_\tau$	$\tau \to 3\pi\nu_\tau$
$N_{\tau \to 3\pi(n\gamma)\nu_\tau}$	1169	570
$\epsilon_{\tau \to 3\pi(n\gamma)\nu_\tau}$ (%)	35.13	26.14
$f_{bkg}^{non-\tau \to 3\pi(n\gamma)\nu_\tau}$ (%)	3.93	7.81
$Br(\tau \to 3\pi(n\gamma)\nu_\tau)$ (%)	$13.28 \pm 0.39 \pm 0.17$	$8.35 \pm 0.35 \pm 0.24$

Table 3.11: *Summary of corrected $\tau \to 3\pi(n\gamma)\nu_\tau$ branching ratios. The errors quoted for the branching ratios are, in order, statistical and systematic.*

These decay modes are sometimes treated in a different way [33] in the experiments. The effect is not negligible, since the $K_S\pi$ mode has a branching ratio of $\simeq 0.5\%$ and the three-prong kaon modes can account for 0.56% [33].

In Table 3.12, the $\tau \to 3\pi n\gamma\nu_\tau$ branching ratio measured with DELPHI data (this analysis) is compared with results published by other experiments. The PDG [6] value is obtained by summing the exclusive measurements $Br(\tau \to 3\pi\nu_\tau)$ and $Br(\tau \to 3\pi n\gamma\nu_\tau)$ $(n \geq 1)$, adding

the errors of the two measurements in quadrature. The ALEPH [8] value is computed in a similar way. Notice that in the ARGUS [10] measurement, which is an inclusive measurement of $\tau \to 3\pi n\gamma\nu_\tau$ ($n \geq 0$), the three-prong kaon modes have been subtracted. The measured

	$Br(\tau \to 3\pi n\gamma\nu_\tau)$ (%)
PDG	13.7 ± 0.6
ALEPH	14.44 ± 1.00
ARGUS	13.3 ± 0.9
DELPHI	13.28 ± 0.43

Table 3.12: *Recent measurements of the $\tau \to 3\pi n\gamma\nu_\tau$ branching ratio. In the ARGUS measurement, the three-prong kaon modes have been subtracted.*

value of the $\tau \to 3\pi n\gamma\nu_\tau$ branching ratio

$$Br(\tau \to 3\pi n\gamma\nu_\tau) = (13.28 \pm 0.39 \pm 0.17) \ \% \tag{3.19}$$

is in good agreement with the PDG value of 13 7 $\pm$ 0.6 %.

The measured value of the $\tau \to 3\pi\nu_\tau$ branching ratio

$$Br(\tau \to 3\pi\nu_\tau) = (8.{:}5 \pm 0.35 \pm 0.24) \ \% \tag{3.20}$$

is in good agreement with the PDG value of 8.4 ± 0.4 %. In Table 3.13 the $\tau \to 3\pi\nu_\tau$ branching ratio measurements for PDG, ALEP I [8], CELLO [9], ARGUS [53], and DELPHI (this analysis) are reported. In the ARGUS determination, the three-prong kaon modes are subtracted. Thus, the result obtained in t is analysis confirms the higher value for the $\tau \to 3\pi\nu_\tau$ branching ratio of recent measureme ts (the 1990 PDG average was $7.1 \pm 0.6\%$).

Experiment	$Br(\tau \to 3\pi\nu_\tau)$ (%)
PDG	8.4 ± 0.4
ALEPH	9.49 ± 0.72
CELLO	8.7 ± 0.8
ARGUS	6.8 ± 0.5
DELPHI	8.35 ± 0.43

Table 3.13: *Recent measurements of the $\tau \to 3\pi\nu_\tau$ branching ratio. In the ARGUS measurement, the three-prong kaon modes have be n subtracted.*

Chapter 4

Theoretical aspects of the decay $\tau \to 3\pi\nu_\tau$

Several interesting subjects can be investigated with the help of the $\tau \to 3\pi\nu_\tau$ decay. The semileptonic τ decay into three pions allows the study of the axial-vector part of the hadronic current. All the collected experimental data show that the invariant mass of the 3π system from the τ decay is dominated by the a_1 resonance. The a_1 decays through two possible $\rho\pi$ combinations, and measurement of their interference term in the decay amplitude allows a determination of the product γ_{VA} of vector and axial-vector couplings of the charged weak leptonic current (*i.e.* the ν_τ helicity). The weak decay $\tau \to 3\pi\nu_\tau$ is parity violating, and thus it is sensitive to the original τ polarization state.

The related theoretical aspects are outlined in this chapter. The general properties of the 3π system are derived with simple arguments based on symmetry considerations (Bose statistics, isospin, *etc.*). The $\tau \to 3\pi\nu_\tau$ decay then is presented in the framework of the theory of the weak interaction, and the existing models for the hadronic current are reviewed. A detailed description of the $\tau \to 3\pi\nu_\tau$ kinematics is given, and the relevant decay angles and invariant masses are introduced. The explicit decay rate dependence on observables like P_τ, γ_{VA} and the hadronic form factors is derived. Finally, hadronic form factors predicted by various models are compared with each other.

4.1 General properties of the amplitude $X \to 3\pi$

The three pion system produced in the $\tau \to 3\pi\nu_\tau$ decay can be seen as the product of the decay chain

$$\tau \to X\nu_\tau \to 3\pi\nu_\tau$$

where X is a meson of mass m_X. In this Section the general amplitude for the decay

$$X \to \pi_1\pi_2\pi_3 \tag{4.1}$$

is derived taking into account the limitations imposed by isospin (I), spin-parity (J^P) of the 3π final state and Bose statistics. For the sake of simplicity, only allowed quantum numbers for the $\tau \to 3\pi\nu_\tau$ decay will be considered ($I = 1$, $J^P = 0^-, 1^+$; see Section 4.2). A more complete presentation can be found in [34].

The amplitude can be constructed as a product, or a sum of products of the form

$$M_{3\pi} = \sum M_I M_{JP} M_F \qquad (4.2)$$

where M_I carries the isotopic spin dependence, M_{JP} carries the spin J and parity P information, and the remaining energy-momentum dependence is in the form factor M_F. The construction of $M_{3\pi}$ is done in the rest frame of X for the sake of simplicity. The pion momenta $\vec{p}_i$ and their energies w_i satisfy conservation laws:

$$\vec{p}_1 + \vec{p}_2 + \vec{p}_3 = 0 \qquad (4.3)$$
$$w_1 + w_2 + w_3 = m_X. \qquad (4.4)$$

An useful consequence of this is that any function of the energy and momentum variables of the three pions can be expressed as a function of the variables of any two pions. Then symmetry problems involving three identical particles may be reduced to symmetry problems involving only two particles which are trivial.

Notice that, so far, the three pion labels 1, 2 and 3 have no particular meaning, and that the 3π system can be understood as composed of identical bosons. Bose statistics thus constraints the total amplitude $M_{3\pi}$ to be symmetric in the exchange of any two pions.

4.1.1   Isospin constraints

To construct forms of M_I, classified by total isospin, one can use vector operators $\vec{a}$, $\vec{b}$ and $\vec{c}$ to represent the isospins of the first, second and third pions respectively. Notice that a pion is characterized by a unit isospin, of which the third component gives the electric charge of the pion, *e.g.* $a_3 = Q_{\pi_1}$.

The most general way to combine $\vec{a}$, $\vec{b}$ and $\vec{c}$ to make $I = 1$ (M_I transforming like a vector for isospin rotations) is $M_I = \vec{a}(\vec{b} \cdot \vec{c})$ and its obvious permutations. Notice that M_I is now symmetric in two pions. The total amplitude must thus be written as

$$M_{3\pi} = \vec{a}(\vec{b} \cdot \vec{c})A + \vec{b}(\vec{c} \cdot \vec{a})B + \vec{c}(\vec{a} \cdot \vec{b})C, \qquad (4.5)$$

where A, B and C are general functions which contain the spin-parity dependence and the form factors, and are symmetric in the exchange of pions 2-3, 3-1 and 1-2 respectively. $M_{3\pi}$ is then symmetric as required by Bose statistics. The amplitudes which contribute to the charged decay modes can be derived easily. For example, consider the decay $X^- \to \pi^-\pi^-\pi^+$. The amplitude terms proportional to $\vec{a}$ and $\vec{b}$ have the correct charge of the three pion system $I_3 = Q_{3\pi} = -1$. Thus

$$M(\pi^-\pi^-\pi^+) = A + B. \qquad (4.6)$$

Similarly, one can deduce that the only contribution to the decay $X^- \to \pi^0\pi^0\pi^-$ is

$$M(\pi^0\pi^0\pi^-) = C. \tag{4.7}$$

The ratio of the branching ratios of the two different charged modes (apart from an overall factor due to the slightly different total amount of phase space for the two processes) is

$$\frac{Br(\pi^-\pi^-\pi^+)}{Br(\pi^0\pi^0\pi^-)} = \frac{|A + B|^2}{|C|^2}. \tag{4.8}$$

This result will be used in the following to show that the expected ratio for the decays $\tau \to a_1\nu_\tau \to \pi^-\pi^-\pi^+\nu_\tau$ and $\tau \to a_1\nu_\tau \to \pi^0\pi^0\pi^-\nu_\tau$ is unity.

4.1.2   Spin and Parity

It is common to describe states of angular momentum l, with z components m, by spherical harmonics $Y_{l,m}(\theta, \phi)$, where θ and ϕ are defined by the polar coordinates of $\vec{p} = (|p|, \theta, \phi)$. However, in the phenomenological description of states it is more convenient to work with a tensor representation. A complete description of the tensor formalism and properties can be found in the literature [35]. Here only the intuitive aspects are discussed. Using the Cartesian coordinates of the vector $\vec{p}$, one may form tensors of arbitrary rank,

$$T_0 = 1, \quad T_i = p_i, \quad T_{ij} = p_i p_j, \quad T_{ijk} = p_i p_j p_k, \quad \cdots. \tag{4.9}$$

Since

$$p_x \pm i p_y \propto p Y_{1,\pm 1} \qquad p_z \propto p Y_{1,0}, \tag{4.10}$$

the elements of the tensor of rank l can be expressed as linear combinations of $p^l Y_{l',m}(\theta, \phi)$, where $l' \le l$. To make it traceless and symmetric, the tensor is modified by subtraction of appropriate terms. After this reduction, the tensor of rank l provides a $(2l + 1)$-dimensional representation of the rotation group as do the $Y_{l,m}(\theta, \phi)$. The basic tensors become

$$T_0 = 1, \quad T_i = p_i, \quad T_{ij} = p_i p_j - \frac{1}{3}\delta_{ij}p^2, \quad \cdots. \tag{4.11}$$

The vectors from which M_{J^P} is to be constructed (for $J > 0$) are thus the momenta $\vec{p_1}$, $\vec{p_2}$ and $\vec{p_3}$ of the three pions and the pseudovector $\vec{q}$, where

$$\vec{q} = \vec{p_1} \times \vec{p_2} = \vec{p_2} \times \vec{p_3} = \vec{p_3} \times \vec{p_1}. \tag{4.12}$$

Given the intrinsic negative parity of the pion, the 3π system also has an intrinsic negative parity. The parity of three pions states described by M_{J^P} which is a product of $\vec{p_i}$ will thus be $(-1)^J(-1) = (-1)^{J+1}$, which implies spin-parity assignment 0^-, 1^+, 2^-, $\cdots$. When $M_{J^P} \propto \vec{q}$ the parity of the three pion state is $(-1)^{J+1}(-1) = (-1)^{J+2}$ ($\vec{q}$ is a pseudovector), which allows X spin-parity states like 1^-, 2^+, $3^- \cdots$.

For the sake of simplicity, only spin-parity states for X which are allowed in τ decay (*cf.* Section 4.2) will be discussed in the following. A summary of different spin-parity configurations for the 3π system and the corresponding basic tensors are presented in Table 4.1.

J^P	M_{JP}
0^-	1
1^+	$\vec{p_i}$

Table 4.1: *The allowed spin-parity assignment J^P for a X meson produced in a τ decay, and the corresponding basic tensor of the amplitude M_{JP}.*

4.1.3   Form Factors

The form factors are generally functions $M_F(w_1, w_2, w_3)$ of the pion energies. It is convenient to use, instead of w_i, variables s_1, s_2 and s_3 with

$$s_i = (w_j + w_k)^2 - (\vec{p_j} + \vec{p_k})^2, \quad (i \neq j \neq k), \tag{4.13}$$

which is the invariant mass squared for the $j - k$ pion combination. Also let f_3 denote any function of the two variables s_1, s_2 which is symmetric in these variables. The definition of f_1 and f_2 is analogous to f_3. Let h_{12} denote an arbitrary function, $h(s_1, s_2)$, unrestricted by symmetry requirements. Companion functions $h_{21} = h(s_2, s_1)$, h_{13}, *etc.* are constructed by the appropriate permutations.

One can now construct the general function A introduced in Section 4.1.1, which includes the spin-parity dependence and form factors, and is symmetric in the exchange of pions 2-3 (functions B and C are obvious permutations). Also define $\tilde{A}$ as the general antisymmetric function. For example, in the case of spin-parity 0^- the basic tensor is 1; to obtain a general symmetric function A one has simply to take $A = f_1$. The antisymmetric case is easily derived: $\tilde{A} = (s_2 - s_3)f_1$. In the case of 1^+, the basic tensor is $\vec{p_i}$. The most general function, symmetric in the exchange of pion 2 and 3, is $A = h_{32}\vec{p_2} + h_{23}\vec{p_3}$. The antisymmetric function is $\tilde{A} = (s_2 - s_3)(h_{32}\vec{p_2} + h_{23}\vec{p_3})$.

A list of the symmetric and antisymmetric amplitudes for different spin-parity configurations of the three pion system is presented in Table 4.2. So far the finite width, Γ_X, of the X meson

J^P	A	$\tilde{A}$
0^-	f_1	$(s_2 - s_3)f_1$
1^+	$h_{32}\vec{p_2} + h_{23}\vec{p_3}$	$(s_2 - s_3)(h_{32}\vec{p_2} + h_{23}\vec{p_3})$

Table 4.2: *The symmetric amplitude A and antisymmetric $\tilde{A}$ for different spin-parity configurations of the 3π system.*

has been neglected. To take the width effect into account, a relativistic Breit-Wigner factor

$$BW_X(Q^2) = \frac{1}{Q^2 - m_X^2 + im_X\Gamma_X} \quad (w_1 + w_2 + w_3 = Q) \tag{4.14}$$

is included in the final amplitude.

4.1.4 Decays through a ρ intermediate state

Strong interactions among the final state pions may lead to a process of the type

$$X \to \pi_1 + Y, \quad Y \to \pi_2 + \pi_3, \tag{4.15}$$

as a dominant or important mode of the X decay.

One can now study the case in which Y is a ρ meson with spin and isospin of unity. Let $M_{1,23}$ be the amplitude, without the isospin factor, for the decay

$$X \to \pi_1 + \rho \to \pi_1 + \pi_2 + \pi_3. \tag{4.16}$$

To take into account the finite width of the ρ, a Breit-Wigner factor similar to the one in expression (4.14)

$$BW_\rho(s_1) = \frac{1}{s_1 - m_\rho^2 + im_\rho\Gamma_\rho} \tag{4.17}$$

should appear in $M_{1,23}$.

The isospin factor for the ρ has to be constructed with the vectors $\vec{b}$ and $\vec{c}$, and the only combination which gives a vector under rotations in isospin space is $\vec{b} \times \vec{c}$. In order to obtain a unit isospin for the 3π system, one has to include the vector $\vec{a}$. The combination which provides a vector in isospin space is $M_I = \vec{a} \times (\vec{b} \times \vec{c})$, which is antisymmetric in 2 and 3 pions. The complete amplitude M for the process (4.16), apart from an overall $BW_X(Q^2)$ factor, is thus given by

$$M = \vec{a} \times (\vec{b} \times \vec{c})M_{1,23} = [\vec{b}(\vec{c} \cdot \vec{a}) - \vec{c}(\vec{a} \cdot \vec{b})]M_{1,23}, \tag{4.18}$$

and since one wants M to be symmetric, $M_{1,23}$ has to be antisymmetric in the exchange of pions 2 and 3. By symmetrizing expression (4.18), the A, B and C functions introduced in Section 4.1.1 are derived:

$$A = M_{3,12} - M_{2,31}, \tag{4.19}$$

$$B = M_{1,23} - M_{3,12}, \tag{4.20}$$

$$C = M_{2,31} - M_{1,23}. \tag{4.21}$$

Notice that

$$A + B + C = 0 \implies |A + B| = |C|, \tag{4.22}$$

which, when inserted in expression (4.8), gives $Br(\pi^-\pi^-\pi^+)/Br(\pi^0\pi^0\pi^-) = 1$. Based on this isospin argument, one expects the τ charged decay into 3π, dominated by an intermediate ρ resonance, to be equally found in the mode with neutral pions and in the one without.

The explicit form of $M_{1,23}$ is readily obtained once the spin-parity and form factor constraints, determined in Section 4.1.3, are taken into account. The energy-momentum dependence is assumed to be described by the Breit-Wigner $BW_\rho(s_1)$ of expression (4.17) apart from an

arbitrary constant (f_1 and $h_{23} \propto BW_\rho(s_1)$). Using the antisymmetric $\tilde{A}$ function of Table 4.2, one obtains

$$M_{1,23}(0^-) = BW_\rho(s_1)(s_2 - s_3), \tag{4.23}$$

$$M_{1,23}(1^+) = BW_\rho(s_1)[x(s_2 - s_3)\vec{p_1} + y(\vec{p_2} - \vec{p_3})], \tag{4.24}$$

where x, y are arbitrary constants. Notice that $M_{1,23}(1^+)$ is written in a form which explicitely shows the ρ momentum dependence, since $\vec{p_1} = -(\vec{p_2} + \vec{p_3}) = -\vec{p_\rho}$. If $\vec{p_1}$ is substituted in expression (4.24), $M_{1,23}$ becomes a linear combination of $\vec{p_2}$ and $\vec{p_3}$ with an antisymmetric function, as expected from Table 4.2.

One may now write down the total amplitude $M_{3\pi}$ for either $\pi^-\pi^-\pi^+$ or $\pi^0\pi^0\pi^-$ decay

$$M_{3\pi}(J^P) = BW_X(Q^2)[A(J^P) + B(J^P)] = BW_X(Q^2)[-M_{2,31}(J^P) + M_{1,23}(J^P)], \tag{4.25}$$

which gives

$$M_{3\pi}(0^-) = BW_X(Q^2)[BW_\rho(s_1)(s_2 - s_3) + BW_\rho(s_2)(s_1 - s_3)], \tag{4.26}$$

$$\begin{aligned} M_{3\pi}(1^+) = BW_X(Q^2)\{&BW_\rho(s_1)[x(s_2 - s_3)\vec{p_1} + y(\vec{p_2} - \vec{p_3})] \\ + &BW_\rho(s_2)[x(s_1 - s_3)\vec{p_2} + y(\vec{p_1} - \vec{p_3})]\}, \end{aligned} \tag{4.27}$$

4.2 The semileptonic τ decay in the theory of weak interaction

Consider the process

$$\tau(l,s) \rightarrow \nu_\tau(l',s') + H(p_f), \tag{4.28}$$

where $l(l')$ denotes the $\tau(\nu_\tau)$ four-momentum, $s(s')$ is the polarization four-vector of the $\tau(\nu_\tau)$ and p_f is the 4-momentum of the H hadron. The Feynman diagram corresponding to $\tau \rightarrow 3\pi\nu_\tau$ is shown in Fig. 4.1. In the theory of weak interactions [36] the general matrix element S for the semileptonic decay of a polarized τ can be written as a product of leptonic and hadronic currents:

$$S = \frac{G_F}{\sqrt{2}} L_\mu M^\mu = \frac{G_F}{\sqrt{2}} \bar{u}(l',s')\gamma_\mu(g_V^{chr} - g_A^{chr}\gamma_5)\frac{1 + \gamma_5 \rlap{/}{s}}{2} u(l,s) M^\mu, \tag{4.29}$$

where g_V^{chr} and g_A^{chr} are the vector and axial-vector coupling constants in the charged leptonic current ($g_V^{chr} = g_A^{chr} = 1$ in the Standard Model) and s is the polarization 4-vector of the τ lepton, which satisfies:

$$l_\mu s^\mu = 0 \qquad s_\mu s^\mu = -P_\tau^2. \tag{4.30}$$

P_τ is the polarization of the τ.

The differential decay rate is obtained from the square of (4.29):

$$d\Gamma_{\tau \rightarrow H\nu_\tau} = \frac{G_F^2}{2m_\tau}[L_{\mu\nu}H^{\mu\nu}]dPS^{(4)}, \tag{4.31}$$
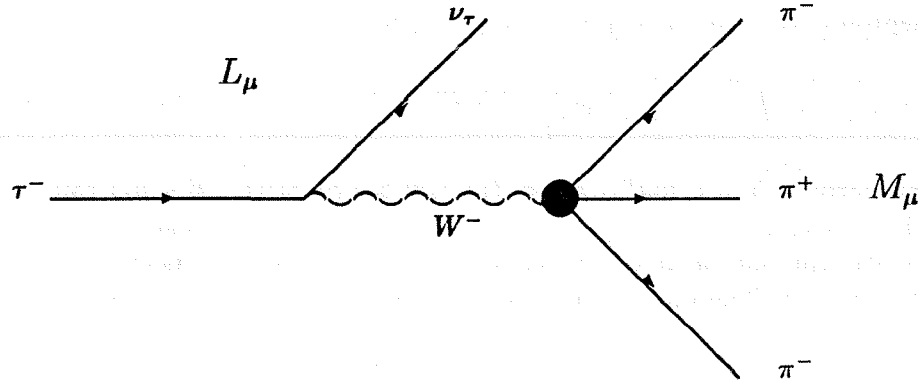
Figure 4.1: *Feynman diagram for the τ semileptonic decay into three pions. L_μ and M_μ are respectively the leptonic and hadronic currents.*

where $dPS^{(4)}$ is the phase space factor of the final state, $L_{\mu\nu} = L_\mu L_\nu^\dagger$ and $H^{\mu\nu} = M^\mu M^{\nu\dagger}$. The lepton tensor is obtained[1] as:

$$L_{\mu\nu} = \frac{1}{2}(\bar{g}_V^2 + \bar{g}_A^2)\{L_{\mu\nu}^{(A)} - \gamma_{VA} L_{\mu\nu}^{(B)}\}, \qquad (4.32)$$

with

$$L_{\mu\nu}^{(A)} = 4\{l, l'\} - 4im_\tau \epsilon_{\alpha\beta\mu\nu} l'^\alpha s^\beta, \qquad (4.33)$$

$$L_{\mu\nu}^{(B)} = -4i\epsilon_{\alpha\beta\mu\nu} l'^\alpha l^\beta + 4m_\tau\{s, l'\}. \qquad (4.34)$$

The chirality parameter is defined as:

$$\gamma_{VA} = \frac{2g_V^{chr} g_A^{chr}}{(g_V^{chr})^2 + (g_A^{chr})^2}, \qquad (4.35)$$

and the ν_τ helicity is given by $h_{\nu_\tau} = -\gamma_{VA}$.

The first comprehensive study of τ decays was done by Tsai [2]. The starting point in the calculation of the semileptonic width is the hadronic Cabibbo current [37]:

$$J_{had}^\mu = [j_V^{(0)\mu} - j_A^{(0)\mu}]\cos\theta_C + [j_V^{(1)\mu} - j_A^{(1)\mu}]\sin\theta_C, \qquad (4.36)$$

where $j_V^{(0)\mu}(j_V^{(1)\mu})$ and $j_A^{(0)\mu}(j_A^{(1)\mu})$ are respectively the strangeness conserving(nonconserving) vector and axial-vector currents, and θ_C is the Cabibbo angle. The hadronic current M_μ introduced in (4.29) is given by

$$M^\mu = <0|J_{had}^\mu|f>, \qquad (4.37)$$

where $|f>$ is the hadronic final state.

---

[1]The following conventions are used [11]: $\{a, b\} \equiv a_\mu b_\nu + a_\nu b_\mu - abg_{\mu\nu}$, the metric tensor $g^{\mu\nu} = g_{\mu\nu} = diag(1; -1, -1, -1)$ and $\epsilon_{0123} = 1$.

The semileptonic width is calculated from (4.31) to be:

$$\Gamma_{\tau \to H\nu_\tau} = \frac{1}{2m_\tau}\frac{G_F^2}{2}\int\frac{d^3l'}{2l_0'}\frac{1}{(2\pi)^3}L_{\mu\nu}\sum_f < 0|J_{had}^\mu|f><f|J_{had}^{\nu\dagger}|0>(2\pi)^4\delta^4(l-l'-p_f). \quad (4.38)$$

The general form of $\sum_f < 0|J_{had}^\mu|f><f|J_{had}^{\nu\dagger}|0>(2\pi)^4\delta^4(l-l'-p_f)$ can be derived considering that, after summing $(\sum_f)$ over all the momenta and polarizations internal to the hadronic state, the only available kinematical quantity which is Lorentz invariant is the 4-vector $Q^\mu = l^\mu - l'^\mu$. The most general second rank tensor which can be written is thus:

$$A(Q^2)g^{\mu\nu} + B(Q^2)Q^\mu Q^\nu, \quad (4.39)$$

and one expects the hadronic tensor to have this form. Thus one can introduce the spectral functions of the hadronic current v_1, a_0 and a_1 (from now on only the strangeness conserving part of the current will be considered) as:

$$\frac{1}{(2\pi)}\sum_f < 0|j_V^{(0)\mu}|f><f|j_V^{(0)\nu\dagger}|0>(2\pi)^4\delta^4(l-l'-p_f) = (Q^\mu Q^\nu - Q^2 g^{\mu\nu})v_1(Q^2),$$

$$\frac{1}{(2\pi)}\sum_f < 0|j_A^{(0)\mu}|f><f|j_A^{(0)\nu\dagger}|0>(2\pi)^4\delta^4(l-l'-p_f) = Q^\mu Q^\nu a_0(Q^2) \quad (4.40)$$

$$+(Q^\mu Q^\nu - Q^2 g^{\mu\nu})a_1(Q^2).$$

Notice that the currents do not interfere with each other because the final states associated to each of them have different quantum numbers, as shown in Table 4.3. Special case of n pions G parity is $(-1)^n$. Also, it can be shown (see [2]) that the spectral functions a_1 and v_1 are

Current	G	J^P	Examples
$j_V^{(0)}$	1	1^-	ρ, 2π, 4π
$j_A^{(0)}$	-1	0^-, 1^+	π, 3π, a_1

Table 4.3: *Possible states and their quantum numbers (G-parity, spin-parity J^P) generated by the vector and axial-vector hadronic current.*

associated to final states with $J = 1$, while a_0 is associated to final states with $J = 0$. The vector spectral function v_0 is assumed to be zero, because of the Conserved Vector Current (CVC) hypothesis [38].

Inserting the spectral functions (4.40) into (4.38) and taking into account $l_0' = (m_\tau^2 - Q^2)/2m_\tau$ in the τ rest frame, the decay width becomes

$$\Gamma_{\tau \to H\nu_\tau} = \frac{G_F^2}{4m_\tau}(\bar{g}_V^2 + \bar{g}_A^2)\cos^2\theta_C\frac{1}{4\pi}\int dQ^2(m_\tau^2 - Q^2)^2\left[\rho_0(Q^2) + \left(1 + \frac{2Q^2}{m_\tau^2}\right)\rho_1(Q^2)\right], \quad (4.41)$$

with

$$\rho_0(Q^2) = a_0(Q^2), \qquad \rho_1(Q^2) = v_1(Q^2) + a_1(Q^2). \quad (4.42)$$

So far the description of the $\tau \to H\nu_\tau$ decay has been completely general. To be able to compare with the measured branching ratios and differential rates, specific models of the spectral functions must be introduced.

Experimental data on the decay $\tau \to \rho\nu$ are very well described [39] by the CVC hypothesis, which relates the vector part of the hadronic current to the isovector part of the total cross section for e^+e^- annihilations into hadrons.

The $\tau \to 3\pi\nu_\tau$ decay is sensitive to the axial part of the hadronic current, and in this case only a partial conservation of the axial current (PCAC [40]) can be invoked. A detailed discussion on the present theoretical understanding of the 3π decay is presented in the next Section.

4.3 Theoretical Models for $\tau \to 3\pi\nu_\tau$

The analysis of experimental data of $\tau \to 3\pi\nu_\tau$ shows a clear dominance of the mode $\tau \to a_1\nu \to \rho\pi\nu_\tau$. The $\rho_0(Q^2)$ term in (4.41) is thus expected to be negligible, since the a_1 has $J^P = 1^+$. The first phenomenological analyses [41] [42] of the Q^2 spectrum used a differential decay rate of the form:

$$\frac{d\Gamma_{\tau \to a_1\nu_\tau}}{dQ^2} \propto \left(\frac{m_{a_1}}{Q}\right)^x (m_\tau^2 - Q^2)^2 \left(1 + \frac{2Q^2}{m_\tau^2}\right) \frac{m_{a_1}\Gamma_{a_1}(Q^2)}{(Q^2 - m_{a_1}^2)^2 + m_{a_1}^2\Gamma_{a_1}(Q^2)}. \tag{4.43}$$

The $(m_{a_1}/Q)^x$ factor was introduced to take into account possible deviations from pointlike coupling at the $W - a_1$ vertex, but so far there is no evidence for such a deviation (i.e. $x \simeq 0$). The $\rho_1(Q^2)$ term is expected to be proportional to a Breit-Wigner factor in order to describe the broad a_1 resonance. Notice that the Γ_{a_1} in (4.43) has a Q^2 dependence, which comes from the $\rho\pi$ phase space, including the effects of the ρ width and of interference of the two possible ρ combinations.

The phenomenological study through (4.43) identifies the main requirements for a theoretical model of the $\tau \to 3\pi\nu_\tau$ decay. These are : a prediction for the $W - a_1$ coupling and the explicit form of the Breit-Wigner term.

Two different theoretical approaches turned out to be quite successful in the description of experimental data; namely the one originating from the assumption of chiral dynamics, with particular attention to the Kühn and Santamaria model [43] as used in the KORALZ Monte Carlo, and the one from Isgur, Morningstar and Reader [44] which uses predictions of the flux-tube-breaking model. In the following, a description of these models is given. The work of Feindt [45], who proposes an ansatz based on angular momentum eigenstates amplitudes, and its relationship with the other models will also be discussed.

4.3.1 Chiral dynamics and the Kühn-Santamaria model

The concept of chiral invariance [46] can be more conveniently introduced in the modern language of the QCD [47] theory of strong interaction. Consider a doublet field for the u and d quarks:

$$q = \begin{pmatrix} u \\ d \end{pmatrix}. \tag{4.44}$$

The part of the QCD Lagrangian which involves u and d quarks can then be written as:

$$L_{u,d} = \bar{q}i\not{D}q + \frac{m_u + m_d}{2}\bar{q}q + \frac{m_u - m_d}{2}(\bar{u}u - \bar{d}d), \qquad (4.45)$$

where $\not{D}$ is the usual covariant derivative and m_u, m_d are the bare quark masses. For $m_u = m_d = m$ this Lagrangian is invariant under isospin transformations $q \to Uq$. Notice that the associated current $V_\mu = \bar{q}\gamma_\mu Tq$ ($T = \sigma/2$ is an isospin matrix) which is equivalent to the hadronic vector current in (4.36), is conserved. In particular, the Lagrangian can be rewritten as

$$L_{u,d} = \bar{q}_L i\not{D}q_L + \bar{q}_R i\not{D}q_R + m(\bar{q}_L q_L + \bar{q}_R q_R), \qquad (4.46)$$

where q has been split into left-handed and right-handed components:

$$q_{L,R} = \left(\frac{1 \mp \gamma_5}{2}\right)q. \qquad (4.47)$$

If one takes $m = 0$, it is easy to verify that the Lagrangian becomes invariant under *independent* 'chiral' isospin transformations on q_L and q_R ($q_L \to U_L q_L$, $q_R \to U_R q_R$). This is the so-called chiral invariance of the strong interaction Lagrangian, which is thus invariant under $SU(2)_L \times SU(2)_R$ transformations. Notice that, under the assumption of chiral symmetry, the axial-vector current $A_\mu = \bar{q}\gamma_\mu\gamma_5 Tq$, which is equivalent to the hadronic axial-vector current in (4.36), is also conserved, since it is by definition the difference between the left-handed and right-handed currents which are conserved.

Processes which involve only interactions between pions do not need the QCD formalism to be described, and the Lagrangian can be written in terms of a pion field π. The request for chiral invariance generates an explicit form [46] [49] for the Lagrangian $L(\pi)$, with only one free parameter f_π: the pion decay constant. The result is that once a process is determined, all the processes with additional pions are predicted, the only free constant being f_π. Notice that, due to the chiral invariance, the pion is massless and the axial-vector current is conserved. In fact, current algebra [48] and chiral dynamics predictions have been very successfully verified in the domain of low energy and few pions. It is an interesting question if these ideas can also be applied in the high energy particle domain.

Fischer, Wess and Wagner [49], starting from the chiral Lagrangian for massless pion interactions, have calculated the multipion interactions of the graphs in Fig. 4.2. The corresponding hadronic current is:

$$J_\mu = f_{a_1}[(p_1 - p_3)^\nu + (p_2 - p_3)^\nu]\left(g_{\mu\nu} - \frac{Q_\mu Q_\nu}{Q^2}\right) \qquad f_{a_1} = -\frac{2\sqrt{2}i}{3f_\pi}, \qquad (4.48)$$

where p_1, p_2 are the like-sign pion momenta, p_3 is the non-like-sign pion momentum and $f_\pi = 93.3$ MeV. This expression for the hadronic current is valid only as long as final state interactions can be neglected. In particular, all invariant masses should be lower than m_ρ^2. This is certainly not the case in the decay $\tau \to a_1\nu_\tau \to \rho\pi\nu_\tau$. The solution proposed by the authors of [49] and by Kühn and Santamaria [43] is to modify the chiral current (4.48) by resonances. The modified current should still be conserved (*i.e* $Q^\mu J_\mu = 0$), and in the low energy limit the result (4.48) should be recovered. Resonances can occur in Q^2 corresponding
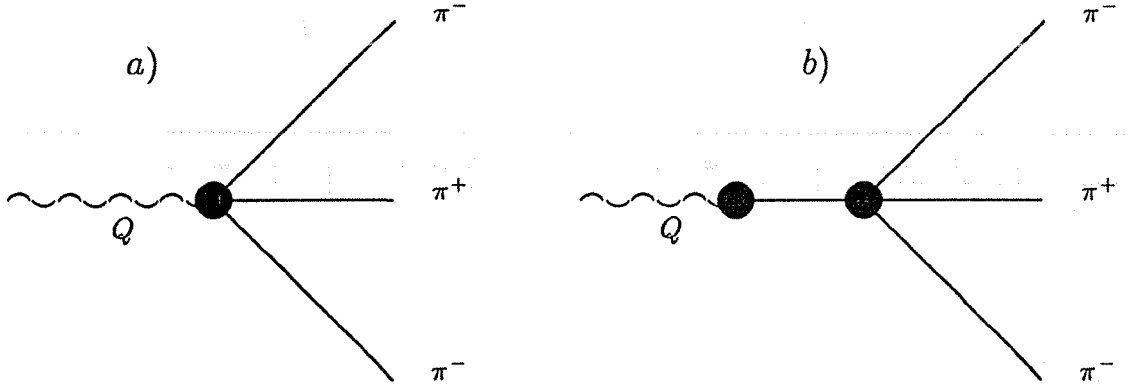
Figure 4.2: *Multipion interactions graphs: a) three pion interaction, b) four pion interaction.*

to the three-body a_1 resonance, or in s_i corresponding to the ρ two-body resonance. The modified hadronic current thus becomes:

$$J_\mu = f_{a_1} BW_{a_1}(Q^2)[BW_\rho(s_2)(p_1 - p_3)^\nu + BW_\rho(s_1)(p_2 - p_3)^\nu]\left(g_{\mu\nu} - \frac{Q_\mu Q_\nu}{Q^2}\right), \qquad (4.49)$$

where the $BW_{a_1,\rho}$ are Breit-Wigner factors corresponding to the a_1 and ρ resonances with the properties $BW_{a_1} \to 1$ $(Q^2 \to 0)$ and $BW_\rho \to 1$ $(s_i \to 0)$. Thanks to these properties, expression (4.48) is recovered in the low energy limit. Notice that this current has the form expected from Bose symmetry as previously derived in Section 4.1.4 (*cf.* expression (4.27) with $x = 0$).

The explicit form of the Breit-Wigner is:

$$BW_X(s) = \frac{m_X^2}{m_X^2 - s - im_X\Gamma_X(s)}, \qquad (4.50)$$

with $X = a_1$, ρ. The energy dependence of Γ_{a_1} is derived from the current (4.49):

$$\Gamma_{a_1}(Q^2) = \Gamma_{a_1}\frac{g(Q^2)}{g(m_{a_1}^2)}, \qquad (4.51)$$

with the three pion phase space factor given by

$$g(Q^2) = \int \frac{ds_1 ds_2}{Q^2} \frac{-J^\mu J_\mu^\dagger}{|f_{a_1}BW_{a_1}(Q^2)|^2}. \qquad (4.52)$$

Notice that $g(Q^2)$ depends on the particular choice of the ρ Breit-Wigner. According to Kühn and Santamaria, the experimental results can be parametrized with a modified Breit-Wigner form to include also the ρ':

$$BW_\rho^{mod} = \frac{BW_\rho + \beta BW_{\rho'}}{1 + \beta}, \qquad (4.53)$$

a)   b)

q $\bar{q}$ q $\bar{q}$
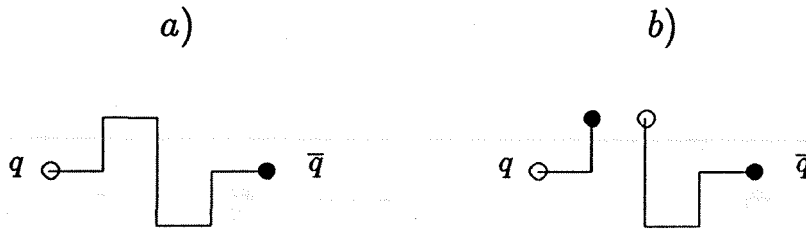
Figure 4.3: *The flux-tube model: a) quark and antiquark sites in the lattice connected by flux links represent a meson state; b) a meson decays through a flux-tube breaking.*

with a best-fit value of $\beta = -0.145$. The energy dependence of Γ_ρ is given by

$$\Gamma_\rho(s) = \Gamma_\rho \frac{m_\rho}{\sqrt{s}} \left(\frac{s - 4m_\pi^2}{m_\rho^2 - 4m_\pi^2} \right)^{\frac{3}{2}}. \tag{4.54}$$

Kühn and Santamaria have successfully fitted the experimental data with their model, and in Table 4.4 the corresponding values of the parameters are reported.

Parameter	Value (GeV)
m_{a_1}	1.251
Γ_{a_1}	0.599
m_ρ	0.773
Γ_ρ	0.145
$m_{\rho'}$	1.370
$\Gamma_{\rho'}$	0.510

Table 4.4: *Fitted parameters of Kühn and Santamaria model.*

4.3.2 The Isgur, Morningstar and Reader model

The flux-tube model [50] is based on the strong-coupling Hamiltonian lattice formulation [51] of QCD. In this picture, the eigenstates of quantum chromodynamics consist of configurations of quarks and flux links (or flux tubes) connected on a lattice. In this limit, mesons correspond to states with a quark and antiquark (at arbitrary points in the lattice) connected by arbitrary configurations of chromoelectric flux along the links between lattice points, as is shown schematically in Fig. 4.3(a). A meson decays with a flux-tube breaking to create a quark antiquark pair, as shown in Fig. 4.3(b). The model is able to reproduce all the known strong decays of mesons [52].

Isgur, Morningstar and Reader [44] have applied the model predictions in the treatment of the $\tau \to a_1\nu_\tau$ process. In order to calculate the hadronic current, they started from the general Feynman graph of Fig. 4.4. The amplitude is then constructed specifying the $W - a_1$ vertex,
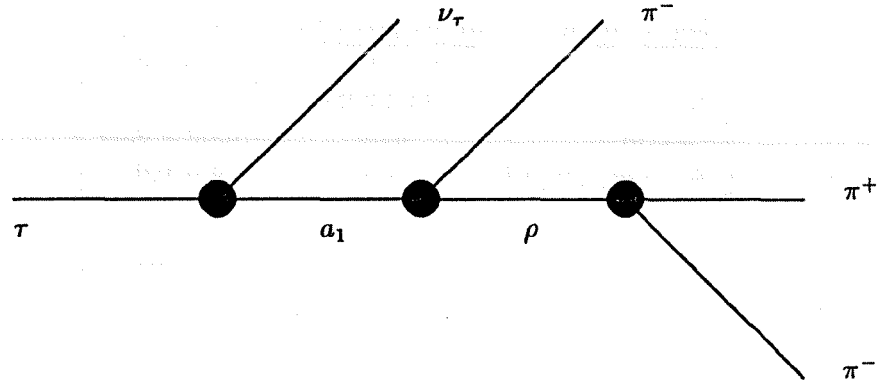
Figure 4.4: *Graph for $\tau \to 3\pi\nu_\tau$ via the a_1 and ρ intermediate states. The blobs represent general vertex functions.*

the $a_1 \to \rho\pi$ vertex, the $\rho \to \pi\pi$ vertex and the particle propagators. The hadronic current in the Isgur et al. model takes the form

$$J_\mu = if_{a_1}BW_{a_1}(Q^2)\left\{ f_{\rho\pi\pi}(s_2)BW_\rho(s_2)\left[f_{a_1\rho\pi}(Q^2,s_2)(p_1 - p_3)^\nu \right.\right.$$

$$\left.\left. + g_{a_1\rho\pi}(Q^2,s_2)\left(p^\nu_{\rho_1} - Q^\nu\frac{p_{\rho_1}Q}{Q^2} \right)\right] + (1 \leftrightarrow 2)\right\}\left(g_{\mu\nu} - \frac{Q_\mu Q_\nu}{Q^2} \right), \qquad (4.55)$$

where $p_{\rho_1} = p_1 + p_3$, f_{a_1} is the weak form factor at the $W - a_1$ vertex, $f_{a_1\rho\pi}$ and $g_{a_1\rho\pi}$ are form factors at the $a_1 \to \rho\pi$ vertex and $f_{\rho\pi\pi}$ is the form factor at the $\rho \to \pi\pi$ vertex. All these form factors are calculated in the framework of the flux-tube breaking model, and their explicit form can be found in [44].

As far as the Breit-Wigner form factors are concerned, definitions (4.50)-(4.54) are used, similarly to Kühn and Santamaria, the only difference being 1 instead of m_X^2 in the numerator of (4.50). No ρ' contribution is considered in the ρ Breit-Wigner (*i.e.* $\beta = 0$ in (4.53)) and the Γ_ρ in (4.54) is multiplied by $f_{\rho\pi\pi}(s)/f_{\rho\pi\pi}(m_\rho^2)$.

The contribution of a scalar part (π') is also considered in the model. The corresponding current is:

$$J_\mu = -\frac{if_{\pi'}}{2}BW_{\pi'}(Q^2)\left[f_{\pi'\rho\pi}(Q^2,s_2)f_{\rho\pi\pi}(s_2)BW_\rho(s_2)(s_3 - s_1) + (1 \leftrightarrow 2)\right]Q_\mu \qquad (4.56)$$

where $f_{\pi'}$ is the weak form factor at the $W - \pi'$ vertex, $f_{\pi'\rho\pi}$ is the form factor at the $\pi' \to \rho\pi$ vertex (see [44]). This scalar current has the form expected from Bose symmetry as previously derived in Section 4.1.4 (*cf.* expression (4.26)).

The predictions for the form factors in the flux-tube breaking model and the result of a fit to data [44] are summarized in Table 4.5. No constraint can be derived on $f_{\pi'}$, and Isgur et al. choose $f_{\pi'} = 0.2f_{a_1}$.

Form factor	Model prediction	Fit to data
f_{a_1}	0.12-0.22	0.25 ± 0.02
$f_{\pi'}$	0.02-0.08	-
$f_{\rho\pi\pi}(m_\rho^2)$	6.08	6.08 ± 0.04
$f_{a_1\rho\pi}(m_{a_1}^2, m_\rho^2)$	4.8	4.6 ± 0.2
$g_{a_1\rho\pi}(m_{a_1}^2, m_\rho^2)$	6.0	5.4 ± 0.5
$f_{\pi'\rho\pi}(m_{\pi'}^2, m_\rho^2)$	5.8	-

Table 4.5: *The strong decay form factors in the flux-tube breaking model.*

Notice that the hadronic current (4.55) contains terms proportional to p_ρ^μ and Q^μ which are not present in the current (4.49) of Kühn and Santamaria. These terms come from a more general form of the $a_1 \to \rho\pi$ vertex used by Isgur et al., and reflect the fact that the general tensor that can be constructed with the available 4-vectors is

$$T_{\mu\nu} = f_{a_1\rho\pi}g_{\mu\nu} + g_{a_1\rho\pi}p_{\rho\mu}Q_\nu. \tag{4.57}$$

In the literature, the Lorentz scalar coefficients $f_{a_1\rho\pi}$ and $g_{a_1\rho\pi}$ have sometimes been identified incorrectly with the S- and D-wave decay amplitudes. In fact, one can decompose the decay amplitude in the a_1 rest frame in terms of S and D waves:

$$f_{a_1\rho\pi}^S Y_{00}(\Omega_\rho) + f_{a_1\rho\pi}^D \sum_{m_L} C(211; m_L, s_\rho, s_{a_1}) Y_{2m_L}(\Omega_\rho), \tag{4.58}$$

where s_ρ and s_{a_1} are the spin projections along the z axis, Y_{Lm_L} and $C(LSJ; m_L, m_S, m_J)$ are the standard spherical harmonics and Clebsch-Gordan coefficients. The two form factors $f_{a_1\rho\pi}$ and $g_{a_1\rho\pi}$ are thus related to the S- and D-wave amplitudes through the expressions

$$f_{a_1\rho\pi}^S(m_{a_1}^2, m_\rho^2) = \frac{\sqrt{4\pi}}{3m_\rho}[(E_\rho + 2m_\rho)f_{a_1\rho\pi}(m_{a_1}^2, m_\rho^2) + (E_\rho^2 - m_\rho^2)g_{a_1\rho\pi}(m_{a_1}^2, m_\rho^2)],$$

$$f_{a_1\rho\pi}^D(m_{a_1}^2, m_\rho^2) = -\frac{\sqrt{8\pi}}{3m_\rho}[(E_\rho - m_\rho)f_{a_1\rho\pi}(m_{a_1}^2, m_\rho^2) + (E_\rho^2 - m_\rho^2)g_{a_1\rho\pi}(m_{a_1}^2, m_\rho^2)]. \tag{4.59}$$

Taking into account that in the a_1 rest frame $E_\rho = m_{a_1}(1 + m_\rho^2/m_{a_1}^2)/2$, and using the flux-tube breaking model predictions of Table 4.5 for the $f_{a_1\rho\pi}$ and $g_{a_1\rho\pi}$ form factors, a prediction of $f^D/f^S \simeq -0.12$ is obtained.

The Isgur, Morningstar and Reader model has been extensively used to fit high statistics samples of $\tau \to 3\pi\nu_\tau$ decay. In particular, ARGUS [53] has recently determined $f^D/f^S = -0.11 \pm 0.02$, which is in very good agreement with the flux-tube breaking model prediction.

4.3.3   The Feindt model

Feindt [45] proposed an ansatz which is based on the orbital angular momentum eigenstates amplitudes for the process $a_1 \to \rho\pi$, $\rho \to \pi\pi$. To construct such amplitudes, one starts from the general tensor (4.57), noticing that $g_{\mu\nu}$ and $p_{\rho\mu}Q_\nu$ separately are not eigenstates of angular momentum. Starting from (4.57) Feindt calculated linear combinations for the

description of $L = 0$ and $L = 2$ transitions, defined by an angular distribution in terms of spherical harmonics

$$C(L11; m_L, s_\rho, s_{a_1})|\vec{p_\rho}|^L Y_{Lm_L}(\Omega_\rho),\tag{4.60}$$

which is equal to the definition (4.58) of Isgur et al., apart from an additional factor $|\vec{p_\rho}|^L$ that takes into account a threshold behaviour. If the $|\vec{p_\rho}|^L$ threshold behaviour is not included, one gets:

$$T_{\mu\nu}^S = g_{\mu\nu} - \frac{1}{Qp_\rho + \sqrt{Q^2 p_\rho^2}} p_{\rho\mu} Q_\nu,$$

$$T_{\mu\nu}^D = g_{\mu\nu} - \frac{Qp_\rho + 2\sqrt{Q^2 p_\rho^2}}{(Qp_\rho)^2 - Q^2 p_\rho^2} p_{\rho\mu} Q_\nu,\tag{4.61}$$

and it is easy to verify, using $f_{a_1\rho\pi} g_{\mu\nu} + g_{a_1\rho\pi} p_{\rho\mu} Q_\nu = f_{a_1\rho\pi}^S T_{\mu\nu}^S + f_{a_1\rho\pi}^D T_{\mu\nu}^D$ and calculating (4.61) in the a_1 rest frame, that the results (4.59) of Isgur et al. are recovered. Including the $|\vec{p_\rho}|^L$ threshold behaviour, the D amplitude becomes:

$$T_{\mu\nu}^D = g_{\mu\nu} \frac{(Qp_\rho)^2 - Q^2 p_\rho^2}{Q^2} - \frac{Qp_\rho + 2\sqrt{Q^2 p_\rho^2}}{Q^2} p_{\rho\mu} Q_\nu.\tag{4.62}$$

The complete decay matrix element for the chain decay reads:

$$J_\mu(a_1 \to \rho\pi \to \pi\pi\pi) = T_{\mu\sigma} \frac{-g^{\sigma\alpha} + p_\rho^\sigma p_\rho^\alpha / p_\rho^2}{m_\rho^2 - p_\rho^2 - im_\rho\Gamma_\rho} (p_1 - p_3)_\alpha,\tag{4.63}$$

where the term $(p_1 - p_3)_\alpha$ is the matrix element for $\rho \to \pi\pi$. One can thus write the S- and D-wave part of the current

$$J_\mu^S = BW_{a_1}(Q^2) \left[BW_\rho(s_2) \left((p_1 - p_3)_\mu - \frac{(p_1 - p_3)Q}{Qp_{\rho 1} + \sqrt{Q^2 p_{\rho 1}^2}} p_{\rho 1\mu} \right) + (1 \leftrightarrow 2) \right],$$

$$J_\mu^D = BW_{a_1}(Q^2) \left[BW_\rho(s_2) \left(\frac{(Qp_{\rho 1})^2 - Q^2 p_{\rho 1}^2}{Q^2} (p_1 - p_3)_\mu \right. \right.$$

$$\left. \left. - \frac{(Qp_{\rho 1} + 2\sqrt{Q^2 p_{\rho 1}^2})((p_1 - p_3)Q)}{Q^2} p_{\rho 1\mu} \right) + (1 \leftrightarrow 2) \right],\tag{4.64}$$

which are then contracted with the spin 1 projection operator $g_{\mu\nu} - Q_\mu Q_\nu / Q^2$. The total current is given by a combination of J_μ^S and J_μ^D, with coefficients which have to be determined from the experimental data.

4.3.4 Comments

The theoretical approaches described in this Section are based on quite different frameworks, and it is interesting to note that the final hadronic currents are quite similar. As a matter

of fact, conservation laws limit in a general way the actual form of the decay amplitude, as discussed in detail in Section 4.1. In particular, the currents (4.49), (4.55) and (4.64) can be reduced to the general expression (4.27) once calculated in the a_1 rest frame where all the time components become zero.

A noticeable difference is the absence of a $p_{\rho\mu}$ term in current (4.49) of Kühn and Santamaria. An identical result would also be obtained by Isgur et al. and Feindt if $g_{a_1\rho\pi}$ in the tensor (4.57) is set to zero. Thus, Kühn and Santamaria current implies a fixed value of the f^D/f^S ratio, which can be calculated from expressions (4.59) taking $g_{a_1\rho\pi} = 0$:

$$\frac{f^D}{f^S} = -\sqrt{2}\frac{E_\rho - m_\rho}{E_\rho + 2m_\rho} \simeq -0.05. \tag{4.65}$$

The ARGUS Collaboration, as previously mentioned, has measured [53] $f^D/f^S = -0.11 \pm 0.02$. However, this result is obtained from a fit to the Isgur et al. model, and it is not excluded that the model of Kühn and Santamaria could fit the Dalitz plot projections for different intervals of Q^2 which are used to determine f^D/f^S.

Concerning the Breit-Wigner factors, a general agreement is found in the literature. Attempts to improve the mass and width expressions (4.50)-(4.52) with the inclusion of the decay into $K^*\bar{K} + \bar{K}^*K$ in the a_1 width, and of an energy dependence of the masses, have been performed by Törnqvist [42] and Isgur et al. [44]. The effect of such modifications, according to [44], is small ($\simeq 15$ MeV shift) and model independent for the a_1 mass, but significant ($\simeq 80$ MeV shift) and model dependant (Törnqvist finds a shift in the opposite direction) for the a_1 width.

In Table 4.6 the results of a fit to the a_1 parameters performed by the ARGUS Collaboration [53] with different models are reported. The differences in the results are not negligible.

Model	m_{a_1} (GeV)	Γ_{a_1} (GeV)
Isgur et al.	1.211 ± 0.007	0.446 ± 0.021
Kühn et al.	1.274 ± 0.007	0.594 ± 0.023
Ivanov et al.	1.246 ± 0.006	0.483 ± 0.021
Bowler	1.236 ± 0.006	0.450 ± 0.022
Törnqvist	1.224	0.592

Table 4.6: *Results for the a_1 parameters from ARGUS using different theoretical models.*

The general comment one can make is that, given the present theoretical understanding of the decay $\tau \to 3\pi\nu_\tau$, whenever the a_1 decay is used to extract observables (like P_τ and γ_{VA}), particular care should be taken in the estimate of possible systematic biases coming from the theoretical uncertainties.

4.4   Kinematics of the decay $\tau \to 3\pi\nu_\tau$

In the process $\tau \to 3\pi\nu_\tau$ the neutrino escapes detection and only the hadronic decay products are observed experimentally. Therefore the τ rest frame cannot be reconstructed. However,
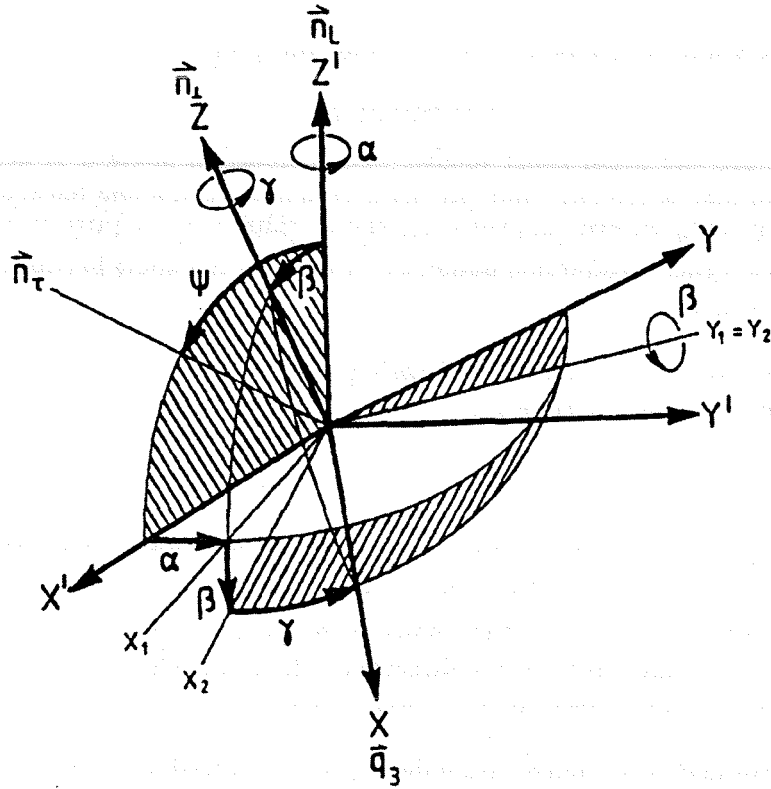
Figure 4.5: *Definition of the Euler angles* α, β, γ *relating the two coordinate frames* S *and* S'.

the kinematical configuration of the decay is still constrained enough to allow at least a partial determination of the kinematical variables. The kinematical properties of $\tau \to 3\pi\nu_\tau$ and their relationship to observables have been studied by several authors [2] [15] [16] [17].

Recently, Kühn and Mirkes [1] [54] have determined the most general angular distribution that can be observed in the semileptonic τ decay, opening the possibility of new experimental investigations. In this Section, their work is summarized and the definition of the experimentally observable kinematical variables is introduced. The conventions of Section 4.2 are followed.

The decay $\tau \to 3\pi\nu_\tau$ is most easily analyzed in the hadronic rest frame $\vec{p}_1 + \vec{p}_2 + \vec{p}_3 = 0$, where $\vec{p}_1$ and $\vec{p}_2$ are the momenta of like-sign pions. Two coordinate frames $S' = Ox'y'z'$ and $S = Oxyz$ are introduced in Fig. 4.5. The system S' allows for a simple description of the τ momentum and spin. The axis Oz' is pointing in the direction of the boost of the pions system in the laboratory $\vec{n}_L$ viewed from the pions in the hadronic rest frame ($\vec{n}_L = -\vec{n}_Q$ where $\vec{n}_Q$ denotes the direction of pions in the laboratory system). The x' axis is chosen such that $\vec{n}_\tau$ (direction of flight of the τ as viewed from the hadronic rest frame) is in the (x', z')-plane, and $(\vec{n}_L \times \vec{n}_\tau)/|\vec{n}_L \times \vec{n}_\tau|$ points along Oy'.

The frame S allows a simple description of the hadron tensor. The (x, y) plane is aligned with the pion momenta, with $\vec{n}_\perp = (\vec{p}_1 \times \vec{p}_2)/|\vec{p}_1 \times \vec{p}_2|$ (the normal to the hadronic plane) pointing along Oz. The Ox axis is defined by the direction of $\hat{p}_3 = \vec{p}_3/|\vec{p}_3|$. Also $|\vec{p}_2| > |\vec{p}_1|$ is always chosen.

The two frames S and S' are related by an Euler rotation

$$\vec{x} = R(\alpha,\beta,\gamma)\vec{x}', \qquad\qquad (4.66)$$

where α, β, γ are the usual Euler angles. The azimuthal angle α is defined by the angle between the two planes $(\vec{n}_L, \vec{n}_r)$ and $(\vec{n}_L, \vec{n}_\perp)$. β denotes the angle between $\vec{n}_\perp$ and $\vec{n}_L$. The remaining Euler angle γ corresponds to a rotation around $\vec{n}_\perp$ and determines the orientation of the pions within their production plane, *i.e.* γ denotes the angle between the $(\vec{n}_L, \vec{n}_\perp)$ plane and the $(\vec{n}_\perp, \vec{p}_3)$ plane.

Since the Euler rotation characterizes the orientation of the hadronic system, the three Euler angles can be used to parametrize the $\pi_1 + \pi_2 + \pi_3 + \nu_\tau$ phase space of expression (4.31):

$$
\begin{aligned}
dPS^{(4)} &= (2\pi)^4 \delta(l - l' - p_1 - p_2 - p_3) \frac{d^3\vec{l}}{2E_\nu} \frac{d^3\vec{p}_1}{2E_1} \frac{d^3\vec{p}_2}{2E_2} \frac{d^3\vec{p}_3}{2E_3} \frac{1}{(2\pi)^{12}} \\
&= \frac{1}{(2\pi)^5} \frac{1}{64} \frac{m_\tau^2 - Q^2}{m_\tau^2} \frac{dQ^2}{Q^2} ds_1 ds_2 \frac{d\alpha}{2\pi} \frac{d\gamma}{2\pi} \frac{d\cos\beta}{2} \frac{d\cos\theta}{2},
\end{aligned}
\qquad (4.67)
$$

where the azimuthal direction of the unobservable neutrino has been integrated over. The angle θ denotes the angle between the direction of flight of τ in the laboratory frame and the direction of the hadrons as seen in the τ rest frame.

In order to disentangle the angular dependence, Kühn and Mirkes write the lepton and hadron tensor contraction in (4.31) as sum of 16 independent terms:

$$
L_{\mu\nu} H^{\mu\nu} = (\bar{g}_V^2 + \bar{g}_A^2)(m_\tau^2 - Q^2) \sum_X \bar{L}_X W_X \qquad X = A, B, ...I, SA, SB, ...SG, \qquad (4.68)
$$

where $\bar{L}_X$ and W_X are appropriate symmetric and antisymmetric combinations of the original lepton and hadron tensor. The hadron factors W_X are given by

$$
\begin{aligned}
W_A &= H^{11} + H^{22} & \qquad W_{SA} &= H^{00} \\
W_B &= H^{33} & \qquad W_{SB} &= H^{01} + H^{10} \\
W_C &= H^{11} - H^{22} & \qquad W_{SC} &= -i(H^{01} - H^{10}) \\
W_D &= H^{12} + H^{21} & \qquad W_{SD} &= H^{02} + H^{20} \\
W_E &= -i(H^{12} - H^{21}) & \qquad W_{SE} &= -i(H^{02} - H^{20}) \\
W_F &= H^{13} + H^{31} & \qquad W_{SF} &= H^{03} + H^{30} \\
W_G &= -i(H^{13} - H^{31}) & \qquad W_{SG} &= -i(H^{03} - H^{30}) \\
W_H &= H^{23} + H^{32} & & \\
W_I &= -i(H^{23} - H^{32}) & &
\end{aligned}
$$

and the lepton factors $\bar{L}_X$ are similar functions of the lepton tensor.

Using expression (4.31), (4.67) and (4.68), the differential decay rate becomes

$$
\begin{aligned}
d\Gamma_{\tau \to \pi\pi\pi\nu_\tau} &= \frac{G_F^2}{4m_\tau} (\bar{g}_V^2 + \bar{g}_A^2) \cos^2\theta_C \sum_X \bar{L}_X W_X \\
&\times \frac{1}{(2\pi)^5} \frac{1}{64} \frac{(m_\tau^2 - Q^2)^2}{m_\tau^2} \frac{dQ^2}{Q^2} ds_1 ds_2 \frac{d\alpha}{2\pi} \frac{d\gamma}{2\pi} \frac{d\cos\beta}{2} \frac{d\cos\theta}{2}.
\end{aligned}
\qquad (4.69)
$$

Notice that all the angular dependence is contained in $\bar{L}_X$, and the hadronic functions W_X depend only on s_1, s_2 and Q^2.

4.4.1 Definition of the observable angles in $\tau \to 3\pi\nu_\tau$

Of the kinematical variables used for the differential rate (4.69), s_1, s_2 and Q^2 are measurable experimentally. The Euler angles β and γ also are observable, since:

$$\cos\beta = \vec{n}_L \cdot \vec{n}_\perp \tag{4.70}$$

$$\cos\gamma = -\frac{\vec{n}_L \cdot \hat{p}_3}{|\vec{n}_L \times \vec{n}_\perp|} \tag{4.71}$$

$$\sin\gamma = \frac{(\vec{n}_L \times \vec{n}_\perp) \cdot \hat{p}_3}{|\vec{n}_L \times \vec{n}_\perp|}. \tag{4.72}$$

Notice that $\vec{n}_L$, $\vec{n}_\perp$ and $\hat{p}_3$ can be determined applying Lorentz transformations and space rotations to the pion 4-vectors measured in the laboratory.

The angle α is defined as

$$\cos\alpha = \frac{(\vec{n}_L \times \vec{n}_r) \cdot (\vec{n}_L \times \vec{n}_\perp)}{|\vec{n}_L \times \vec{n}_r||\vec{n}_L \times \vec{n}_\perp|} \tag{4.73}$$

and cannot be determined because of $\vec{n}_r$.

The cosine of the θ angle is also measurable and is given by

$$\cos\theta = \frac{2xm_\tau^2 - m_\tau^2 - Q^2}{(m_\tau^2 - Q^2)\sqrt{1 - 4m_\tau^2/s}}, \qquad x = \frac{2E_{3\pi}}{\sqrt{s}}, \qquad s = E_{cm}^2, \tag{4.74}$$

where $E_{3\pi}$ is the sum of the pion energies and E_{cm} is the energy in the centre of mass.

Of particular importance for the subsequent discussion is the angle ψ between the direction of the boost of the pions system in the laboratory $\vec{n}_L$ and the τ as seen from the hadronic rest frame (*cf.* Fig. 4.5). The cosine of such angle is

$$\cos\psi = \frac{x(m_\tau^2 + Q^2) - 2Q^2}{(m_\tau^2 - Q^2)\sqrt{x^2 - 4Q^2/s}}. \tag{4.75}$$

In the ultrarelativistic limit $s \gg m_\tau$, and

$$\cos\psi \simeq \frac{\cos\theta(m_\tau^2 + Q^2) + (m_\tau^2 - Q^2)}{\cos\theta(m_\tau^2 - Q^2) + (m_\tau^2 + Q^2)} \tag{4.76}$$

4.4.2 Angular dependence of the $\tau \to 3\pi\nu_\tau$ rate

In order to obtain the differential rate in terms of observable angles, expression (4.69) is integrated over the angle α. The lepton functions $\bar{L}_X$ become thus functions only of θ, β, γ, ψ and Q^2, and can be written explicitly [54]:

$$\bar{L}_A = \frac{2}{3}K_1 + K_2 + \frac{1}{3}\bar{K}_1\frac{3\cos^2\beta - 1}{2}$$

$$\bar{L}_B = \frac{2}{3}K_1 + K_2 - \frac{2}{3}\bar{K}_1 \frac{3\cos^2\beta - 1}{2}$$

$$\bar{L}_C = -\frac{1}{2}\bar{K}_1 \sin^2\beta \cos 2\gamma$$

$$\bar{L}_D = \frac{1}{2}\bar{K}_1 \sin^2\beta \sin 2\gamma$$

$$\bar{L}_E = \bar{K}_3 \cos\beta$$

$$\bar{L}_F = \frac{1}{2}\bar{K}_1 \sin 2\beta \cos\gamma \qquad\qquad (4.77)$$

$$\bar{L}_G = -\bar{K}_3 \sin\beta \sin\gamma$$

$$\bar{L}_H = -\frac{1}{2}\bar{K}_1 \sin 2\beta \sin\gamma$$

$$\bar{L}_I = -\bar{K}_3 \sin\beta \cos\gamma$$

$$\bar{L}_{SA} = K_2$$

$$\bar{L}_{SB} = \bar{K}_2 \sin\beta \cos\gamma$$

$$\bar{L}_{SD} = -\bar{K}_2 \sin\beta \sin\gamma$$

$$\bar{L}_{SF} = -\bar{K}_2 \cos\beta$$

$$\bar{L}_{SC} = \bar{L}_{SE} = \bar{L}_{SG} = 0$$

with

$$K_1 = 1 - \gamma_{VA}P_\tau \cos\theta - \frac{m_\tau^2}{Q^2}(1 + \gamma_{VA}P_\tau \cos\theta)$$

$$K_2 = \frac{m_\tau^2}{Q^2}(1 + \gamma_{VA}P_\tau \cos\theta)$$

$$K_3 = \gamma_{VA} - P_\tau \cos\theta$$

$$\bar{K}_1 = K_1 \frac{3\cos^2\psi - 1}{2} - \frac{3}{2}K_4 \sin 2\psi$$

$$\bar{K}_2 = K_2 \cos\psi + K_4 \sin\psi \qquad\qquad (4.78)$$

$$\bar{K}_3 = K_3 \cos\psi - K_5 \sin\psi$$

$$K_4 = \sqrt{\frac{m_\tau^2}{Q^2}}\gamma_{VA}P_\tau \sin\theta$$

$$K_5 = \sqrt{\frac{m_\tau^2}{Q^2}}P_\tau \sin\theta.$$

The explicit expressions (4.77)-(4.78) of the leptonic factors show that the τ polarization P_τ and the chirality parameter γ_{VA} can be extracted from the angular distributions.

4.5   Hadronic structure functions and model dependence

The hadronic structure functions W_X contain the dynamics of the hadronic decay and depend in general on s_1, s_2 and Q^2. They can be calculated using expressions (4.69) once the hadronic current is specified.

The general ansatz to describe the decay into three pions can be written:

$$J_\mu = J^{(1)\nu}\left(g_{\mu\nu} - \frac{Q_\mu Q_\nu}{Q^2}\right) + J^{(0)}_\mu, \qquad (4.79)$$

where the current $J^{(1)}_\mu$ corresponds to spin 1 (a_1) and $J^{(0)}_\mu \propto Q_\mu$ corresponds to spin 0 (π'). One can check that the currents of the models discussed in Section 4.3 can be written in the form (4.79).

Some constraints on the hadronic structure functions are derived from the general form of the current (4.79). The spin 1 part of the current has no timelike component in the hadronic rest frame introduced in Section 4.4. This is explained by the fact that the contraction of the spin 1 projection operator $g_{\mu\nu} - Q_\mu Q_\nu/Q^2$ with any 4-vector $p^\mu = (p^0, \vec{p})$ produces a new 4-vector $(0, \vec{p})$ with a zero time component. The spatial components of $J^{(1)}_\nu$ are confined to the (x, y) plane. In fact, the current is composed by $(p_1 - p_3)_\nu$ and $(p_1 + p_3)_\nu$ terms, and by construction of the S frame ($Oz \equiv \vec{n}_\perp$, $Ox \equiv \hat{p}_3$) the spatial components of the pion momenta are confined to the (x, y) plane. The spin 0 part of the current ($\propto Q_\mu$) has instead only a timelike component. Hence, only the structure functions constructed from tensors with x, y and time components are different from zero, *i.e.* W_A, W_C, W_D and W_E which arise from spin 1, and W_{SA}, W_{SB}, W_{SC}, W_{SD} and W_{SE} which arise from spin 0.

W_A and W_{SA} are closely related to the spin 1 and spin 0 part of the spectral functions introduced in (4.41), *i.e.*

$$\rho_1(Q^2) = \frac{1}{6}\frac{1}{(4\pi)^4}\frac{1}{Q^4}\int ds_1 ds_2 W_A \qquad (4.80)$$

$$\rho_0(Q^2) = \frac{1}{2}\frac{1}{(4\pi)^4}\frac{1}{Q^4}\int ds_1 ds_2 W_{SA}. \qquad (4.81)$$

A possible strategy to isolate the various structure functions proposed by Kühn and Mirkes is to take suitable moments of the decay rate, with a moment of a variable m defined as

$$< m > = \frac{3}{(\bar{g}_V^2 + \bar{g}_A^2)(m_\tau^2 - Q^2)}\int L_{\mu\nu}H^{\mu\nu}m\frac{d\cos\beta}{2}\frac{d\gamma}{2\pi}. \qquad (4.82)$$

An appropriate set of moments is [54]:

$$< 1 > = (2K_1 + 3K_2)W_A + 3K_2 W_{SA} \qquad (4.83)$$

$$< (3\cos^2\beta - 1)/2 > = \frac{1}{5}\bar{K}_1 W_A \qquad (4.84)$$

$$< \cos 2\gamma > = -\frac{1}{2}\bar{K}_1 W_C \qquad (4.85)$$

$$< \sin 2\gamma\, sign(s_1 - s_2) > = \frac{1}{2}\bar{K}_1 sign(s_1 - s_2)W_D \qquad (4.86)$$

$$< \cos\beta\, sign(s_1 - s_2) > = \bar{K}_3 sign(s_1 - s_2)W_E \qquad (4.87)$$

$$< \sin\beta\cos\gamma > = \bar{K}_2 W_{SB} \qquad (4.88)$$

$$< \sin\beta\sin\gamma\, sign(s_1 - s_2) > = -\bar{K}_2 sign(s_1 - s_2)W_{SD}, \qquad (4.89)$$

where $sign(s_1 - s_2) = +1(-1)$ when $s_1 > s_2 (s_1 < s_2)$. Notice that the moments (4.83)-(4.89) are functions of $\cos\theta$, s_1, s_2 and Q^2, and are measurable.

4.6   Comparison of hadronic structure functions for different models

The structure functions W_X depend on the specific choice of the model used for the hadronic current. The moments (4.83)-(4.89) could be used to extract the structure functions, and their comparison with the predictions could distinguish different models. On the other hand, if one wants to use the angular distributions of the lepton functions $\bar{L}_X$ to measure P_τ (or γ_{VA}), particular care should be taken in understanding the uncertainties coming from the imperfect knowledge of the hadronic current, since the differential rate is proportional to $\sum_X \bar{L}_X W_X$. In the following, numerical predictions and comparisons of different models are presented. The main purpose of this study is to determine if significant differences exist in the model predictions. If this is the case, a specific analysis of the systematic error introduced in the P_τ measurement would be needed.

One can introduce the $s_1 s_2$-integrated hadronic structure functions as:

$$w_{A,C,SA,SB} = \int ds_1 ds_2 W_{A,C,SA,SB} \qquad (4.90)$$

$$w_{D,E,SD} = \int ds_1 ds_2 sign(s_1 - s_2) W_{D,E,SD}. \qquad (4.91)$$

These structure functions are now only Q^2 dependent, and can be visualized. The w_E structure function is closely related to the parity violating asymmetry proposed in [15] [43] [45] which has been used by ARGUS [53] to measure γ_{VA} (see [54] for detailed discussion).

Kühn and Mirkes [54] presented numerical predictions for the w_X using the Kühn and Santamaria model for the spin 1 part of the hadronic current. The corresponding structure functions normalized to w_A are shown in Fig. 4.6.

For the scalar part of the current, they assumed:

$$J_\mu^{(0)} = -\frac{ig_{\pi'\rho\pi}g_{\rho\pi\pi}f_{\pi'}}{2m_\rho^4 m_{\pi'}^2} BW_{\pi'}(Q^2)[s_1(s_2 - s_3)BW_\rho(s_1) + s_2(s_1 - s_3)BW_\rho(s_2)]Q_\mu, \qquad (4.92)$$

with $g_{\pi'\rho\pi} = 5.8$, $g_{\rho\pi\pi} = 6.08$, $f_{\pi'} = 0.08$, $m_{\pi'} = 1.3$ GeV and $\Gamma_{\pi'} = 0.3$ GeV. The energy dependence of $\Gamma_{\pi'}(Q^2)$ is given by:

$$\Gamma_{\pi'}(Q^2) = \Gamma_{\pi'} \left(\frac{\sqrt{Q^2}}{m_{\pi'}} \right)^5 \left(\frac{1 - m_\rho^2/Q^2}{1 - m_\rho^2/m_{\pi'}^2} \right)^3. \qquad (4.93)$$

This parametrization corresponds to a scalar contribution on the total rate $\Gamma_{3\pi}$ of $\simeq 5\%$. The predictions for the structure functions arising from the presence of such scalar component are shown in Fig. 4.7. One observes that the scalar contributions are not negligible ($\simeq 10 - 15\%$), and thus could be observable experimentally. Notice that no direct experimental measurement of the hadronic form factors has been performed so far.

Some relevant aspects of the hadronic form factors have been investigated:

• **Dependence on a_1 mass parameters**
A change of the a_1 mass and width is not expected to modify Fig. 4.6, since $w_X \propto BW_{a_1}$.

Figure 4.6: *The spin 1 hadronic structure functions, normalized to w_A, as functions of Q^2: Kühn-Mirkes (solid lines), Isgur et al. (dashed lines), Feindt (dotted lines; $f^D/f^S = -0.11$).*

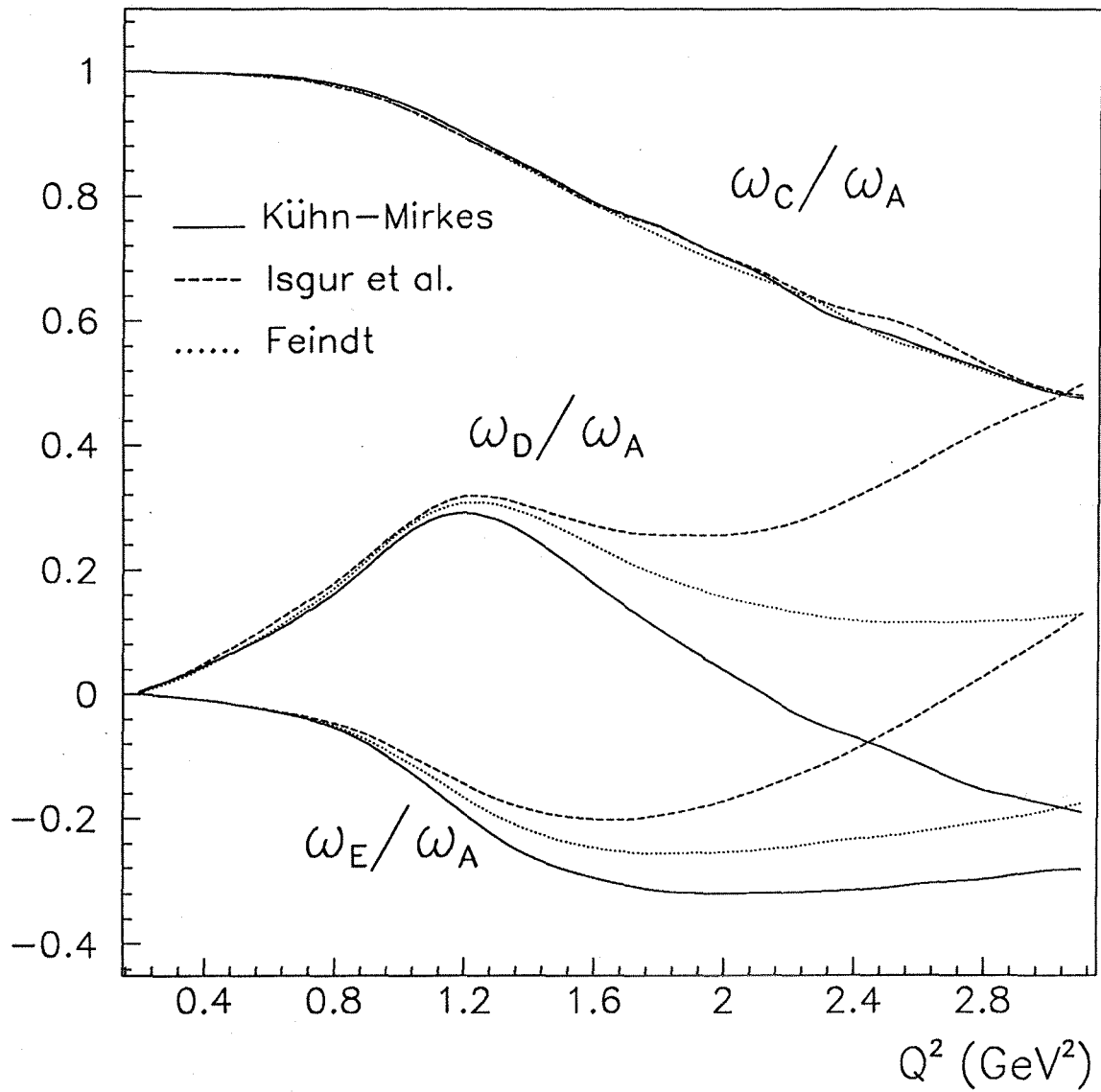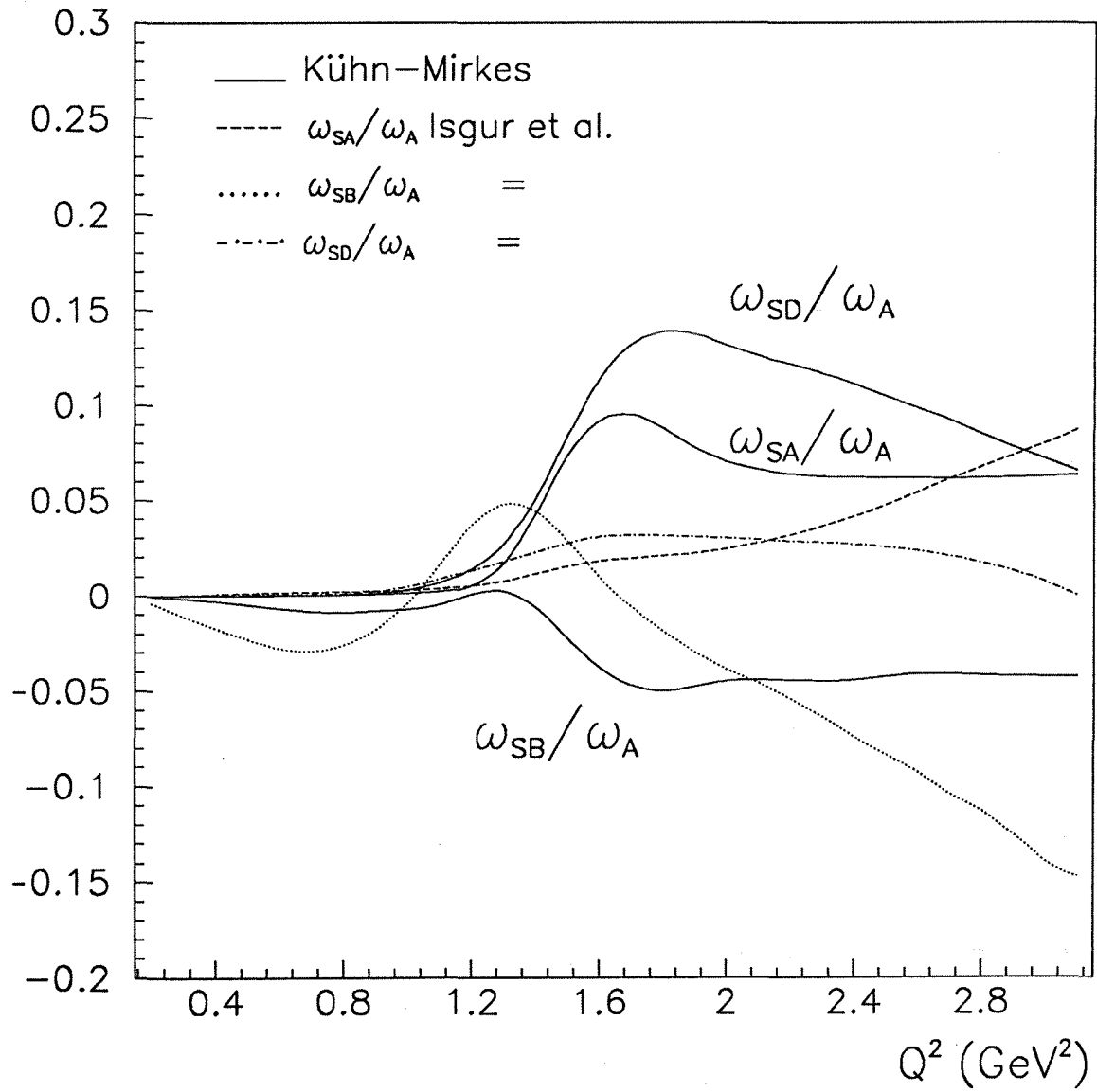**Figure 4.7:** *The spin 0 hadronic structure functions, normalized to w_A, as functions of Q^2: Kühn-Mirkes (solid lines), Isgur et al. (dashed, dashed-dotted and dotted lines).*
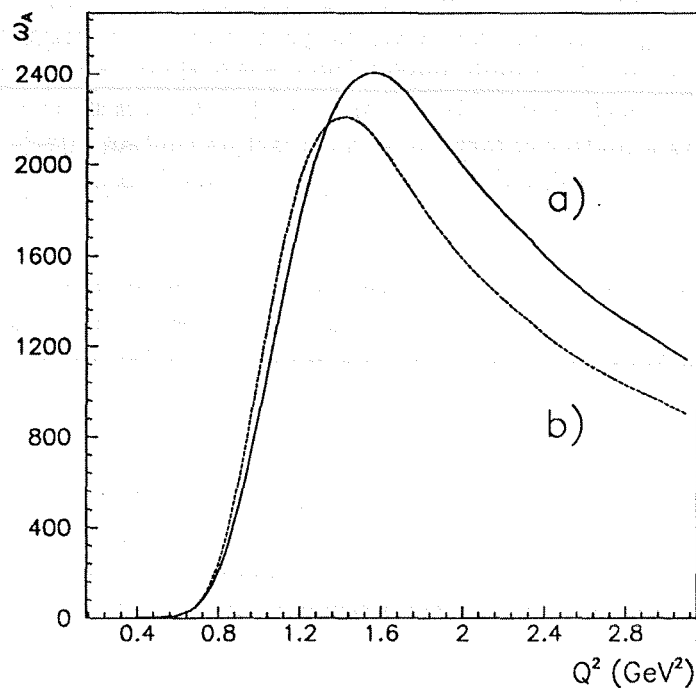
Figure 4.8: *The hadronic structure function w_A as a function of Q^2: a) $m_{a_1} = 1.251$ GeV, $\Gamma_{a_1} = 0.599$ GeV; b) $m_{a_1} = 1.200$ GeV, $\Gamma_{a_1} = 0.549$ GeV.*

The a_1 Breit-Wigner contribution will thus cancel in the ratio w_X/w_A. However, the Q^2 dependence of the form factors is affected, as it is clearly visible for w_A in Fig. 4.8, where the Kühn and Santamaria model has been used. In particular, the model prediction for the total decay rate can change significantly. In Table 4.7 the Kühn and Santamaria model predictions for the $\tau \to a_1 \nu$ decay rate normalized to the leptonic decay rate ($\Gamma_{\tau \to a_1 \nu}/\Gamma_{\tau \to e \nu \bar{\nu}}$) are reported for various values of the a_1 mass and width. Notice that the maximum difference in the

m_{a_1}	Γ_{a_1}	$\Gamma_{\tau \to a_1 \nu}/\Gamma_{\tau \to e \nu \bar{\nu}}$
1.251	0.599	0.355
1.251	0.549	0.398
1.251	0.649	0.319
1.200	0.599	0.322
1.300	0.599	0.380
1.200	0.549	0.362

Table 4.7: *Kühn and Santamaria predictions for the a_1 total decay rate for different values of the a_1 mass and width.*

predictions of Table 4.7 corresponds to a variation $\Delta Br \simeq 1\%$ of the $\tau \to 3\pi\nu_\tau$ branching ratio. The present experimental error [6] on the $\tau \to 3\pi\nu_\tau$ branching ratio is 0.4%.

• **Model dependence**

The spin 1 hadronic structure functions normalized to w_A for the Isgur et al. and Feindt models are shown in Fig. 4.6, together with the predictions of Kühn and Mirkes. A value $f^D/f^S = -0.11$ is used for the Feindt model. The predictions of the models for the ratio w_C/w_A are very close to each other. The w_D and w_E form factors show a different behaviour for $Q^2 > 1.4$ GeV^2. As a matter of fact, these form factors contain interference terms where, in particular for high Q^2, the differences in the parametrizations of the Breit-Wigner terms become important.

The scalar structure functions calculated with the Isgur et al. model are compared to those of Kühn and Mirkes in Fig. 4.7. There are clear differences in the predictions. The scalar contribution to the total rate $\Gamma_{3\pi}$ is only $\simeq 1.6\%$ in the Isgur et al. model, compared with 5% of Kühn and Mirkes.

• **Conclusions**

The differences in the model predictions are sizeable enough to be experimentally accessible. However, a large sample of $\tau \to 3\pi\nu_\tau$ is needed, since all the variations are at large Q^2. On the other hand, it is important to estimate the possible biases to the P_τ measurement due to these theoretical uncertainties. A detailed discussion on the corresponding systematic error for the measurement of P_τ will be presented in Section 5.3.2.

Chapter 5

Measurement of P_τ with the decay $\tau \rightarrow 3\pi\nu_\tau$

The measurement of the τ polarization with a selected sample of $\tau \rightarrow 3\pi\nu_\tau$ decays is discussed in this chapter. The sensitivity to P_τ of various distributions is compared. In particular, a new method which fully exploits the kinematical characteristics of the a_1 decay is described. Its sensitivity to P_τ is shown to be considerably better than that of the existing methods. The data set used for the measurement has been described in Section 3.2, but the polarization analysis in addition includes a part of the statistics collected during the 1992 LEP run. Details of the systematic error estimate are given. The hadronic form factors used in the new method depend on the specific theoretical model chosen to describe the hadronic current, and the corresponding theoretical uncertainty has been carefully estimated.

5.1 Sensitivity to P_τ

In the decay $\tau \rightarrow a_1\nu \rightarrow \pi\pi\pi\nu_\tau$, the hadronic system helicity can assume the values 0 or -1 (see Fig. 5.1). The corresponding amplitudes A_0 and A_1 can be deduced from the expression of the helicity amplitudes for a spin 1 particle, and are related by $A_1/A_0 = \sqrt{2}m/m_\tau$, where $m = \sqrt{Q^2}$ is the mass of the hadronic system. Summing over the helicity states, the expected a_1 angular distribution in the τ rest frame is:

$$\frac{1}{N}\frac{dN}{d\cos\theta} = \frac{1}{2}\left(1 + P_\tau \alpha_{a_1}\cos\theta\right) \tag{5.1}$$

$$\alpha_{a_1} = \frac{|A_0|^2 - |A_1|^2}{|A_0|^2 + |A_1|^2} = \frac{m_\tau^2 - 2Q^2}{m_\tau^2 + 2Q^2}, \tag{5.2}$$

where $\cos\theta$ was defined in expression (4.74). Taking into account the Q^2 distribution of the a_1, one finds $\alpha_{a_1} \simeq 0.12$. In the case of $\tau \rightarrow \pi\nu$ decay, $\alpha_\pi = 1$ (cf. Section 1.3). As a consequence of the two possible helicity states, the sensitivity to the polarization of the $dN/d\cos\theta$ distribution is significantly reduced. New distributions should be studied in order to improve the sensitivity.
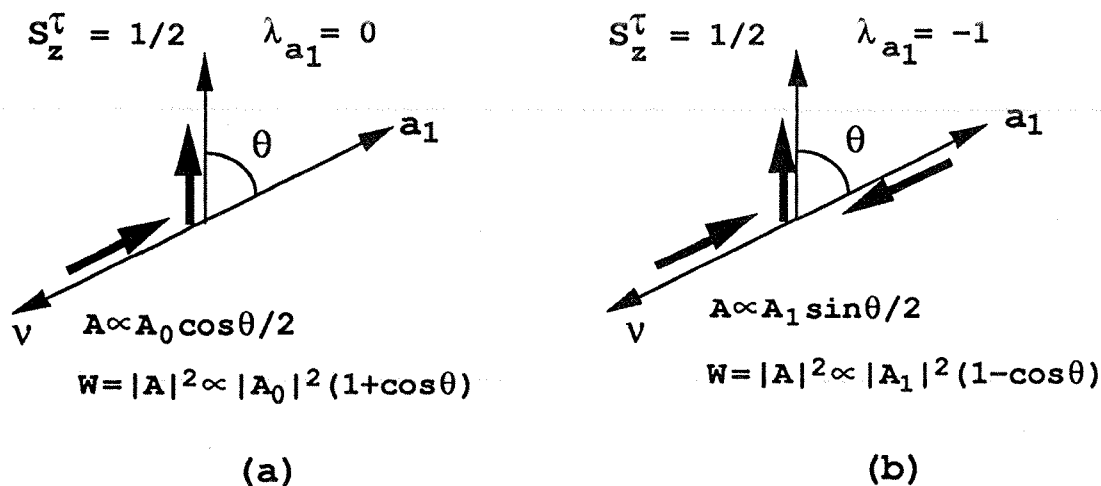
Figure 5.1: *The decay $\tau \to a_1\nu$ in the τ rest frame. The thin arrows represent particle momenta, the thick ones particle spins. Figures (a) and (b) correspond to the cases for zero and negative a_1 helicity, respectively.*

In the following, several distributions sensitive to P_τ will be shown. The definition of sensitivity given by Rougé [55] is used. Consider a general distribution which can be written in a form which shows explicitly the P_τ dependence:

$$W(\vec{x}) = f(\vec{x}) + P_\tau g(\vec{x}), \tag{5.3}$$

where $\vec{x}$ is a decay observable (or a set of observables) and the functions f and g satisfy the normalization and positivity condition: $\int f(\vec{x})d^n\vec{x} = 1$, $\int g(\vec{x})d^n\vec{x} = 0$, $f \geq 0$ and $|g| \leq f$. Given a sample of N measurements $\{\vec{x}_i\}$ of the decay observables, the measured polarization P_τ which maximizes the likelihood function $L(P_\tau, \{\vec{x}_i\})$ is determined by:

$$\log L = \sum_i \log\left(f(\vec{x}_i) + P_\tau g(\vec{x}_i)\right), \tag{5.4}$$

$$\frac{\partial}{\partial P_\tau}\log L = \sum_i \frac{g(\vec{x}_i)}{f(\vec{x}_i) + P_\tau g(\vec{x}_i)}, \tag{5.5}$$

$$-\frac{\partial^2}{\partial^2 P_\tau}\log L = \sum_i \frac{g^2(\vec{x}_i)}{(f(\vec{x}_i) + P_\tau g(\vec{x}_i))^2}. \tag{5.6}$$

The fitted value of P_τ is the solution of the equation $\partial \log L/\partial P_\tau = 0$ and its error σ_{P_τ} is determined by:

$$\frac{1}{\sigma_{P_\tau}^2} = -\frac{\partial^2}{\partial^2 P_\tau}\log L = N \int \frac{g^2}{f + P_\tau g}d\vec{x} = NS^2, \tag{5.7}$$

where S is the sensitivity. The procedure which will be used to determine the sensitivity of a given distribution is the following. The f and g functions of (5.3) are explicitly calculated for the distribution of interest. Then, N events are generated with the KORALZ [22] Monte Carlo

program. For each generated event f and g are calculated, and after summing over all events, $\sigma_{P_\tau}^2$ is obtained from expression (5.6). The sensitivity is then $S = 1/\sqrt{N\sigma_{P_\tau}^2}$. To be sure that the asymptotic approximation (5.7) for the sensitivity is valid, a large number of Monte Carlo events has been used ($N = 200000$). Notice that the sensitivity and the distributions which will be discussed below take into account the effects of radiative corrections, since these are included in the KORALZ Monte Carlo program.

5.1.1   The two dimensional $(\cos\theta, \cos\beta)$ distribution

The sensitivity can be improved by measuring the helicity of the a_1 through the decay distribution of the hadronic system [15] [16] [17]. However, the τ rest frame helicity cannot be measured because of the missing neutrino, and only the laboratory frame helicity is accessible. To compute the decay angular distribution, the components of the spin state must be rotated by the angle ψ between the direction of the boost of the pions system in the laboratory $\vec{n}_L$, and the τ both as seen from the hadronic rest frame (*cf.* expression (4.75)).

Following Rougé [17], the general decay distribution for a spin 1 hadronic system reads:

$$W(\cos\theta, \cos\beta) = \frac{3}{8(m_\tau^2 + 2Q^2)} \left[(1 + P_\tau)W^+(\cos\theta, \cos\beta) + (1 - P_\tau)W^-(\cos\theta, \cos\beta)\right], \quad (5.8)$$

where β is the angle between the normal to the decay plane and the laboratory direction (*cf.* expression (4.72)).

The explicit form of the $W^\pm$ functions is:

$$
\begin{aligned}
W^+(\cos\theta, \cos\beta) &= \sin^2\beta \left(m_\tau \cos\psi \cos\frac{\theta}{2} + \sqrt{Q^2}\sin\psi\sin\frac{\theta}{2}\right)^2 \\
&\quad + \frac{1 + \cos^2\beta}{2}\left[\left(m_\tau \sin\psi\cos\frac{\theta}{2} - \sqrt{Q^2}\cos\psi\sin\frac{\theta}{2}\right)^2 + Q^2\sin^2\frac{\theta}{2}\right] \quad (5.9)
\end{aligned}
$$

$$
\begin{aligned}
W^-(\cos\theta, \cos\beta) &= \sin^2\beta \left(m_\tau \cos\psi \sin\frac{\theta}{2} + \sqrt{Q^2}\sin\psi\cos\frac{\theta}{2}\right)^2 \\
&\quad + \frac{1 + \cos^2\beta}{2}\left[\left(m_\tau \sin\psi\sin\frac{\theta}{2} - \sqrt{Q^2}\cos\psi\cos\frac{\theta}{2}\right)^2 + Q^2\cos^2\frac{\theta}{2}\right] \quad (5.10)
\end{aligned}
$$

Notice that expression (5.8) also contains a Q^2 dependence. Thus, it should follow the Breit-Wigner distribution of the a_1. However, Rougé has shown [55] that in fixing Q^2 to the nominal a_1 mass, *i.e.* using an average decay distribution instead of the exact distribution for each mass, the loss in sensitivity is negligible. The $\cos\theta$ and $\cos\beta$ distributions for negative and positive τ helicity are shown in Fig. 5.2. The $\cos\beta$ distribution clearly is very sensitive to the τ polarization. A fit to the two dimensional distribution $(\cos\theta, \cos\beta)$ will maximize the sensitivity to P_τ. Using the procedure previously described, a sensitivity $S = 0.24$ is obtained, which corresponds to an improvement of more than a factor 2 with respect to $dN/d\cos\theta$.

Notice that the derivation of expressions (5.8)-(5.10) rests only on spin-parity considerations and not on the details of the hadronic system structure. This means that the determination of
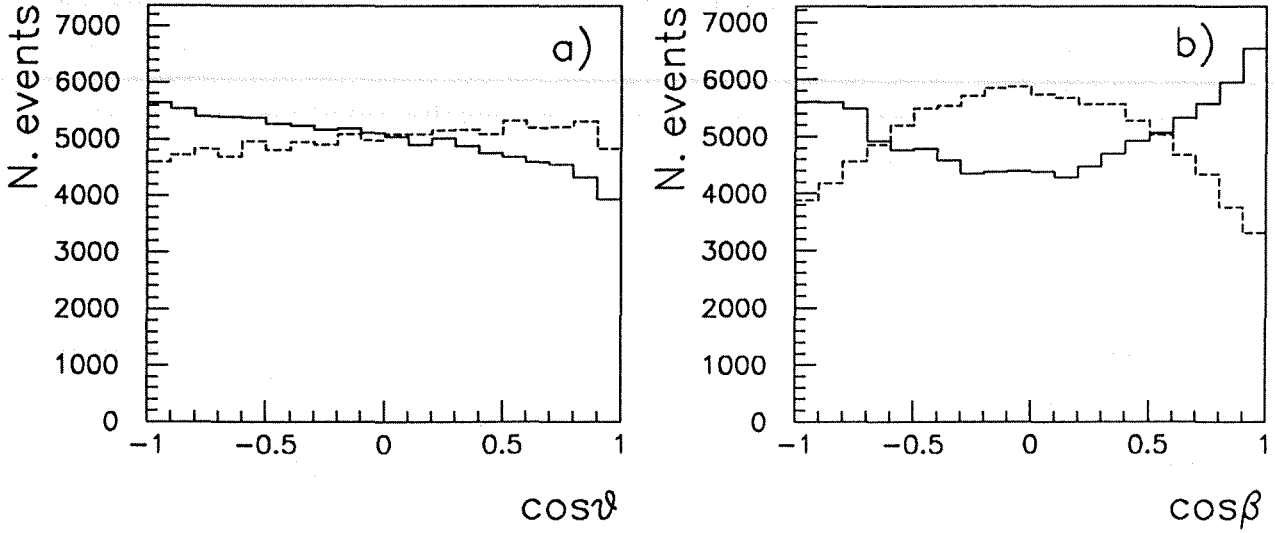
Figure 5.2: *The $\cos\theta$ a) and $\cos\beta$ b) distributions for negative (solid line) and positive (dashed line) τ helicity.*

P_τ using the $(\cos\theta, \cos\beta)$ distribution does not depend on the specific model of the hadronic current. This statement can be clarified by comparing Rougé expressions with the differential decay rate determined by Kühn and Mirkes, which has been discussed in Section 4.4. In fact, the $(\cos\theta, \cos\beta)$ distribution can be derived by integrating the decay rate (4.69) over the α and γ angles. After the integration, the decay rate is of the form:

$$d\Gamma_{\tau \to \pi\pi\pi\nu_\tau} \propto \bar{L}_A W_A d\cos\theta\, d\cos\beta\, dQ^2 ds_1 ds_2 =$$

$$\left(\frac{2}{3}K_1 + K_2 + \frac{1}{3}\bar{K}_1\frac{3\cos^2\beta - 1}{2}\right) W_A d\cos\theta\, d\cos\beta\, dQ^2 ds_1 ds_2. \quad (5.11)$$

Notice that the angular dependence is contained only in the leptonic function $\bar{L}_A$. Since W_A factorizes in expression (5.11), the specific form of the hadronic current does not affect the angular distributions, and the P_τ determination through $(\cos\theta, \cos\beta)$ is thus model-independent. Introducing the explicit expressions (4.78) for K_1, K_2 and $\bar{K}_1$ in (5.11), the Rougé decay distribution (5.8) is obtained.

From the $\cos\theta$ and $\cos\beta$ dependence of expression (5.11) one can see that all the information is contained in the two one-dimensional distributions: $dN/d\cos\theta$ and $< (3\cos^2\beta - 1)/2 > (\cos\theta)$. The last moment is a function of $\cos\theta$, since it is obtained by integrating over all the kinematical variables except $\cos\theta$. The $< (3\cos^2\beta - 1)/2 > (\cos\theta)$ distribution for negative and positive τ helicity is shown in Fig. 5.3.

Most of the sensitivity to P_τ is contained in the $< (3\cos^2\beta - 1)/2 > (\cos\theta)$ distribution. Thus a one-dimensional combined fit to the $dN/d\cos\theta$ and $< (3\cos^2\beta - 1)/2 > (\cos\theta)$ distributions can be performed to determine P_τ, without any loss in the sensitivity.

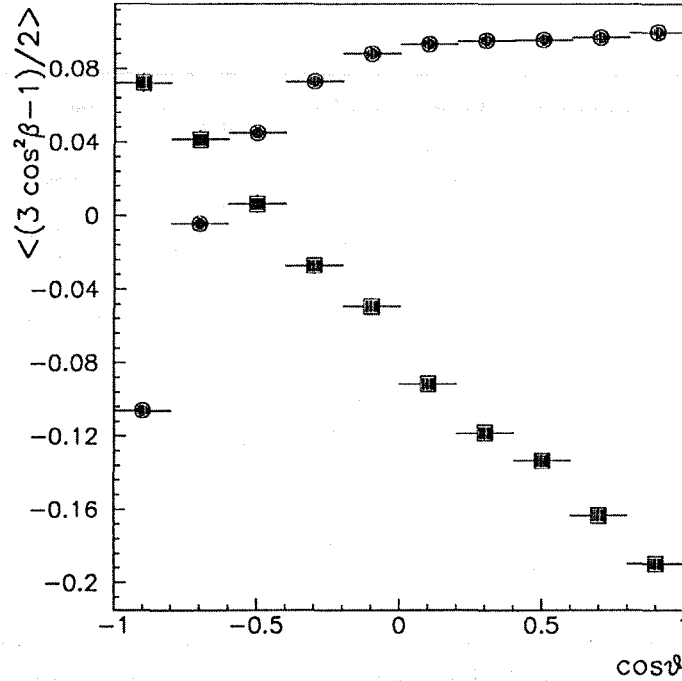**Figure 5.3:** *The* $< (3\cos^2\beta - 1)/2 >$ $(\cos\theta)$ *distribution for negative (dots) and positive (squares)* τ *helicity.*

5.1.2 Improved sensitivity to P_τ using all the decay variables

In Section 4.4 the most general decay distribution for $\tau \to 3\pi\nu_\tau$ determined by Kühn and Mirkes was discussed in detail. The authors emphasized that the use of all the decay variables $\cos\theta$, γ, $\cos\beta$, s_1, s_2, and Q^2 allows a determination of the hadronic form factors.

In this Section it will be shown that a major improvement of the sensitivity to P_τ is also achieved.

The decay rate can be written (*cf.* Section 4.4):

$$d\Gamma_{\tau \to \pi\pi\pi\nu_\tau} \propto \sum_X \bar{L}_X W_X d\cos\theta d\cos\beta dQ^2 ds_1 ds_2. \tag{5.12}$$

A multi-dimensional fit can thus be performed in order to determine P_τ. Notice that all the P_τ dependence is contained in the leptonic functions $\bar{L}_X$. However, the hadronic form factors do not factorize in expression (5.12). Hence, for a given set of $\cos\theta$, γ, $\cos\beta$, s_1, s_2, and Q^2, the $W_X(s_1, s_2, Q^2)$ must be calculated in order to perform the fit. In general, the result will depend on the particular model assumed for the hadronic current. The model dependence of the P_τ measurement with the method proposed here is discussed in detail in Section 5.3.

The improvement in the sensitivity to P_τ is most easily understood in terms of one-dimensional

distributions. Given the form (4.77) of the $\bar{L}_X$, an appropriate set of moments can be used:

$$< 1 > (\cos\theta) = \int (2K_1 + 3K_2)w_A dQ^2 \tag{5.13}$$

$$< (3\cos^2\beta - 1)/2 > (\cos\theta) = \frac{1}{5} \int \bar{K}_1 w_A dQ^2 \tag{5.14}$$

$$< \cos 2\gamma > (\cos\theta) = -\frac{1}{2} \int \bar{K}_1 w_C dQ^2 \tag{5.15}$$

$$< \sin 2\gamma\, sign(s_1 - s_2) > (\cos\theta) = \frac{1}{2} \int \bar{K}_1 w_D dQ^2 \tag{5.16}$$

$$< \cos\beta\, sign(s_1 - s_2) > (\cos\theta) = \int \bar{K}_3 w_E dQ^2 \tag{5.17}$$

which are derived from moments (4.83)-(4.89) by integrating over s_1, s_2 and Q^2. The contribution from a scalar current, which is expected to be small, is neglected ($W_{SA} = W_{SB} = W_{SC} = W_{SD} = W_{SE} = 0$).

The first two moments are equivalent to the $dN/d\cos\theta$ and $< (3\cos^2\beta - 1)/2 > (\cos\theta)$ distributions used in the previous Section.

A significant improvement in the sensitivity to P_τ is expected with the use of the moment $< \cos 2\gamma > (\cos\theta)$. In fact, its P_τ dependence ($\bar{K}_1$) is identical to that of $< (3\cos^2\beta - 1)/2 > (\cos\theta)$ and its hadron form factor w_C/w_A is about unity, as was shown in Section 4.6. A sensitivity of the same order of that of $< (3\cos^2\beta - 1)/2 > (\cos\theta)$ then should be achieved.

In the case of the last two moments $|w_D|/w_A \leq 0.2$ and $|w_E|/w_A \leq 0.3$. Thus, their contributions to the sensitivity are expected to be smaller.

The $dN/d\cos\theta$ and $< (3\cos^2\beta - 1)/2 > (\cos\theta)$ distributions have been shown in Fig. (5.2) and (5.3). The distributions of the other moments for negative and positive τ helicity are shown in Fig. (5.4) and Fig. (5.5). In Fig. (5.4) the $\cos\gamma$ distribution is also plotted. The sensitivities to P_τ for the different moments are summarized in Table 5.1.

Moment	Sensitivity
$A = < 1 > (\cos\theta)$	0.10
$B = < (3\cos^2\beta - 1)/2 > (\cos\theta)$	0.22
$C = < \cos 2\gamma > (\cos\theta)$	0.32
$D = < \sin 2\gamma\, sign(s_1 - s_2) > (\cos\theta)$	0.13
$E = < \cos\beta\, sign(s_1 - s_2) > (\cos\theta)$	0.13
$A + B + C + D + E$	0.44

Table 5.1: *The sensitivity to P_τ for the different moments discussed in the text.*

Combining all the moments, the expected sensitivity is given by $S = \sqrt{\sum_i S_i^2} = 0.44$. Therefore, an improvement of $\simeq 2$ is achieved with respect to the usual $(\cos\theta, \cos\beta)$ analysis if all the decay variables are used. To clarify this point, the comparison of the sensitivity to P_τ for the different decay channels (*cf.* Section 1.3) is presented again in Table 5.2. The contribution
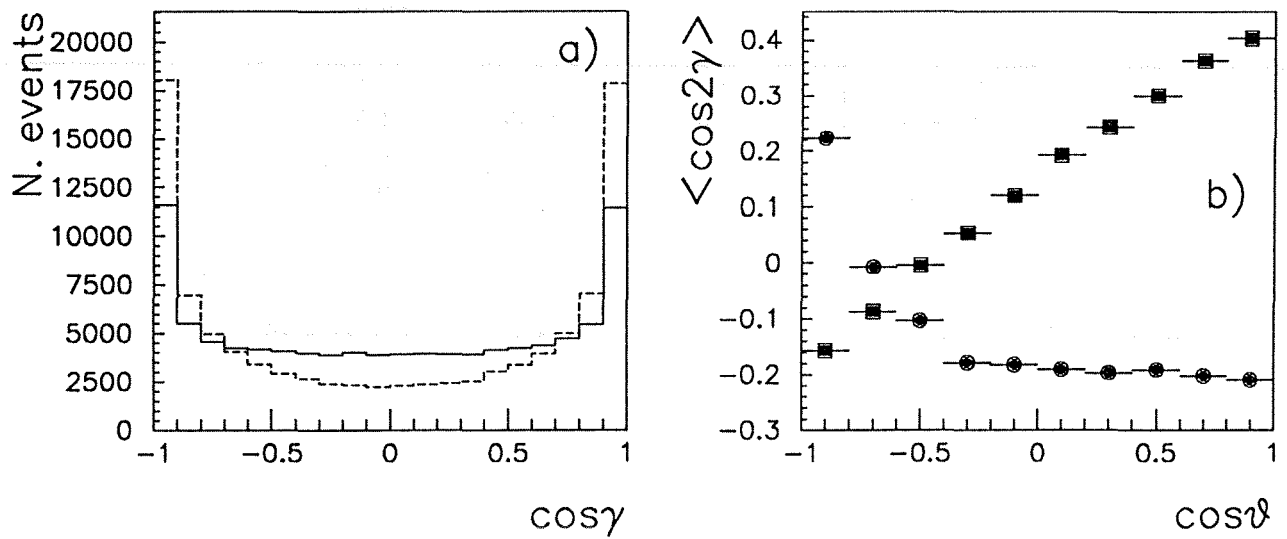
Figure 5.4: *a) the* $\cos\gamma$ *distribution for negative (solid line) and positive (dashed line)* τ *helicity, b) the* $<\cos2\gamma>$ $(\cos\theta)$ *distribution for negative (dots) and positive (squares)* τ *helicity.*
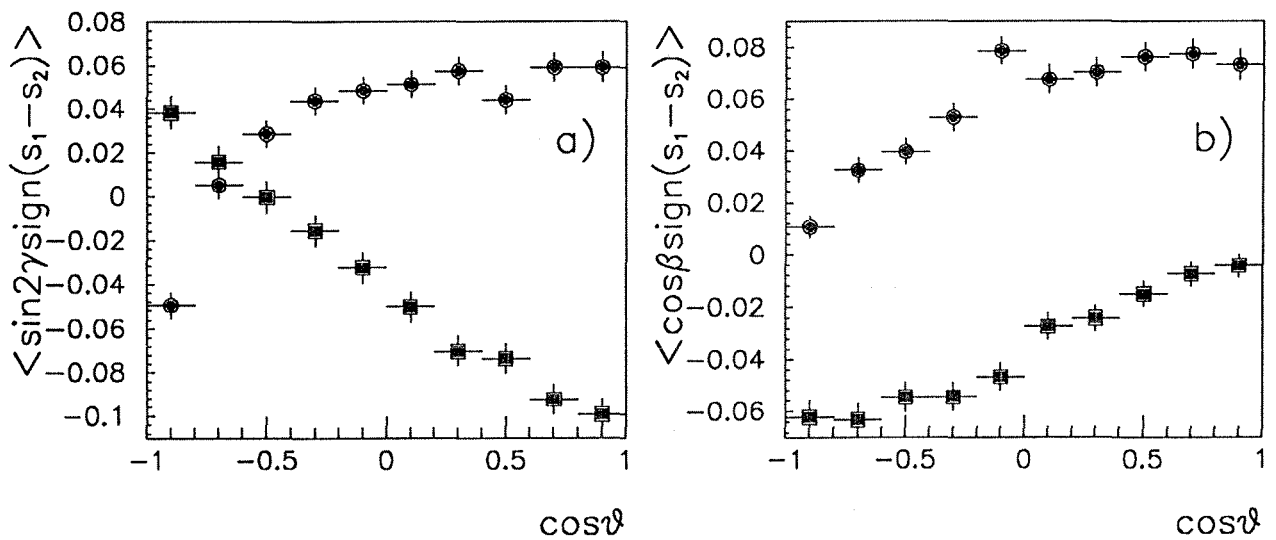
Figure 5.5: *a) the* $<\sin2\gamma\,sign(s_1-s_2)>$ $(\cos\theta)$ *distribution for negative (dots) and positive (squares)* τ *helicity, b) the* $<\cos\beta\,sign(s_1-s_2)>$ $(\cos\theta)$ *distribution for negative (dots) and positive (squares)* τ *helicity.*

Decay mode	$S_X = (\Delta P_\tau \sqrt{N})^{-1}$	B_X	Relative weight $S_X^2 B_X$
$\tau \to \pi\nu$	0.6	0.11	1
$\tau \to \rho\nu$	0.52	0.23	1.6
$\tau \to a_1\nu$	0.44(0.24)	0.08	0.4(0.1)
$\tau \to e\nu\bar\nu$	0.22	0.18	0.2
$\tau \to \mu\nu\bar\nu$	0.22	0.18	0.2

Table 5.2: *Sensitivity, branching ratio and relative weight for the different τ decay modes. For $\tau \to a_1\nu$, the values determined with the method presented in this Section are reported. For comparison, the corresponding values for the usual two-dimensional ($\cos\theta, \cos\beta$) fit are quoted in parenthesis. The relative weights are normalized with respect to the $\tau \to \pi\nu$ channel.*

of the $\tau \to a_1\nu$ channel to the precision on P_τ given by the combination of the different decay modes is improved by a factor of about 4 (0.1 → 0.4), and in both sensitivity and relative weight is equivalent to the leptonic channels $\tau \to e\nu\bar\nu$ and $\tau \to \mu\nu\bar\nu$ combined.

5.1.3   The full sensitivity in a one-dimensional distribution

Rougé [55] has proposed a simple method to reduce the problem of a multi-dimensional fitting to a one-dimensional one. Notice that expressions (5.5)-(5.6) can be rewritten as:

$$\frac{\partial}{\partial P_\tau} \log L = \sum_i \frac{g(\vec{x}_i)/f(\vec{x}_i)}{1 + P_\tau g(\vec{x}_i)/f(\vec{x}_i)}, \tag{5.18}$$

$$-\frac{\partial^2}{\partial^2 P_\tau} \log L = \sum_i \frac{(g(\vec{x}_i)/f(\vec{x}_i))^2}{(1 + P_\tau g(\vec{x}_i)/f(\vec{x}_i))^2}. \tag{5.19}$$

Given a set of decay observables $\vec{x}$, the variable $\xi = g(\vec{x})/f(\vec{x})$ can be computed. The distribution of the ξ variable is given by:

$$\begin{aligned}
W(\xi) &= \int W(\vec{x})\delta\left(\xi - \frac{g(\vec{x})}{f(\vec{x})}\right) d\vec{x} \\
&= \int f(\vec{x})\delta\left(\xi - \frac{g(\vec{x})}{f(\vec{x})}\right) d\vec{x} + P_\tau \int g(\vec{x})\delta\left(\xi - \frac{g(\vec{x})}{f(\vec{x})}\right) d\vec{x} \\
&= \hat{f}(\xi) + P_\tau \hat{g}(\xi) = \hat{f}(\xi)(1 + P_\tau\xi),
\end{aligned} \tag{5.20}$$

where $\hat{f}$ and $\hat{g}$ are given by the corresponding integrals and the last equation is obtained by setting $g(\vec{x}) = \xi f(\vec{x})$. It is easy to verify that $\hat{f}$ and $\hat{g}$ satisfy the same normalization and positivity conditions of f and g. Notice that a fit to P_τ using $W(\xi)$ is equivalent to a fit using $W(\vec{x})$. In fact, substituting in (5.18) $g(\vec{x})/f(\vec{x}) = \xi$, it is clear that in both cases the fitted value of P_τ is a solution of $\sum_i \xi_i/(1 + P_\tau\xi_i) = 0$. Similarly, the error on the estimated P_τ is the same since it is given by (5.19).

The $\tau \to 3\pi\nu_\tau$ decay rate distribution (5.12) can be written in a form like (5.3), where $\vec{x} = (\cos\theta, \gamma, \cos\beta, s_1, s_2, Q^2)$. The explicit expressions for $f(\vec{x})$ and $g(\vec{x})$ can be derived from (4.77)-(4.78):

$$
\begin{aligned}
f(\cos\theta, \gamma, \cos\beta, s_1, s_2, Q^2) =\ & \left[\frac{1}{3}\left(2 + \frac{m_\tau^2}{Q^2}\right) + \frac{3\cos^2\beta - 1}{12}(3\cos^2\psi - 1)\left(1 - \frac{m_\tau^2}{Q^2}\right)\right] W_A \\
& -\frac{1}{4}\sin^2\beta\cos 2\gamma(3\cos^2\psi - 1)\left(1 - \frac{m_\tau^2}{Q^2}\right) W_C \\
& +\frac{1}{4}\sin^2\beta\sin 2\gamma(3\cos^2\psi - 1)\left(1 - \frac{m_\tau^2}{Q^2}\right) W_D \\
& +\gamma_{VA}\cos\psi\cos\beta W_E
\end{aligned}
\tag{5.21}
$$

$$
\begin{aligned}
g(\cos\theta, \gamma, \cos\beta, s_1, s_2, Q^2) =\ & \frac{\gamma_{VA}}{3}\Bigg\{\cos\theta\left(\frac{m_\tau^2}{Q^2} - 2\right) - \frac{3\cos^2\beta - 1}{4} \\
& \times\left[(3\cos^2\psi - 1)\cos\theta\left(1 + \frac{m_\tau^2}{Q^2}\right) + 3\sin 2\psi\sqrt{\frac{m_\tau^2}{Q^2}}\sin\theta\right]\Bigg\} W_A \\
& +\frac{\gamma_{VA}}{4}\sin^2\beta\cos 2\gamma\left[(3\cos^2\psi - 1)\cos\theta\left(1 + \frac{m_\tau^2}{Q^2}\right) + 3\sin 2\psi\sqrt{\frac{m_\tau^2}{Q^2}}\sin\theta\right] W_C \\
& -\frac{\gamma_{VA}}{4}\sin^2\beta\sin 2\gamma\left[(3\cos^2\psi - 1)\cos\theta\left(1 + \frac{m_\tau^2}{Q^2}\right) + 3\sin 2\psi\sqrt{\frac{m_\tau^2}{Q^2}}\sin\theta\right] W_D \\
& -\cos\beta\left(\cos\theta\cos\psi + \sin\theta\sin\psi\sqrt{\frac{m_\tau^2}{Q^2}}\right) W_E.
\end{aligned}
\tag{5.22}
$$

One can verify that $g(\vec{x})$ in (5.22) satisfies $\int g(\vec{x})d^n\vec{x} = 0$. Notice that the $f(\vec{x})$ in (5.21) is not normalized to unity. The reason is that the normalization factor is the same for both $f(\vec{x})$ and $g(\vec{x})$, and thus it cancels in their ratio ξ. The Standard Model prediction for the chirality parameter $\gamma_{VA} = 1$ is assumed.

The ξ distribution for negative and positive τ helicity is shown in Fig. 5.6. The two distributions are clearly separated. The corresponding sensitivity is $S = 0.44$, as expected from the results of the previous Section.

The method has the advantage of keeping the full sensitivity in only one distribution, which is easy to display and compare with the data with respect to the multi-dimensional one. However, particular care should be taken when dealing with real data, since possible biases could be difficult to recognize on the basis of the ξ distribution alone. To be confident of the fitted result, independent distributions like the moments presented in the previous Section also should be fitted and compared to the data.
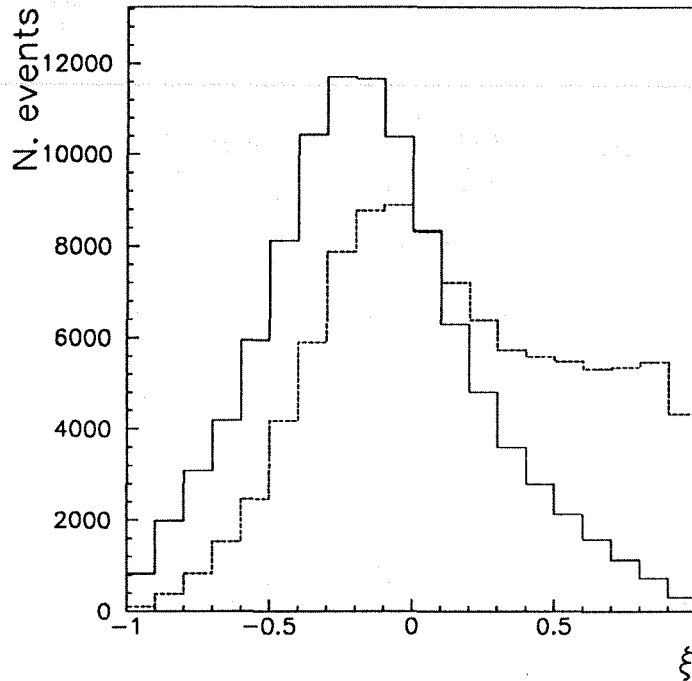
Figure 5.6: *The ξ distribution for negative (solid line) and positive (dashed line) τ helicity.*

5.2   Measurement of P_τ

5.2.1   The data sample

The selection of a sample of $\tau \to 3\pi\nu_\tau$ candidates has been described in Section 3.2. For the polarization measurement, the three pions are assumed to be produced in the chain $a_1^- \to \rho^0\pi^-$ (and its charge conjugate). Thus, at least one of the possible $\pi^+\pi^-$ combinations is expected to originate from the ρ^0 resonance, whereas the $\pi^-\pi^-$ combination is non-resonant. This behaviour is indeed seen in the data. In Fig. 5.7 the invariant mass $m_{\pi^+\pi^-}$ for the two $\pi^+\pi^-$ combinations per event is shown in a two-dimensional plot. The $\pi^+\pi^-$ combination with the highest invariant mass has been chosen always for the horizontal axis, thus folding in one band the ρ resonance. The invariant masses for the unlike sign combinations (two entries per event) and for the like sign combination are shown in Fig. 5.8. In the scatter plot, events are clearly distributed in bands around the ρ mass. A clear ρ^0 signal is visible in the unlike sign combinations.

To enhance the $\tau \to a_1\nu \to \rho\pi\nu_\tau$ signal, an additional cut is used:

- at least one of the two possible $\pi^+\pi^-$ combinations should satisfy $0.6 < m_{\pi^+\pi^-} < 1.2$.

Notice that this cut is not symmetric with respect to the ρ mass ($\simeq 0.77$ GeV). The reason
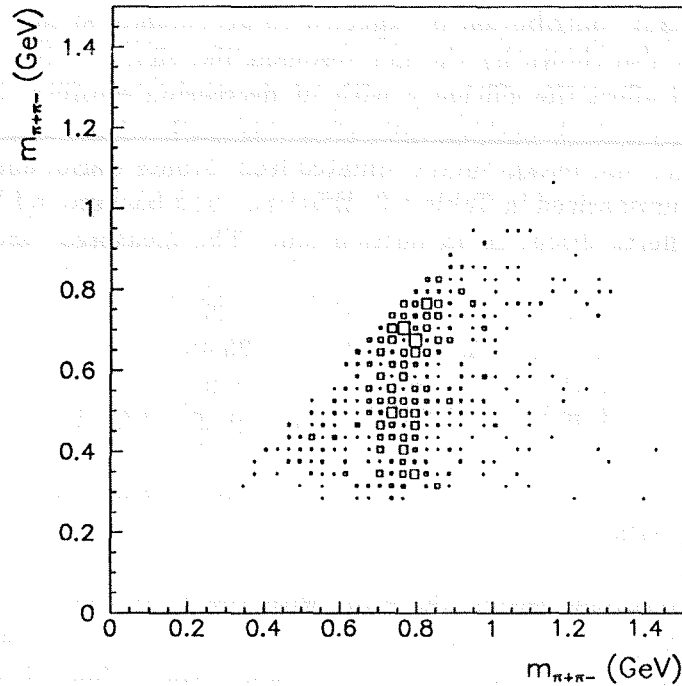
Figure 5.7: *Two dimensional plot for the correlation of the invariant masses $m_{\pi^+\pi^-}$ of the two unlike sign combinations. The box dimension is proportional to the number of entries. The $\pi^+\pi^-$ combination with the highest invariant mass has been chosen always for the horizontal axis, thus folding in one band the ρ resonance. The plot refers to the selected data sample.*
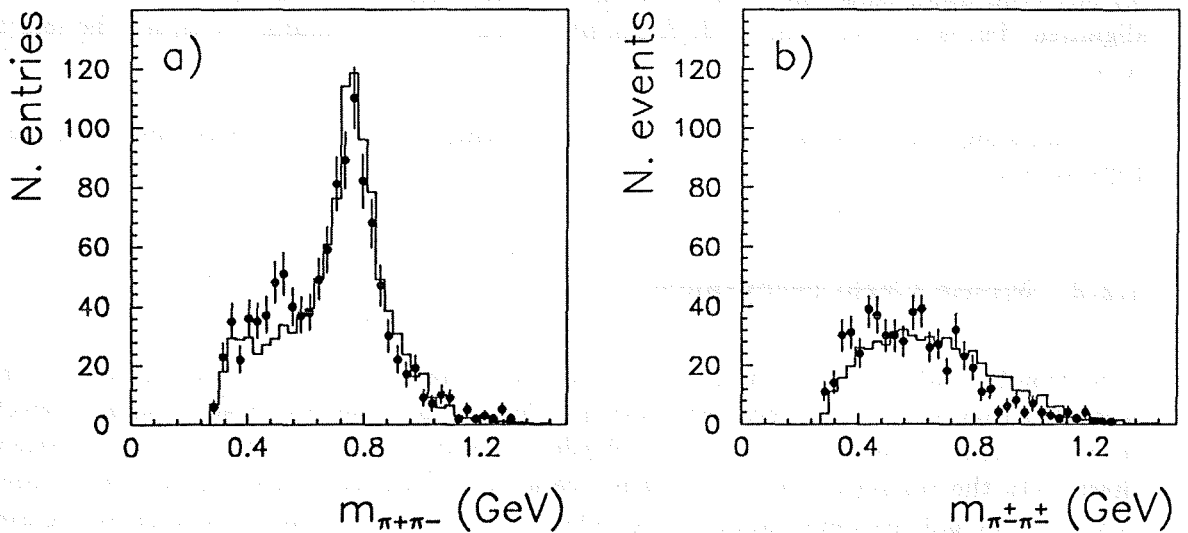
Figure 5.8: *The invariant masses $m_{\pi^+\pi^-}$ (two entries per event) for the unlike sign combinations a) and $m_{\pi^\pm\pi^\pm}$ for the like-sign combination b). Data are represented by dots, while the solid line is the Monte Carlo expectation.*

is that the non-resonant contribution is expected to accumulate at low values of the $\pi^+\pi^-$ invariant mass, as is also shown by the non-resonant like-sign distribution of Fig. 5.8. A symmetric cut would affect the efficiency without decreasing sensibly the background. To check for possible biases, the branching ratio after this cut has been computed. The number of events, the efficiency and background estimated from Monte Carlo, and the corresponding branching ratio are summarized in Table 5.3. Efficiency and background have been corrected for the systematic effects discussed in Section 3.6. The measured value of the $\tau \to a_1\nu$

$N_{\tau \to a_1\nu}$	520
$\epsilon_{\tau \to a_1\nu}$ (%)	25.48
$f_{bkg}^{non-\tau \to a_1\nu}$ (%)	5.92
$Br(\tau \to a_1\nu)$ (%)	$7.98 \pm 0.35 \pm 0.28$

Table 5.3: *Summary of $\tau \to a_1\nu \to 3\pi\nu_\tau$ branching ratio. The first error is statistical, the second error is systematic.*

branching ratio is consistent within the error with the $\tau \to 3\pi\nu_\tau$ measurement $Br(\tau \to 3\pi\nu_\tau) = 8.35 \pm 0.35 \pm 0.24\%$ *(cf.* Section 3.7). In particular it is compatible with the recent ARGUS [53] limit of less than 6% non-$\rho\pi$ contribution to the 3π final state at 95% confidence level.

The data used so far were collected in the 1991 LEP run. The DELPHI detector has successfully collected data during the 1992 LEP run, accumulating a total of $\simeq 750000\ Z^0 \to q\bar{q}$ for an integrated luminosity of $\simeq 23\ pb^{-1}$. The detector performance during 1992 has been very stable, and comparable to the 1991 run. For the P_τ measurement, a part of 1992 statistics, corresponding to an integrated luminosity of $\simeq 14\ pb^{-1}$, has been included. Only a partial set has been used, since the 1992 data reprocessing with correct calibration constants and alignment files is not yet completed. A sample of 808 $\tau \to a_1\nu$ candidates passed the selection cuts.

The final sample of $\tau \to a_1\nu$ candidates used for the P_τ measurement is thus composed of 1328 events.

5.2.2   Monte Carlo acceptance

In Section 5.1 the sensitivity to the τ polarization has been studied in the ideal case of perfect reconstruction of the $\tau \to 3\pi\nu_\tau$ decay observables. In fact, detector resolution and selection cuts can modify the shape of the distributions sensitive to P_τ. Thus, it is important to check both the resolution and the acceptance for these distributions. Given the complexity of the events and the importance of a detailed description of the detector, a complete Monte Carlo simulation, using the KORALZ [22] event generator with detector response simulated by DELSIM [21], and the 'events' processed with the standard DELPHI analysis programs (DELANA [23]), is used for this purpose.

In Fig. 5.9 $\cos\theta_{rec} - \cos\theta_{gen}$ is plotted, where $\cos\theta_{rec}$ is the value of $\cos\theta$ calculated from the reconstructed kinematical quantities after detector simulation and $\cos\theta_{gen}$ is the corresponding
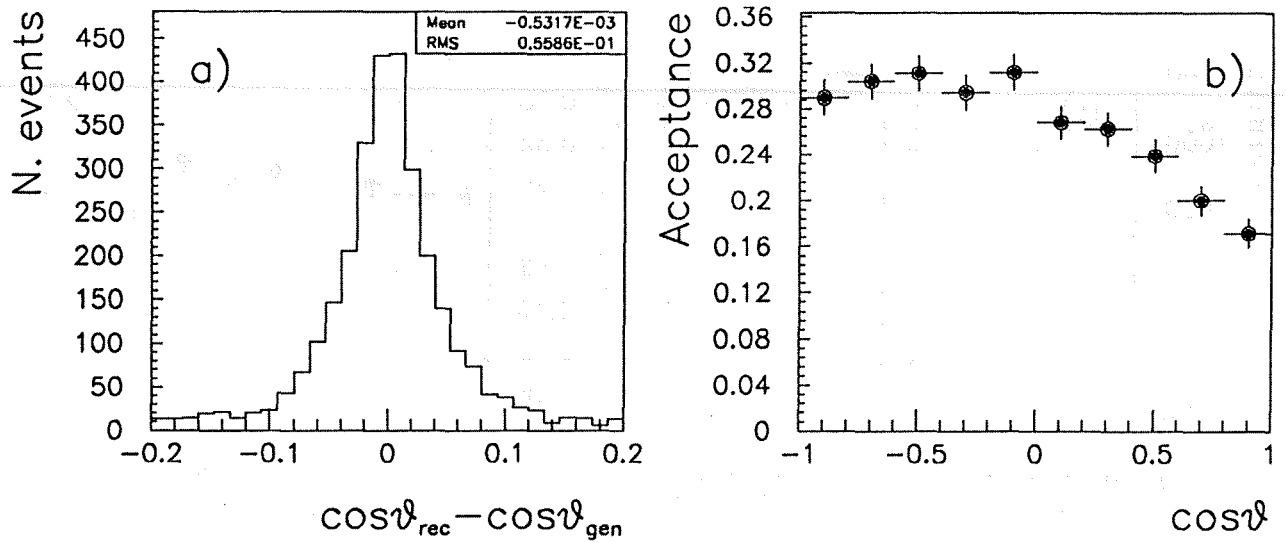
Figure 5.9: *a) the difference between the reconstructed and generated* $\cos\theta$*, b) the* $\cos\theta$ *acceptance.*

value calculated from the Monte Carlo generated quantities. The mean value and the root mean square (RMS) of the distribution is reported. The $\cos\theta$ acceptance is also shown, where the acceptance in a given $\cos\theta$ bin is defined as the ratio of the number of reconstructed events after $\tau \to a_1\nu$ selection cuts to the number of originally generated events. Notice that this definition of the acceptance includes the $e^+e^- \to \tau^+\tau^-$ selection, and in particular the geometrical acceptance as well which is restricted to the barrel region. The equivalent distributions for $\cos\beta$, $\cos\gamma$, $m_\rho(= \sqrt{s_1}, \sqrt{s_2})$ and Q^2 are shown in Fig. 5.10-5.13.

It is important that all the distributions of the difference between reconstructed and generated variables have approximately gaussian shapes and are centered at zero. One can conclude that no systematic shift is expected in the reconstruction of the angular and kinematical variables used for the P_τ measurement. Moreover, the resolution for each of the variables is well within the bin size which will be used for the actual fit to P_τ (for example, a bin size of 0.2 is used for $\cos\theta$).

As far as the acceptances are concerned, a reasonably flat behaviour is observed. The $\cos\theta$ acceptance shown in Fig. 5.9 decreases with increasing $\cos\theta$. This can be understood since increasing $\cos\theta$ corresponds to increasing $E_{3\pi}$. For large $E_{3\pi}$, the three pions are highly collimated and the probability of losing the event because of overlap between tracks increases. Also, the P_{rad} cut used for the $\tau^+\tau^-$ selection tends to reject events with large $E_{3\pi}$. This also explains the higher tails in $\cos\theta$ resolution with respect to $\cos\beta$ and $\cos\gamma$, since for high momentum tracks the momentum reconstruction is less accurate.

The $\cos\beta$ and $\cos\gamma$ acceptances are practically constant.

Figure 5.10: *a) the difference between the reconstructed and generated* $\cos\beta$, *b) the* $\cos\beta$ *acceptance.*

Figure 5.11: *a) the difference between the reconstructed and generated* $\cos\gamma$, *b) the* $\cos\gamma$ *acceptance.*
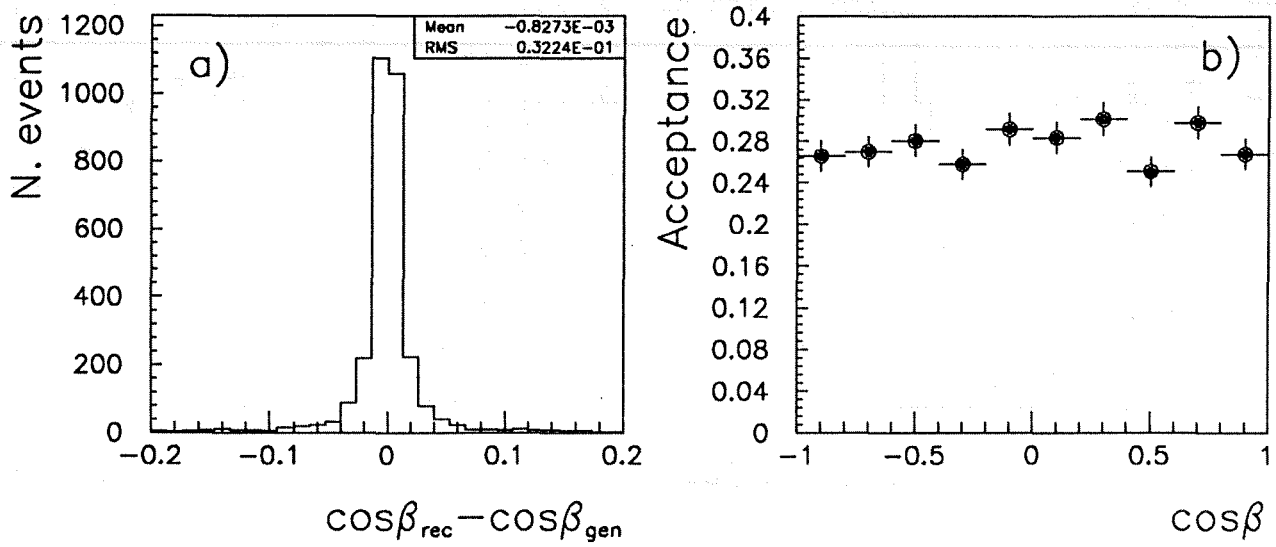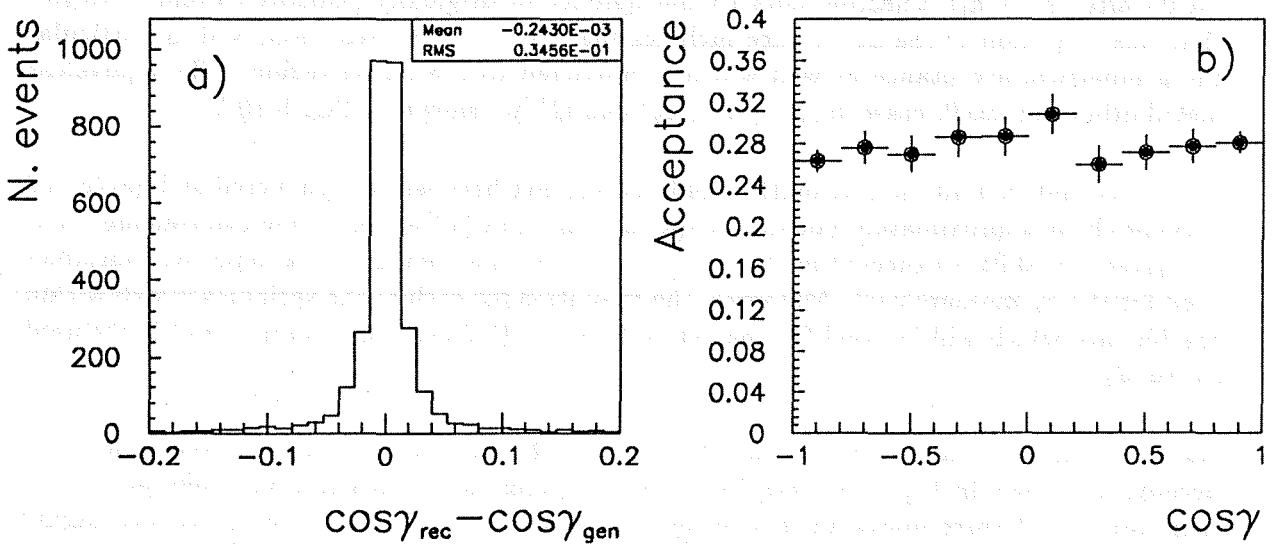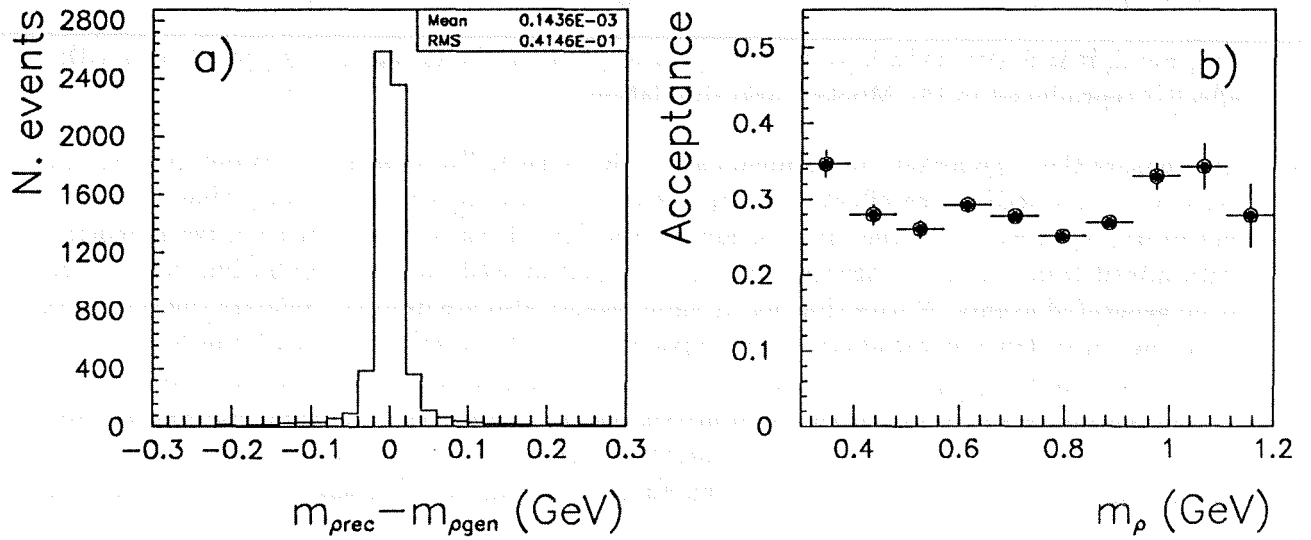
Figure 5.12: *a) the difference between the reconstructed and generated m_ρ, b) the m_ρ acceptance.*
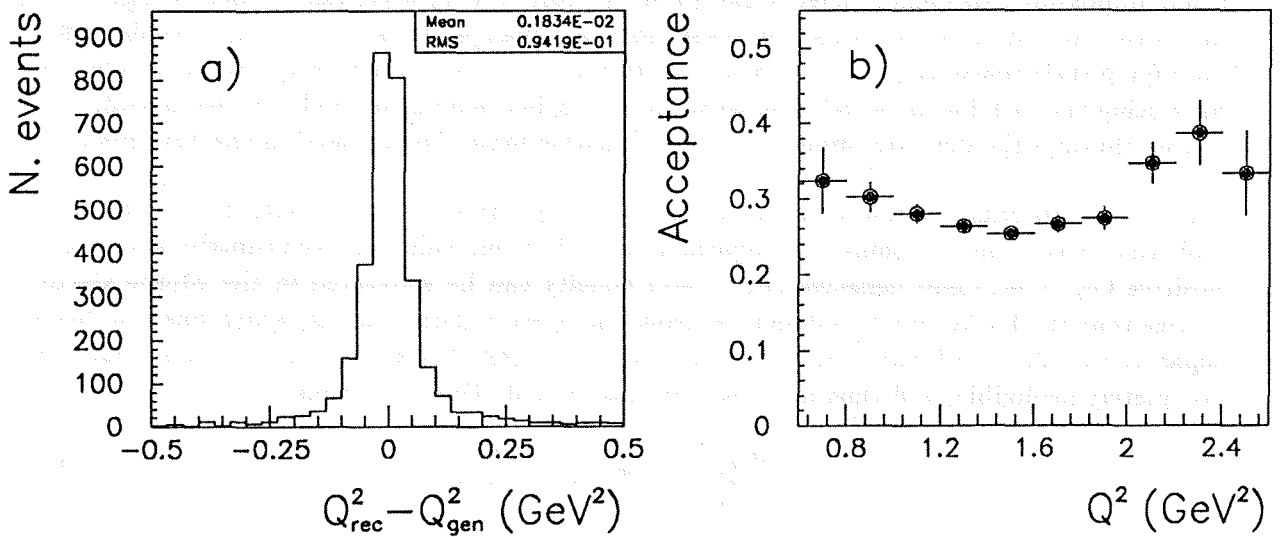

Figure 5.13: *a) the difference between the reconstructed and generated Q^2, b) the Q^2 acceptance.*

Also, the m_ρ and Q^2 acceptances in Fig. 5.12 and 5.13 are flat, particularly in the region where most of the events have been collected. Notice that the effect of the additional m_ρ cut ($0.6 < m_\rho < 1.2$) does not seem to produce a significant bias in the acceptance.

In general, it is desirable to have flat acceptances, but this is not necessary provided that the effect is reproduced in the Monte Carlo simulation.

To measure the τ polarization, moments also will be used. Systematic biases due to detector resolution and acceptance effects are expected to be minimized when calculating moments. For example, in Fig. 5.14 the distribution $< (3 \cos^2\beta - 1)/2 > (\cos\theta)$ for negative τ helicity, determined from the reconstructed events, is superimposed on the distribution determined from generated events. Notice that background events also are used to calculate the moments with the reconstructed variables. The equivalent $< \cos 2\gamma > (\cos\theta)$ distribution for positive τ helicity also is shown. It is interesting to see that moments calculated from reconstructed events reproduce the original generated distributions. The background contributions are also included, and there is no evidence of a significant effect on the moment values. Therefore, the systematic uncertainty is expected to be small when estimating P_τ from a fit to the moments.

Finally, in Fig. 5.15 $\xi_{rec} - \xi_{gen}$ and the ξ acceptance are shown. Also in this case the acceptance is flat, apart for a small decrease near $\xi = +1$.

5.2.3   Fitting procedures

In order to determine P_τ, a fit to the data distributions must be performed. One possible approach is to adjust the data to analytical formulae. However, in this case it is very difficult, if not impossible, to include effects like radiative corrections, acceptances and background. Moreover, acceptances and detector resolution can change the shape of the distributions, modifying their sensitivity to P_τ with respect to the ideal case. A better approach is to fit the data using the distributions obtained with Monte Carlo events generated with KORALZ, and passed through the detector simulation, event reconstruction, and selection analysis chain.

The fitting procedure is described in the case of the ξ variable, but its extension to the $\cos\theta$ and $(\cos\theta, \cos\beta)$ distributions is straightforward. After selection cuts, the contributions from positive ($P_\tau = +1$) and negative ($P_\tau = -1$) helicity can be separated in the Monte Carlo. Notice that the background contribution from the other τ decay modes, which has also been separated in $P_\tau = +1$ and -1, is included in the distributions. The non-τ background is completely negligible, and thus no subtraction is needed. One can define:

$$\Psi_+(\xi) = \frac{dn_+(\xi)}{d\xi} \qquad \Psi_-(\xi) = \frac{dn_-(\xi)}{d\xi}, \tag{5.23}$$

with

$$\int \Psi_+(\xi)d\xi = n_+ \qquad \int \Psi_-(\xi)d\xi = n_- \tag{5.24}$$

where $n_+(n_-)$ is the number of accepted positive(negative) helicity Monte Carlo $\tau \to a_1\nu$ candidates. Notice that $n_- > n_+$, since the events have been generated with a polarization
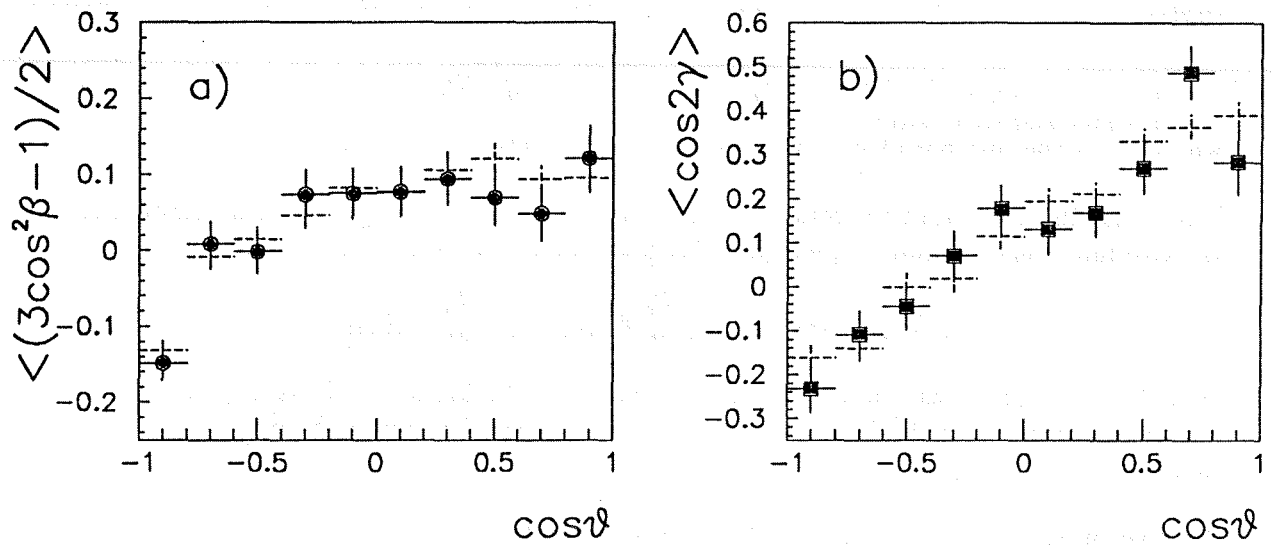
Figure 5.14: *a) the distribution $< (3\cos^2\beta-1)/2 > (\cos\theta)$ for negative τ helicity determined from the reconstructed events (dots) superimposed on the distribution determined from the generated events (dashed lines), b) the equivalent $< \cos 2\gamma > (\cos\theta)$ distributions for positive τ helicity.*
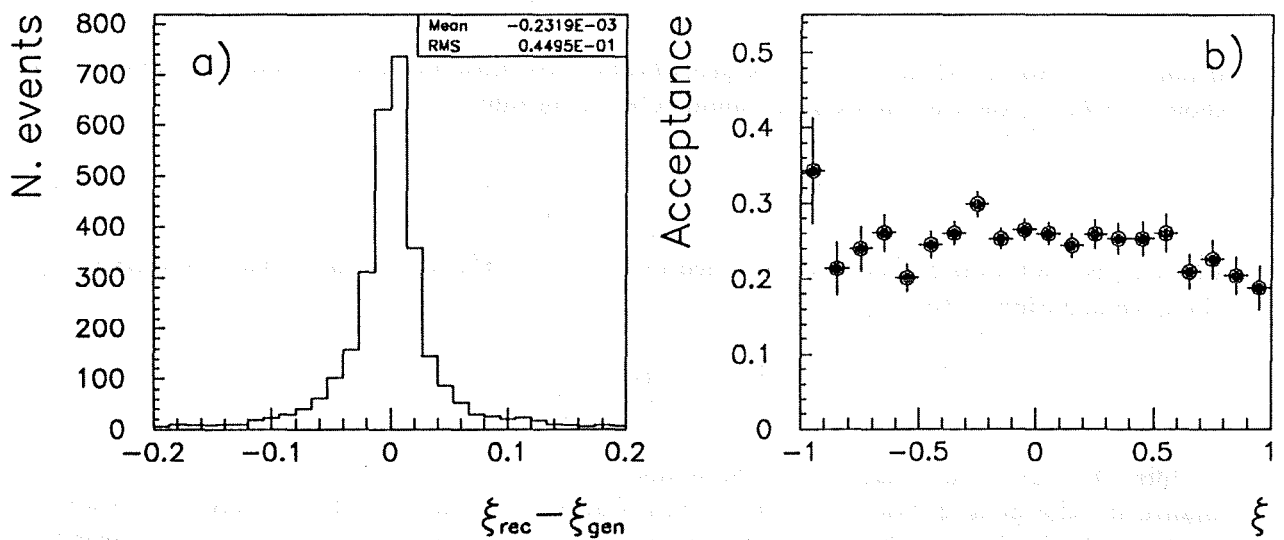

Figure 5.15: *a) the difference between the reconstructed and generated ξ, b) the ξ acceptance.*

$P_0 < 0$. One must thus normalize the functions Ψ_+ and Ψ_- with the number of $\tau \to a_1\nu$ events with $P_\tau = \pm 1$ before selection $(N_\pm)$ which depend on the polarization P_0 in the Monte Carlo:

$$N_+ = \frac{1 + P_0}{2} N_\tau \quad N_- = \frac{1 - P_0}{2} N_\tau,\qquad (5.25)$$

where N_τ is the number of $\tau \to a_1\nu$ events before selection.

The ξ distribution obtained from the data sample can then be adjusted to a combination of the two functions Ψ_+ and Ψ_-, weighted with the fitting parameter P_τ:

$$\Lambda(P_\tau, \xi) = N(P_\tau) \left[\frac{1 + P_\tau}{1 + P_0} \Psi_+(\xi) + \frac{1 - P_\tau}{1 - P_0} \Psi_-(\xi) \right].\qquad (5.26)$$

$N(P_\tau)$ is the normalization factor which depends on the Monte Carlo statistics and also on the polarization P_τ if the selection efficiency is different for events of positive and negative helicity.

To perform the actual fit, data and Monte Carlo events are histogrammed in 20 bins between $\xi = -1$ and $\xi = +1$. A maximum likelihood fit is then used, which consists of maximizing an appropriate probability function $L(P_\tau)$:

$$L(P_\tau) = \prod_{i=1}^{20} P(P_\tau, \xi_i)\qquad (5.27)$$

where $P(P_\tau, \xi_i)$ is the appropriate normalized probability of observing the given content of bin i. In practice, it is easier to minimize the function $S(P_\tau) = -\log L(P_\tau)$

$$S(P_\tau) = -\sum_{i=1}^{20} \log P(P_\tau, \xi_i).\qquad (5.28)$$

If normalized to unity, $\Lambda(P_\tau, \xi)$ is the probability distribution of the variable ξ. The obvious choice for $L(P_\tau)$ then becomes a multinomial distribution:

$$L(P_\tau) = n_{tot}! \prod_{i=1}^{20} \frac{[\Lambda(P_\tau, \xi_i)]^{n_i}}{n_i!}\qquad (5.29)$$

where n_i is the number of events contained in bin i, and $\Lambda(P_\tau, \xi)$ is normalized to unity using the normalization factor:

$$N(P_\tau) = \frac{1}{\sum_{i=1}^{20} \Lambda(P_\tau, \xi_i)}\qquad (5.30)$$

A different procedure is used to fit the moments, since in this case there is no need to normalize for the polarization P_0 in the Monte Carlo generation. In fact, taking as example $<(3\cos^2\beta - 1)/2>(\cos\theta)$, the function $\Psi_+(\cos\theta_i)$ for a given $\cos\theta$ bin i is no longer given by the number of events in the bin, but is instead the value of moment $<(3\cos^2\beta - 1)/2>(\cos\theta)$ in that bin for positive helicity. The data can thus be adjusted to a simple linear combination:

$$\Lambda(P_\tau, \cos\theta) = \frac{1 + P_\tau}{2} \Psi_+(\cos\theta) + \frac{1 - P_\tau}{2} \Psi_-(\cos\theta).\qquad (5.31)$$

To perform the fits, MINUIT [56] fitting routines have been used.

It is worthwhile stressing that the procedures described take into account

- the contribution of background coming from the other τ decay modes, and
- the effect of QED radiative corrections, since the KORALZ Monte Carlo has been used.

5.2.4 Results

A number of fits have been performed:

- a fit to the $(\cos\theta, \cos\beta)$ two-dimensional distribution,
- fits to each of the $dN/d\cos\theta$, $< (3\cos^2\beta - 1)/2 > (\cos\theta)$, $< \cos 2\gamma > (\cos\theta)$, $< \sin 2\gamma\, sign(s_1 - s_2) > (\cos\theta)$ and $< \cos\beta\, sign(s_1 - s_2) > (\cos\theta)$ distributions,
- a combined fit to these distributions, and
- a fit to the ξ distribution

The results are summarized in Table 5.4. The determination of P_τ through different variables

Fitted distribution	P_τ
$(\cos\theta, \cos\beta)$	-0.25 ± 0.16
$A = dN/d\cos\theta$	-0.23 ± 0.41
$B =< (3\cos^2\beta - 1)/2 > (\cos\theta)$	-0.22 ± 0.17
$C =< \cos 2\gamma > (\cos\theta)$	-0.32 ± 0.11
$D =< \sin 2\gamma\, sign(s_1 - s_2) > (\cos\theta)$	-0.05 ± 0.32
$E =< \cos\beta\, sign(s_1 - s_2) > (\cos\theta)$	-0.08 ± 0.34
$A + B + C + D + E$	-0.265 ± 0.085
ξ	-0.315 ± 0.087

Table 5.4: *Results of the fit to P_τ for different distributions.*

allows useful crosschecks of the fitting procedure and provides confidence in the goodness of the final result. In fact, systematic biases in a particular variable would produce a very different determination of P_τ compared with the other variables, and thus can be spotted easily. A few points should be stressed:

- the various fits to P_τ in Table 5.4 are in good agreement with each other. The χ^2 per degrees of freedom for the fits ranges between 0.5 and 1.4, which indicates a good quality of the fits,
- the use of all the decay variables (through the combined moments fit or the fit to ξ) improves the error on P_τ with respect to the usual $(\cos\theta, \cos\beta)$ distribution, and

- the quoted errors, determined by the fit, include not only the statistical errors from the number of data events, but also include a contribution from the uncertainty of $\Psi_\pm$ due to the limited Monte Carlo statistics. This contribution will be quantified in Section 5.3.

The best P_τ determination is obtained using the combined fit of the moments or the ξ variable. Both the fitted value and its error are close using both methods, as can be seen in Table 5.4. The value obtained from the combined fit is taken as the final result of this analysis. The reason is that moments are less sensitive to acceptance and background effects than is ξ, and therefore the associated systematic error is smaller.

The Monte Carlo expectations corresponding to the fitted value of P_τ (combined moments fit) are superimposed on the data distributions in Figs. 5.16-5.18.

5.3   Systematic uncertainties

In this Section, the systematic uncertainties in the P_τ measurement are discussed. The contribution due to possible experimental biases is determined. A specific study is performed to assign a systematic uncertainty for dependence of the P_τ measurement with the improved sensitivity method on the theoretical model used for the hadronic current.

5.3.1   Experimental systematic error

• Selection and backgrounds
Possible biases in the P_τ measurement due to the $\tau \to a_1\nu$ event selection have been checked. The procedure is analogous to the one used for the branching ratio measurement (*cf.* Section 3.6), where the systematic error was estimated by varying the selection cuts. For each variation of the cuts, the $\Psi_\pm$ functions are recalculated, and the fit to P_τ is performed again. The observed shift with respect to the value obtained for the nominal cuts is taken as an estimate of the systematic uncertainty: $\Delta P_\tau = \pm 0.03$. In the $\tau \to a_1\nu$ selection, a new cut is imposed, namely that on the invariant mass of the unlike-sign pion combination. The allowed range for the $\pi^+\pi^-$ invariant mass has been moved by 0.04 GeV, which is consistent with the resolution in the mass, and $\Delta P_\tau = \pm 0.02$ is obtained.

Notice that the procedure of varying the cuts affects both the acceptance and the background contribution. To study possible biases due to the background, it has been scaled by 30% (assumed to be the maximum possible deviation from the Monte Carlo estimate), and the effect on P_τ ($\Delta P_\tau = \pm 0.01$) is taken as an estimate of the possible bias.

• Acceptances
Another bias could come from an incorrect description of the acceptances. Notice that an overall scale factor would not affect the final result. Since the moment dependence on $\cos\theta$ is used to determine P_τ, a variation of the $\cos\theta$ acceptance has been considered as a possible

Figure 5.16: *a) the data distribution $dN/d\cos\theta$ (dots) together with the Monte Carlo expectation corresponding to the fitted value of P_τ (solid line), b) the equivalent distributions for $< (3\cos^2\beta - 1)/2 > (\cos\theta)$.*

Figure 5.17: *a) the data distribution $< \cos 2\gamma > (\cos\theta)$ (dots) together with the Monte Carlo expectation corresponding to the fitted value of P_τ (solid line), b) the equivalent distributions for $< \sin 2\gamma sign(s_1 - s_2) > (\cos\theta)$.*
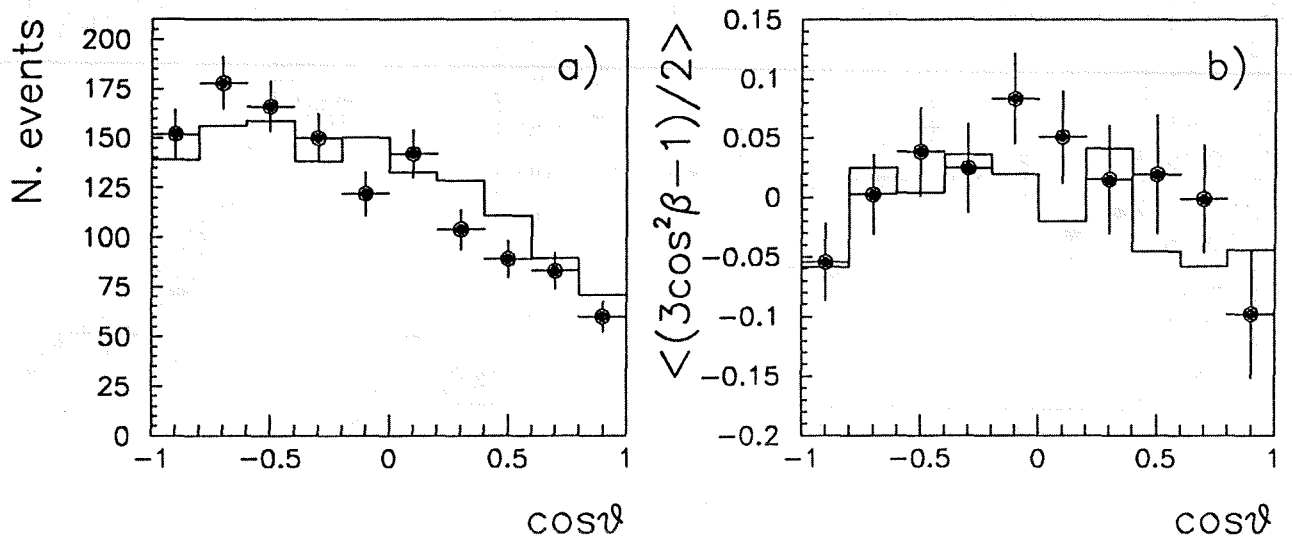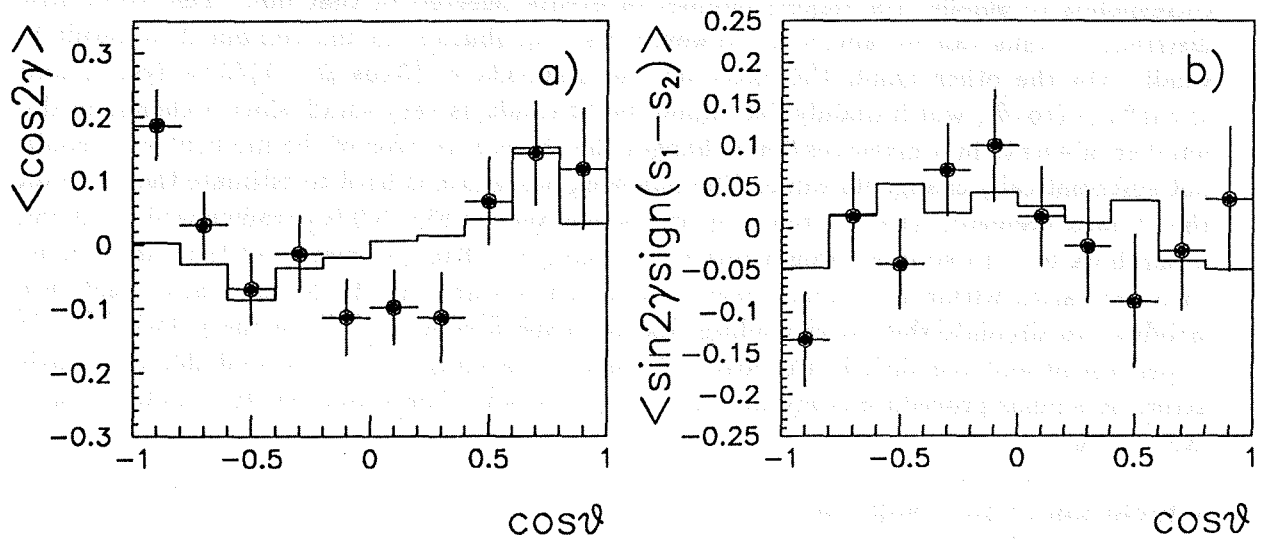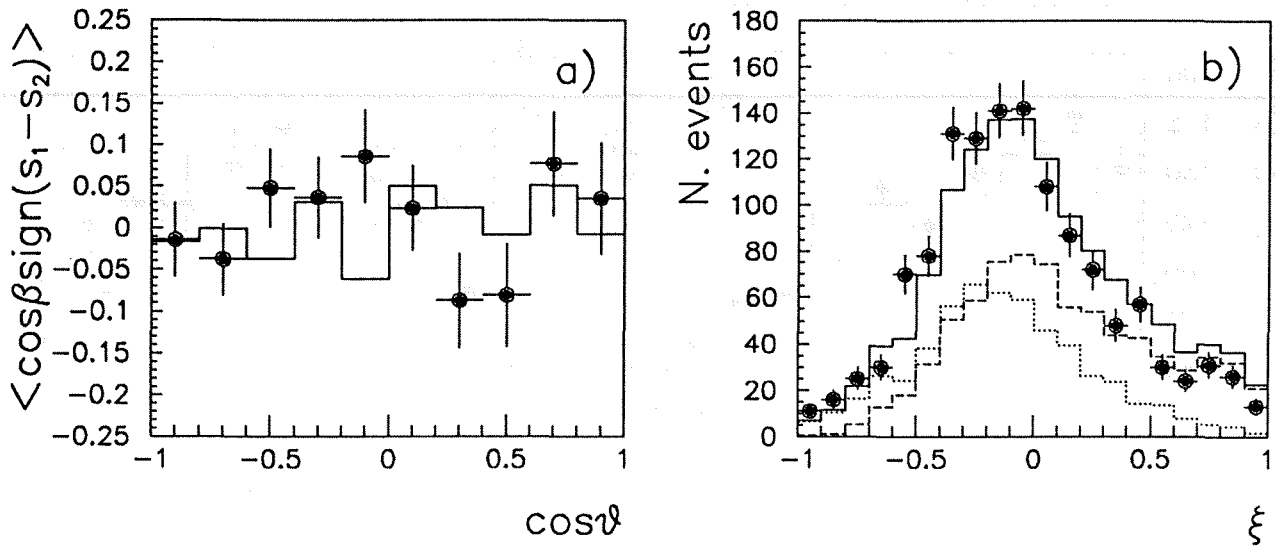
Figure 5.18: *a) the data distribution $< \cos\beta sign(s_1 - s_2) > (\cos\theta)$ (dots) together with the Monte Carlo expectation corresponding to the fitted value of P_τ (solid line) b) the ξ data distribution superimposed on the Monte Carlo expectation corresponding to the fitted value of P_τ. The separate contributions from $P_\tau = -1$ (dashed line) and $+1$ (dotted line) are shown.*

source of systematic error. Notice that a smaller (or larger) acceptance in a given $\cos\theta$ bin corresponds to smaller (or larger) number of events selected in that bin. The $dN/d\cos\theta$ distribution thus can be affected. However, its contribution to the combined fit result is small. On the other hand, the effect on the moments $< (3\cos^2\beta - 1)/2 > (\cos\theta)$ and $< \cos2\gamma > (\cos\theta)$, which mainly determine the fit result, is very small, since a change in the number of events in a given $\cos\theta$ bin changes the statistical error of the moment but should not systematically change its value. The following procedure is used to estimate the effect on the P_τ measurement. The Monte Carlo $\cos\theta$ acceptance of Fig. 5.9 is parametrized by fitting a parabola to it (a simple straight line is not enough). The parameters of the parabolic fit then are varied within a standard deviation of their errors, and the Monte Carlo events are weighted to simulate the corresponding change in the acceptance. Then the polarization fit is performed and the shift in the fitted P_τ value is taken as an estimate of the systematic error. A similar procedure is applied to $\cos\beta$ and $\cos\gamma$. The estimated systematic error is $\Delta P_\tau = \pm 0.01$.

• Inclusion of the 1992 data

Several checks have been performed on the sample of data collected in 1992 which are used for the P_τ measurement. The performances of the detectors used for the selection (microvertex, tracking detectors, electromagnetic calorimeter) have been studied. All the distributions for the microvertex detector (number of VD hits associated to isolated tracks, number of tracks with associated VD hits in the three prong hemisphere, etc.) are in good agreement with the distributions of 1991, and an independent preliminary analysis of the τ lifetime [57] also shows that the behaviour of the VD is of the same quality of the 1991 run. As far as the HPC is
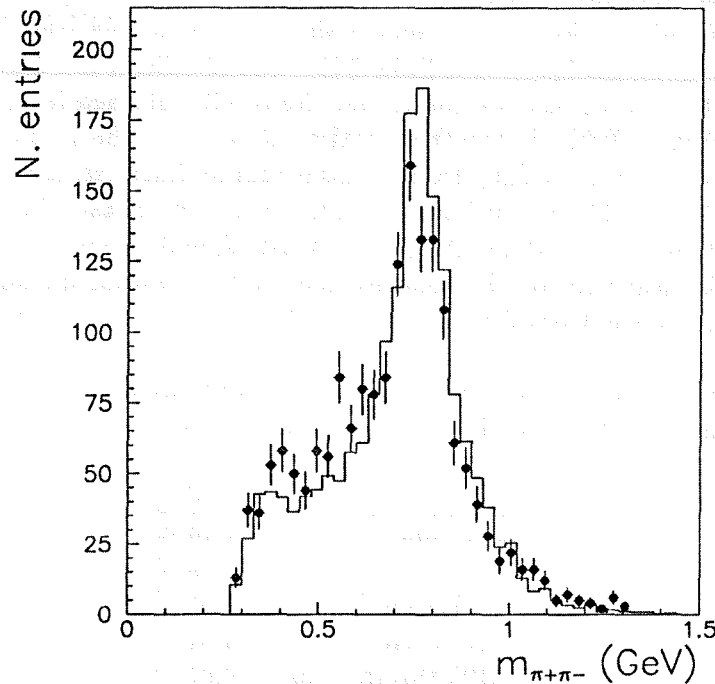
Figure 5.19: *The invariant mass $m_{\pi^+\pi^-}$ (two entries per event) for the unlike-sign combination for the 1992 data (dots). The solid line is the Monte Carlo expectation.*

concerned, the only difference with respect to the 1991 performances is in the energy threshold. In 1991, the electromagnetic calorimeter showed a minimum energy threshold in a layer of $\simeq$ 30 MeV (see the detailed discussion in Section 3.6.1). In 1992, the high voltages of the proportional chambers have been slightly increased, which corresponds to a lower threshold at $\simeq$ 20 MeV. To study the effect on P_τ, the new threshold has been put into the Monte Carlo and the polarization analysis was performed again. The observed shift is taken as an estimate of the systematic error, giving $\Delta P_\tau = \pm 0.01$. As far as the tracking detectors are concerned, the only possible bias can come from the momentum resolution in the 1992 data. To illustrate the problem, the invariant mass of the unlike-sign pion combination is shown in Fig. 5.19. A slightly worse resolution is seen when compared with the 1991 performance shown in Fig. 5.8. The reason is that the final alignment of the tracking detectors for the 1992 data used for this analysis was not yet available. The momentum resolution for 45 GeV muons in 1991 was $dp/p = 3.5\%$, to be compared with 6% for this set of 1992 data. To estimate the possible effect on P_τ, the momentum resolution in the Monte Carlo has been accordingly smeared and the corresponding shift in P_τ is taken as an estimate of the systematic error ($\Delta P_\tau = \pm 0.03$).

• **Monte Carlo statistics**
To estimate the error due to the limited Monte Carlo statistics, the following procedure has been used. The Monte Carlo moments used in Section 5.2.4 to fit the data also have been fit to high statistics $\Psi_\pm$ distributions generated by KORALZ. Notice that in this case detector effects are not included in the $\Psi_\pm$. However, it was shown in Section 5.2.2 that the moment distributions calculated from reconstructed variables reproduce well the original generated

distributions. The only exception is the $dN/d\cos\theta$ distribution, which in any case contributes marginally to the total sensitivity, and thus has been removed from the fit. The fitted value of this Monte Carlo polarization is consistent with the original polarization in the generation, and its error for the combined moments fit is $\Delta P_\tau = 0.050$. Then, the data have been fit with this same high statistics, $\Psi_\pm$ distributions, and the result obtained is $P_\tau = -0.234 \pm 0.073$. This uncertainty $\Delta P_\tau = 0.073$ is the true statistical error on the measurement of P_τ since it is not subject to any uncertainty from limited Monte Carlo statistics. Notice that the quadrature of 0.073 and 0.050 is consistent with the 0.085 uncertainty in Table 5.4. The error $\Delta P_\tau = 0.050$ is attributed to the Monte Carlo statistics, and assigned as a systematic error. Thus, the true statistical error on the measurement of P_τ is obtained from the subtraction in quadrature of $\Delta P_\tau = 0.050$ from $\Delta P_\tau = 0.085$.

All the uncertainties discussed in this Section are summarized in Table 5.5. The largest contribution comes from the limited Monte Carlo statistics.

Source	ΔP_τ
Selection	0.03
m_ρ cut	0.02
Background	0.01
Acceptance	0.01
HPC thresh. 1992	0.01
$\Delta p/p$ 1992	0.03
MC statistics	0.05
Data statistics	0.07
Total	0.099

Table 5.5: *Summary of experimental errors in the P_τ measurement.*

5.3.2   Systematic error from the model dependence

The use of all the decay variables has improved significantly the sensitivity to P_τ. The method shown here, either through the combined fit of the moments or of the ξ variable, relates the various components of the hadronic current. Thus, particular care should be taken in understanding possible biases in the measurement coming from the model dependance of the hadronic form factors W_X. An important difference exists between the moments method and the ξ variable method. To calculate the ξ variable for a given event, an explicit model for W_X must be chosen (*cf.* Section 5.1.3). Thus, the ξ histogram depends on the particular model used for the calculation of ξ. The moments, instead, are calculated only from the decay variables and no assumption on a specific model is needed to produce the corresponding histograms. It is only when the moments are fitted that a particular model must be chosen.

The results quoted in Section 5.2.4 have been obtained assuming the Kühn and Santamaria [43] model for the calculation and fitting of the ξ distribution and for the fit of the moments. In the following, the model dependence for both ξ and the moments is analyzed, since the systematic effects in the two methods are different, and this allows useful crosschecks. Fits

with various assumptions will be performed and compared to the results obtained with the Kühn and Santamaria model, which will be referred as the standard fit. For each assumption, either on the a_1 parameters or on the model for the hadronic current, a large sample of $\tau \to a_1 \nu$ events ($\simeq 100000$) has been generated with KORALZ, without detector simulation.

• **Variation of the a_1 parameters**

The mass and width of the a_1 are not very well determined and depend on the specific model used to fit the 3π invariant mass distribution (see discussion in Section 4.3.4). Also, it has been shown in Section 4.6 that the three pion Q^2 distribution and the total rate can significantly change depending on m_{a_1} and Γ_{a_1}. As far as P_τ is concerned, no effect is expected in the case of the ξ variable. In fact, ξ can be written:

$$\xi = \frac{\sum_X g_X W_X}{\sum_X f_X W_X} \qquad X = A, C, D, E. \tag{5.32}$$

The a_1 Breit-Wigner factor is the same for all W_X and can be factorized both in the numerator and denominator of (5.32), and thus it cancels. The correctness of this argument has been checked producing ξ distributions for different values of m_{a_1} and Γ_{a_1} as input to the KORALZ Monte Carlo, and no difference has been found.

On the other hand, the moments could be affected, since they are proportional to W_X (*cf.* expressions (5.13)-(5.17)) and thus to the a_1 Breit-Wigner. Moment distributions obtained changing m_{a_1} and Γ_{a_1} by ± 0.05 GeV have been produced to estimate the effect. In order to give a quantitative estimate of the possible bias, a combined fit of the moments obtained for each m_{a_1} and Γ_{a_1} variation is performed, using as $\Psi_\pm$ the distributions corresponding to the standard fit. The maximum shift observed with respect to the standard fit result is $\Delta P_\tau = 0.01$.

• **Different theoretical models**

In the standard fit the Kühn and Santamaria model is used. In Section 4.3, the model of Isgur, Morningstar and Reader [44] and the model of Feindt [45] have also been discussed. These models are based on different theoretical assumptions: chiral dynamics (Kühn and Santamaria), flux-tube-breaking model (Isgur et al.) and angular momentum eigenstate amplitudes (Feindt). Their predictions of the hadronic form factors have been compared in Section 4.6. It is important to understand if the differences between the model predictions affect the P_τ measurement significantly. The following procedure has been used. The models of Isgur et al. and Feindt have been substituted into the KORALZ Monte Carlo program for the Kühn and Santamaria model. The distributions used to determine P_τ (moments and ξ) can then be produced using the same software chain. Notice that ξ is calculated using always the Kühn and Santamaria model. In order to give a quantitative estimate of the possible bias, fits of the distributions (moments and ξ) obtained from the Isgur et al. and Feindt models are performed, using as $\Psi_\pm$ the distributions corresponding to the standard fit (Kühn and Santamaria). The maximum observed shift with respect to the standard fit result is $\Delta P_\tau = 0.01$. The dependence of P_τ on m_{a_1} and Γ_{a_1} has also been investigated for the predictions of the Isgur et al. and Feindt models, following the procedure previously described. Similar results have been obtained.

• **Effect of a scalar contribution**

In the Kühn and Santamaria model the effect of a possible scalar contribution (π') is not

considered ($W_{SA} = W_{SB} = W_{SC} = W_{SD} = W_{SE} = 0$). In case such a contribution exists, one can ask what is the effect of neglecting it in the P_τ measurement. It is clear that the combined fit of the moments will be only marginally affected by the presence of such contribution, since the only moment which should be modified is $dN/d\cos\theta$ (*cf.* expression (4.83)), which is not very sensitive to P_τ. The ξ variable is modified by the presence of a scalar part in the sense that terms $g_X W_X(f_X W_X)$ $X = W_{SA}$,.. should be added in the numerator (denominator) of expression (5.32). Notice that the Isgur et al. model contains a scalar contribution, and thus this effect already is contained in the comparisons between the models previously performed. As a further check, the Kühn and Mirkes parametrization for the π' (see expression (4.92)) has been introduced into KORALZ and the procedure described before has been applied. The observed variation is again negligible.

• Conclusions

The various checks which have been performed in this Section allow an estimate of the theoretical systematic error of the P_τ measurement performed with the new method with increased sensitivity. The conclusion is that such an error is small and negligible compared to the present statistical error of the measurement and to the present estimate of the experimental error. A conservative estimate of the theoretical systematic error is given by the combination in quadrature of the maximum shifts (0.01) from the variation of the a_1 parameters and the comparison of the different models: $\Delta P_{\tau theor.} = 0.015 \pm 0.011$. The error on this estimate comes from the Monte Carlo statistics used for the various fits performed in this Section.

5.4   Final results

The measured value of the τ polarization through the analysis of the $\tau \to 3\pi\nu_\tau$ decay mode described in this chapter is:

$$P_\tau = -0.265 \pm 0.070_{stat.} \pm 0.070_{exp.} \pm 0.015_{theor.}, \tag{5.33}$$

where $\Delta P_{\tau stat.}$ is the statistical error of the measurement, $\Delta P_{\tau exp.}$ is the error attributed to experimental biases which also includes the Monte Carlo statistics, and $\Delta P_{\tau theor.}$ is the uncertainty assigned to the measurement because of its theoretical model dependence. The experimental error is dominated by the limited Monte Carlo statistics ($\Delta P_\tau = 0.050$).

The result differs from zero by almost three standard deviations, and is in good agreement with the present average of P_τ obtained combining the results of all the LEP experiments ($P_\tau = -0.138 \pm 0.018$ [58]).

Using the formulas introduced in Section 1.2, this P_τ value can be used to obtain:

$$\frac{g_{V_\tau}(m_Z^2)}{g_{A_\tau}(m_Z^2)} = 0.134 \pm 0.053 \tag{5.34}$$

$$\sin^2\theta_W(m_Z^2) = 0.217 \pm 0.012. \tag{5.35}$$

The measurement is still dominated by the statistical uncertainty. However, the improvements obtained with the analysis presented in this chapter should be remarked:

- a new method to measure P_τ using the $\tau \rightarrow 3\pi\nu_\tau$ decay mode has been studied. Its sensitivity is better by a factor $\simeq 2$ relative to the standard two-dimensional $(\cos\theta, \cos\beta)$ method.

- the experimental systematic uncertainty is not presently limiting the measurement and is expected to improve with more data and higher Monte Carlo statistics, and

- the systematic error arising from the theoretical model dependence of the P_τ determination has been estimated and found to be negligible.

One can thus foresee that with high statistics the P_τ determination through the $\tau \rightarrow 3\pi\nu_\tau$ decay mode will be competitive with the other hadronic decay modes $(\tau \rightarrow \pi\nu, \tau \rightarrow \rho\nu)$ and better than the leptonic ones $(\tau \rightarrow e\nu\bar{\nu}, \tau \rightarrow \mu\nu\bar{\nu})$.

Conclusions

From a sample of $e^+e^- \rightarrow Z^0 \rightarrow \tau^+\tau^-$ events collected in the 1991 LEP run with the DELPHI detector, 1169 $\tau \rightarrow 3\pi n\gamma\nu_\tau$ $(n \geq 0)$ candidates have been selected. The branching ratio for this decay mode has been measured to be:

$$Br(\tau \rightarrow 3\pi n\gamma\nu_\tau) = (13.28 \pm 0.39_{stat} \pm 0.17_{syst}) \%$$

Once events with accompanying photons are rejected, 570 $\tau \rightarrow 3\pi\nu_\tau$ candidates are left. The corresponding branching ratio has been determined to be:

$$Br(\tau \rightarrow 3\pi\nu_\tau) = (8.35 \pm 0.35_{stat} \pm 0.24_{syst}) \%$$

The statistical error is dominant in both determinations. Notice that the decay mode $\tau \rightarrow K^*\nu_\tau \rightarrow K_S\pi\nu_\tau \rightarrow \pi\pi\pi\nu_\tau$ has been considered as a background in the analysis performed. The three charged particle decays with kaons $(\tau \rightarrow K\pi\pi\nu_\tau, \tau \rightarrow KK\pi\nu_\tau)$ have not been subtracted from the branching ratios quoted. These remarks are important since different experiments use different approaches in the treatment of these kaon decay modes, and the global effect can add up to $\simeq 1\%$ on the branching ratio results.

The τ polarization measurement has been performed using the sample of $\tau \rightarrow 3\pi\nu_\tau$ previously selected in addition to partial set of 1992 data. A new method has been devised to perform the P_τ measurement. The method exploits all the kinematical variables available in the $\tau \rightarrow 3\pi\nu_\tau$ decay. The relevant distributions sensitive to P_τ have been derived. An improvement in sensitivity by a factor $\simeq 2$ has been obtained, *i.e.* the statistical error on the P_τ determination with the new method is approximately half of that obtained with previous methods using the same statistics. The gain in sensitivity is obtained because all the hadronic form factors are used. However, theoretical models still must be explicitly assumed to describe the hadronic form factors. For this reason, a detailed study of the model dependence of the measurement has been performed. From a sample of 1328 $\tau \rightarrow 3\pi\nu_\tau$ candidates (1991 and part of 1992 data), the τ polarization is determined to be:

$$P_\tau = -0.265 \pm 0.070_{stat} \pm 0.070_{syst} \pm 0.015_{theor}$$

where the first error quoted is statistical and the second error is systematic. The third error quoted has been assigned to take into account the theoretical uncertainties from the model dependence of the hadronic form factors. This error has been found to be small, and therefore

the new method to measure P_τ with the $\tau \to 3\pi\nu_\tau$ decay will not be limited by theoretical uncertainties even in the case of very large statistics.

References

[1] J. H. Kühn, E. Mirkes, Phys. Lett. B286 (1992) 381

[2] Y. S. Tsai, Phys. Rev. D 4 (1971) 2821;
Erratum, Phys. Rev. D 13 (1976) 771

[3] B. C. Barish, R. Stroynowski, Phys. Rep. 157 (1988) 1;
M. Perl, to appear in Rep. Prog. Phys., SLAC-PUB-5614 (1991);
A. Pich, CERN-TH 6237/91 (1991)

[4] M. L. Perl et al., Phys. Rev. Lett. 35 (1975) 1489

[5] J. Z. Bai et al., Phys. Rev. Lett. 69 (1992) 3021

[6] Review of particle properties, Phys. Rev. D45 (1992)

[7] The world averages are quoted from K. G. Hayes note in Review of particle properties, Phys. Rev. D45 (1992), VI.19

[8] D. Decamp et al., ALEPH Collab., Zeit. Phys. C54 (1992) 211

[9] H. J. Behrend et al., CELLO Collab., Zeit. Phys. C46 (1990) 537

[10] H. Albrecht et al, ARGUS Collab., Zeit. Phys. C53 (1992) 367

[11] J. D. Bjorken, S. D. Drell, Relativistic Quantum Mechanics, (McGraw-Hill, New York, 1964)

[12] S. Jadach et al.,Z Physics at LEP, CERN 89-08 (1989), Vol. 1, p. 235, and references therein

[13] S.L. Glashow, Nucl. Phys. 22 (1967) 579;
S. Weinberg, Phys. Rev. Lett. 19 (1967) 1264;
S. Salam in Elementary Particle Theory, ed. N. Svartholm, (Almquist and Wiksells, Stockholm, 1968), p. 367

[14] J. E. Augustin, Proceedings of the LEP Summer Study, CERN 79-01 Vol. 2, pag. 499;
G. Goggi, Proceedings of the LEP Summer Study, CERN 79-01 Vol. 2, pag. 483

[15] J. H. Kühn, F. Wagner, Nucl. Phys. B236 (1984) 16

[16] K. Hagiwara, A. D. Martin, D. Zeppenfeld, Phys. Lett. B235 (1990) 198

[17] A. Rougé, Zeit. Phys. C48 (1990) 75

[18] LEP Design Report, CERN Report LEP/84-01 (1984)

[19] DELPHI Collab., Technical Proposal, DELPHI 83-66/1;
     DELPHI Collab., DELPHI Progress Report, DELPHI 84-60 (1984);
     P. Aarnio et al., DELPHI Collab., Nucl. Instr. and Meth. A303 (1990) 233

[20] M. Jonker et al., DELPHI 91-92 DAS 112 (1991);
     T. Adye et al., DELPHI 92-145 DAS 131 (1992);
     J. A. Valls et al., DELPHI 92-162 DAS 135 (1992)

[21] DELPHI Collab., DELSIM — DELPHI Event Generation and Detector Simulation, DEL-
     PHI 89-67 (1989)

[22] S. Jadach and Z. Was, Comp. Phys. Commun. 36 (1985) 191;
     S. Jadach, J. H. Kühn, Z. Was, Comp. Phys. Commun. 64 (1990) 275;
     S. Jadach, B. F. L. Ward, Z. Was, Comp. Phys. Commun. 66 (1991) 276

[23] DELPHI Collab., DELANA user guide DELPHI 89-44 (1989)

[24] DELPHI Collab., TANAGRA — Track Analysis and Graphics Package, DELPHI 87-95
     (1987)

[25] J.E. Campagne and R Zitoun, Zeit. Phys. C43 (1989) 469

[26] F.A. Berends, W. Hollik, and R. Kleiss, Nucl. Phys. B304 (1988) 712;
     M. Böhm, R. Kleiss and W. Hollik, Nucl. Phys. B304 (1988) 687

[27] J. Cuevas et al., Nucl. Inst. and Meth. A274 (1989) 459

[28] P. Astier, A. Letessier-Selvon, ODTIME package write up, DELPHI 91-106

[29] T. Sjöstrand Comp. Phys. Comm. 39 (1986) 347

[30] F.A. Berends, P.H. Daverveldt and R. Kleiss, Phys. Lett. B148 (1984) 489 and Comp.
     Phys. Comm. 40 (1986) 271

[31] F. Matorras, DELPHI 92-124 PHYS 225

[32] P. Billoir, CORPUS Package, DELPHI 91-67 PHYS 121, PROG 175

[33] K. G. Hayes, to appear in the proceedings of the 2nd Workshop on Tau lepton Physics,
     Columbus, Ohio, U.S.A., September 8-11, 1992

[34] C. Zeemach, Phys. Rev. B133 (1964) 1201

[35] D. A. Varshalovich, Quantum Theory of Angular Momentum,
     World Scientific, Singapore-New Jersey-Hong Kong (1989)

[36] For reviews, see:
     G. Barbiellini, C. Santoni, Riv. Nuovo Cimento 9(2) (1986) 1;
     E. D. Commins, P. H. Bucksbaum, Weak Interactions of Leptons and Quarks (Cambridge
     University Press, Cambridge, 1983)

[37] N. Cabibbo, Phys. Rev. Lett. 10 (1963) 531

[38] R. P. Feynman, M. Gell-Mann, Phys. Rev. 109 (1958) 193;
S. S. Gershtein, J. B. Zeldovich, Sov. Phys. Journ. Exp. Theor. Phys. 2 (1957) 576

[39] H. Albrecht et al., ARGUS Collab., DESY 92-082 (1992)

[40] M. Gell-Mann, M. Levy, 16 (1960) 705

[41] M. G. Bowler, Phys. Lett. B182 (1986) 400

[42] N. A. Törnqvist, Zeit. Phys. C43 (1987) 695

[43] J. H. Kühn, A. Santamaria, Zeit. Phys. C48 (1990) 445

[44] N. Isgur, C. Morningstar, C. Reader, Phys. Rev. D39 (1989) 1357

[45] M. Feindt, Zeit. Phys. C48 (1990) 681

[46] S. Coleman, J. Wess, B. Zumino, Phys. Rev. 177 (1969) 2239;
C. G. Callan, S. Coleman, J. Wess, B. Zumino, Phys. Rev. 177 (1969) 2247

[47] For an introduction see:
F. J. Yndurain, Quantum Chromodynamics: an introduction to the Theory of Quarks
and Gluons, (Springer, New York, 1983)

[48] S. Weinberg, Phys. Rev. Lett. 18 (1967) 188

[49] R. Fischer, J. Wess, F. Wagner, Zeit. Phys. C3 (1980) 313

[50] N. Isgur, J. Paton, Phys. Lett. 124B (1983) 247;
N. Isgur, J. Paton, Phys. Rev. D31 (1985) 2910

[51] For reviews of lattice gauge theories see, for example:
M. Bander, Phys. Rep. 75 (1981) 206;
J. Kogut, Rev. Mod. Phys. 55 (1983) 775

[52] R. Kokoski, N. Isgur, Phys. Rev. D35 (1987) 907

[53] H. Albrecht et al., ARGUS Collab., DESY 92-125 (1992)

[54] J. H. Kühn, E. Mirkes, TTP92-20 (1992), to appear in Zeit. Phys.

[55] A. Rougé, LPNHE preprint X-LPNHE 92/20 (1992)

[56] F. James, M. Roos, MINUIT Function Minimization and Error Analysis, Release 89.12j,
December 1989

[57] D. Reid, Private communication

[58] L. Rolandi, CERN-PPE/92-175 (1992)